IMPACTS OF LATERAL SPREADING AND UPSTREAM CONDITIONS ON BUOYANT RIVER PLUMES: MIXING, STRUCTURE AND PLUME DYNAMICS

Yeping Yuan

A dissertation submitted in partial fulfillment of
the requirements for the degree of

Doctor of Philosophy

University of Washington

2012

Committee:

Alexander R. Horner-Devine, Chair

Jim Thomson

Parker MacCready

Daniel MacDonald

Robert Hetland

Peter Rhines

Program Authorized to Offer Degree:
Department of Civil and Environmental Engineering

0

University of Washington

Abstract

IMPACTS OF LATERAL SPREADING AND UPSTREAM CONDITIONS ON BUOYANT RIVER PLUMES: MIXING, STRUCTURE AND PLUME DYNAMICS

Yeping Yuan

Chair of the Supervisory Committee:
Associate Professor Alexander R. Horner-Devine
Department of Civil and Environmental Engineering

This dissertation investigates the nature of physical processes associated with buoyant river plumes under the impacts of rotation, lateral spreading and upstream conditions. Two sets of laboratory experiments, one focused on the whole rotating buoyant plume, and the other zoomed into the near field plume, are studied.

When lighter fluid is released into denser water, buoyancy causes the lighter intruding flow to run on top of the ambient water. This baroclinic flow propagates both in the offshore direction due to strong momentum from the inflow source and laterally in the alongshore direction because of the horizontal pressure gradient. This energetic region is the so-called near-field region where the plume behaves like a buoyant jet and is characterized by high momentum and strong stratification. Under the influence of the Coriolis force, the density driven flow is then guided along the coast, forming an anti-cyclonic bulge (in northern hemisphere). In this large scale region, called far-field region, the flow is more geophysical and less energetic. The transition between the two regions is the mid-field region in which the fluid transfers from an energetic flow into a geophysical current.

The first laboratory experiment is designed to simulate the dynamics of two adjacent coastal river plumes in a rotating reference frame. The plumes are generated on a rotating table using two identical fresh water inlets, with blue and red dye indicating upstream and downstream river flows, respectively. We successfully calculate the depth field for the combined two-plume system and differentiate between the two plumes using a two-dimensional calibration map. With the upstream coastal current acting as the ambient condition, the downstream plume bulge does not reach a steady condition. The downstream bulge is pulled into the upstream bulge, forming a larger re-circulating bulge which then becomes unstable. The coastal current transport can be calculated by assuming a geostrophic cross-balance balance with an empirical coefficient $\alpha = 0.6$.

The impact of lateral spreading on mixing was investigated for laboratory scale non-rotating stratified-shear plumes. The experiment is begun with the release of a vertical wall of freshwater and the simultaneous activation of a pump which supplies freshwater to the filling basin. Velocity and density fields are obtained using the combined particle image velocimetry (PIV) and planar laser induced fluorescence (PLIF) method, while the lateral spreading rate is determined using the optical thickness method (OTM). The vertical mixing is parameterized by the turbulent buoyancy flux, which is calculated using a control volume approach. Both the lateral spreading rate and mixing are related to inflow Fr, where the lateral spreading rate decreases with Fr_i while mixing increases with Fr_i. By comparing the mixing in the laterally confined and unconfined cases, we observe that although the lateral spreading significantly modifies the plume vertical structure, it does not change the local turbulent buoyancy flux. On the other hand, the lateral spreading increases the horizontal area

over which mixing occurs and as a result it increases the net dilution of river water at a fixed distance from the river mouth.

Unlike the local mixing process, we observe that the plume structure is significantly different in the laterally confined and unconfined plumes. We hypothesize that the laterally spreading river plume might be a source of non-linear internal solitary waves with trapped cores. Such waves are commonly observed in fjords, straits and coastal ocean, where a strong shear-stratified flow meets dramatical topography changes. A series of small scale Kelvin-Helmholtz instability billows are generated along the edge of the large-scale waves, propagating downstream and finally breaking at the wave trough. This phenomenon highly increases the mixing and entrainment at the edge and trailing edges of the wave while it inhibits the mixing at the frontal side of the wave.

In addition, our laboratory methods make a significant contribution to the field of experimental fluid mechanics. This work represents a novel method to extend classical optical thickness measurement to a two-dimensional calibration map using two colors for calculating two interacting plumes depth fields.

TABLE OF CONTENTS

LIST OF FIGURES

LIST OF TABLES

ACKNOWLEDGMENTS

I owe my deepest gratitude to my advisor, Alexander R. Horner-Devine. He has made available his support in all the possible ways. The graduate study could have been much harder without the numerous advices and discussion from him in these years. In addition, he spared no effect to help me in building my self-confidence and share the wisdom and enthusiasm that I can benefit for the rest of my life. I would also like thank my Ph.D. committee members, Jim Thomson, Parker MacCready, Daniel MacDonald, Robert Hetland and Peter Rhines, for their timely advice and input to my research work.

In addition, I owe thanks to all the people in EFM group who over the past five years have shared their experience, knowledge and friendship with me, especially every Monday morning coffee and Thursday meeting/BBQ. The EFM group was a fantastic place to work. Many thanks to Maggie Averner, Abbas Hooshmand, J.Paul Rinehimer, Chris Bassett, Maggie McKeon, Dan Nowacki, Michael Schwendeman, Roxanne Carini, Emily Spahn, Stefan Talke, Adam Price, Greg Curtiss, Bertand Dano. I have to thank the APL air-sea interaction & remote-sensing group: Andy Jessup, Chris Chickadel, Dan Clark, Alex De Klerk, for all the technical support and helpful discussion on my laboratory experiments.

I would like to thank three PIs in the MeRMADE project team, for making this great collaborate project happens. I am especially grateful to my close friend from this project: Kelly Cole and Georgia Kakoulaki. I would also like to thank other people in MeRMADE, Jianfeng Wang, Fei Chen, Zhaoru Zhang, Joshua Carlson for

all the discussion and meetings either from ooVoo or in person.

Laboratory experiments would not have been possible without the help from CEE department and UW-GFD lab. Jack Herndon and Yiming Liu supported me in the laboratory work. Eric Lindahl and Bob Koon provided a tremendous amount of assistance in building the plume basin. And all the undergraduate students helped me in the experiments and made valuable contribution to this work: Anthony Poggioli, Amanda Gehman, Stephany Wei, Melessa Nagamine, Shaun Bevan, Alejandro Salvado, and Kris Skotheim. I would also thank to the TransNow group for providing TCC room for every committee meetings I have during my Ph.D. study.

During my studies I was supported by the National Science Foundation (OCE-0850847) and the Endowed Presidential Fellowship, for which I am very thankful.

Beyond work and science I am so thankful to my dear parents, for their endless love and support. They are the ones who deserve all the honors I received from this degree. In the mean time, I would like to thank all my colleagues and friends in Seattle, who have made my life in United States the most joyful and memorable experience so far.

DEDICATION

to my dear parents, Bai Yuan and Xiaoling Zhang

Chapter 1

INTRODUCTION

Rivers play a critical role in the exchange of materials between the land and the ocean. River inflows provide highly concentrated river-borne materials to the ocean, which create regions of high biological productivity and diverse habitats along the coast. There are two possible ways that rivers can contribute to the nutrient concentration in the ocean. For high nitrate rivers, like the Mississippi river, the river plume can be a conduit that transport land-driven nutrients from watersheds to the ocean. Alternately, the rivers can entrain coastal upwelling-derived nutrients into the euphotic layer and distribute them into the plume (Hickey and Banas, 2008). Therefore in estuaries and coastal regions, river plume dynamics and plume interactions with ambient ocean water are important in understanding the transport of organisms and particles, and the dispersion of nutrients. Nearly one-half of all oceanic carbon burial occurs in large river deltas (Hedges and Keil, 1995). The goal of this dissertation is to investigate the impacts of two important features on two different regions of the river plume system: the ambient along-shore current on the mid-field plume and the lateral spreading on the near-field plume. With these investigations this work will provide further development in understanding plume dynamics and the fundamental physical processes that influence coastal ecosystems.

1.1 General buoyant plume dynamics

A simple conceptual model for an idealized river plume can be described in terms of four water masses (Figure 1.1): source water, the tidal plume, the re-circulating plume and the far-field plume (Horner-Devine et al., 2009). The second region is often referred to as the near-field plume (Figure 1.1 a yellow box), the region where the buoyant plume is highly energetic due to inflow momentum. This region is of particular interest, because up to half of the mixing and entrainment occurs in this region, even though it only covers a small region of the total plume area (Hetland, 2005). The energy of the plume in the near-field region increases the shear at the base of the plume, entraining low-momentum, high-density ambient water into the buoyant plume. Entrainment continuously increases the buoyant plume volume and at the same time causes it to decelerate, leading the plume return to subcritical conditions and transition into the mid-field (re-circulating) region. Ideally, the mid-field plume is defined as a re-circulating bulge near the river mouth caused by the earth's rotation, as shown in Figure 1.1 a (blue box). However, analysis of the mid-field plume is difficult because its position and characteristics are highly sensitive to wind, coastal current, and ambient water properties. The evolution of the geostrophic far-field plume is dominated by earth's rotation, wind, and background flow, and the flow is primarily along-shore (Figure 1.1 a green box).

This simple model provides an idealized understanding of buoyant plumes; however, the real world is much more complex and unpredictable. It is difficult to produce an accurate picture of large-scale river plumes from field studies due to large spatial scales, short time scales and the confounding influence of other natural phenomena. In addition, unpredicted wind (Hickey et al., 1998), different ambient coastal currents (Fong and Geyer, 2002), and complex bathymetry (Thomas and Linden, 1998;

Signell and Geyer, 1991) all have strong influences on the fate of the plume water. Although the plume could reach steady-state between tides, the change in the inflow flowrate causes the plume becomes unsteady and the dynamics hard to predict. In this case, laboratory simulations can isolate one or two parameters at a time to study the idealized plume dynamics and the impacts of each parameter on the plume.

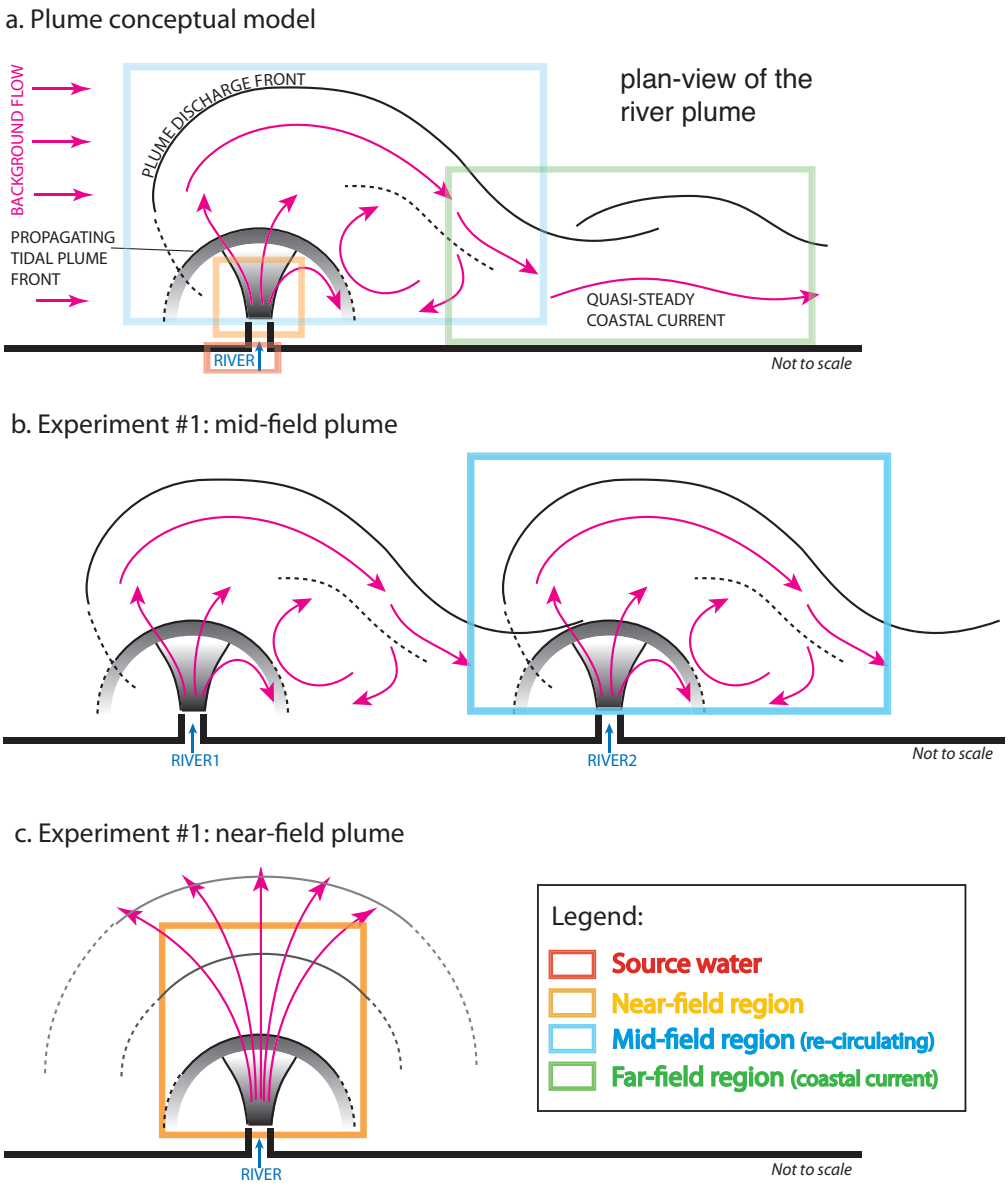

Figure 1.1: a) Conceptual model of an idealized river plume, showing four regions: source water (red), near-field region (yellow), mid-field region (blue) and far-field region (green). b) Schematics of the first rotating experiment described in §2, blue box (mid-field region) shows the region of the interest. c) Schematics of the second non-rotating experiment, yellow box (near-field region) shows the region of the interest. Legends are shown in the black box in (c). The figure was modified from the figure 1 in MeRMADE2 project proposal by D. G. MacDonald, R. D. Hetland and A. R. Horner-Devine.

1.2 Near-field plume

Once the plume leaves the source channel or river mouth, the dynamics of the plume are controlled by the strong offshore momentum source. During this process outflowing buoyant river water propagates along the ocean surface and expands laterally due to the horizontal baroclinic pressure gradient. At the river mouth the freshwater is initially channelized in the estuary and subsequently begins to spread once it reaches the coastal ocean. During this transition to the unconfined state it undergoes vertical and lateral adjustments and the spreading rate is set dynamically based in part on the initial momentum and the density of the buoyant layer. Luketina and Imberger (1987) presented field observations of a tidally pulsed buoyant plume and found an overturning roller at the plume front. Surface water behind the front overtook the roller and formed an energetic mixing area following the front, consistent with the previous laboratory work from Britter and Simpson (1978). Other field observations (Wright and Coleman, 1971; Hetland and MacDonald, 2008) suggest that the lateral spreading of buoyant plumes should behave like a lateral lock-exchange flow, where the spreading rate is proportional to the local internal gravity wave speed, c: $DW/Dt = 2c$, where W is the plume width. Since the streamwise propagation speed of the buoyant layer well behind the front is initially set by the outflow momentum, this implies that the lateral spreading depends on the inflow Froude number $Fr_i = U_0/\sqrt{g_0' H_0}$, where U_0, g_0' and H_0 are inflow velocity, reduced gravity and water depth, respectively. Hetland and MacDonald (2008) and Chen et al. (2009) both suggested that lateral spreading might be significantly affected by the mixing in the near-field region and that the spreading rate is complex.

1.3 Mid-field and far-field plume

As a result of the mixing and spreading processes in the near-field region, the plume loses its initial momentum and forms a re-circulating bulge with a length scale on the order of the Rossby deformation scale ($L_R = \frac{\sqrt{gD}}{f_0}$, where D is the total water depth and f_0 is the Coriolis parameter). Coriolis effects cause the plume to form a two-part structure, with an anticyclonic bulge at the river mouth and a coastal current propagating downstream (in the Kelvin wave sense, i.e., to the right in the northern hemisphere). This bulge circulation has been observed at the mouths of the Columbia River (Horner-Devine et al., 2009) and the Hudson River (Chant et al., 2008). Nof and Pichevin (2001) suggested that the Coriolis force associated with offshore bulge growth balances the alongshore current momentum flux. In the absence of such bulge growth, the alongshore momentum cannot be balanced. A number of previous studies confirm the existence of an unsteady bulge using numerical models (Fong and Geyer, 2002) and lab experiments (Avicola and Huq, 2002; Horner-Devine et al., 2006). In the presence of a uniform alongshore ambient current, the river plume can evolve to a steady-state in which the source freshwater is carried entirely in the coastal current and bulge growth ceases (Fong and Geyer, 2002).

1.4 Structure of this dissertation

The goal of this dissertation is to investigate the impacts of two important features of the mid-field and near-field plume - ambient along-shore current and lateral spreading - on river plumes. With these investigations this work will further develop our understanding of plume dynamics and the fundamental physical processes that influence coastal ecosystems. The key issues to be addressed can be summarized by the following set of questions:

- How does background alongshore current affect the transition in the mid-field plume? Will the bulge re-circulation become stable with the background alongshore current (Figure 1.1 b)?

- How does lateral spreading affect mixing and entrainment in the near-field plume (Figure 1.1 c)?

- Does lateral spreading modify the hydraulics of two-way exchange flow in an energetic river plume system (Figure 1.1 c)?

In this dissertation, there are three major scientific chapters, all focusing on the laboratory simulation of river plumes. Chapter 2 of this dissertation investigates the response of an idealized mid-field plume to a specific background current: an identical river plume upstream. Chapters 3 and 4 examine lateral spreading processes and the effect of lateral spreading on the near-field river plume. In Chapter 3, estimates of lateral spreading rate are derived from the time-averaged horizontal freshwater thickness. The bulk parameters used to describe the mixing and entrainment processes are calculated from time-averaged vertical density and velocity profiles. The relationship between vertical mixing and lateral spreading is then investigated from the available data. In Chapter 4, the impacts of lateral spreading on the plume structure are studied using two-way exchange flow hydraulics. Finally, a summary of and conclusions from the entire work are presented in Chapter 5.

Chapter 2

TWO INTERACTING BUOYANT PLUMES [1]

We describe a technique for measuring the layer thickness of two interacting buoyant rotating gravity currents. The technique can be used generally to differentiate between water masses in experiments with multiple sources, and is used here to simulate the dynamics of two adjacent coastal river plumes. The plumes are generated using two identical fresh water inlets, with blue and red dye indicating upstream and downstream river flows, repectively. Two parameters, normalized intensity and color ratio, are measured with a 3-CCD color video camera and used to develop a two-dimensional (intensity-color ratio) calibration map for layer thickness. The calibration is used successfully to determine the depth field for the combined two-plume system and to differentiate between the two plumes. This technique is applied to compute the volumetric growth of a large eddy near the freshwater source and the transport rate of buoyant fluid away from the source in the coastal current. The validation tests show good agreement between the calculated plume volume and the input fresh water volume.

[1]This chapter duplicates a paper of the title as 'A two-color optical method for determining layer thickness in two interacting buoyant plumes' by Yuan, Y, M. E. Averner and A. R. Horner-Devine which appeared in Experiments in Fluids, May 2011, 50(5), 1235-1245, doi:10.1007/s00348-010-0969-y. All text and figures are identical with the exception of the relabeling of figures, and equation number.

2.1 Introduction

When buoyant fluid is released near a vertical wall in a rotating system, Coriolis forces guide the density-driven flow along the wall (Griffiths and Hopfinger, 1983). If the buoyant fluid is introduced with initial velocity normal to the wall, it forms a two-part structure, with an anticyclonic bulge at the river mouth and a coastal current propagating downstream (in the Kelvin wave sense, i.e., to the right in the northern hemisphere). This bulge circulation has been observed at the mouths of the Columbia River (Horner-Devine et al., 2009) and the Hudson River (Chant et al., 2008). Nof and Pichevin (2001) suggested that the Coriolis force associated with offshore bulge growth balances the alongshore current momentum flux. In the absence of such bulge growth, the alongshore momentum cannot be balanced. A number of previous studies confirm the existence of an unsteady bulge using numerical models (e.g. Fong and Geyer, 2002) and lab experiments (e.g. Avicola and Huq, 2002; Horner-Devine et al., 2006). In the presence of an alongshore ambient current, the river plume can evolve to steady-state in which the source freshwater is carried entirely in the coastal current and the bulge growth ceases (Fong and Geyer, 2002). In the two-river system, the coastal current from the upstream river act as the non-uniform ambient current to the downstream plume, with a high velocity inshore and almost zero velocity offshore. The primary motivation for experiments described here is to test whether the downstream river bulge remains steady with extra alongshore momentum from the upstream plume.

Many advanced techniques have been applied to measure velocity and/or concentration fields in river plumes. One recent method combines particle image velocimetry (PIV) and planar laser induced fluorescence (PLIF) to measure two-dimensional velocity and concentration fields simultaneously (e.g. Cowen et al., 2001; Horner-Devine, 2006). However, neither PIV nor PLIF is ideally suited for measuring the bulge

growth rate since they only resolve a single plane for the plume instead of the entire plume volume. The scanning LIF method provides both time-dependent and space-dependent concentration fields of the buoyant plume (Tian and Roberts, 2003). This three-dimensional concentration field could be used to measure the bulge volume grow rate, but introduces significant experimental complexity.

Optical thickness measurements can be used to determine plume volume, and thus, the bulge growth rate, from a measured depth field with a relatively simple experimental set-up. In the optical thickness method, the thickness of a dyed layer of fluid is measured by illuminating the fluid from beneath and relating the measured intensity (Cenedese and Dalziel, 1998), chromaticity (Afanasyev et al., 2009), or saturation (Zhang et al., 1996) to the thickness of the dyed fluid. This method has been applied to measure layer thickness in a number of two-layer systems (Linden and Simpson, 1994; Holford and Dalziel, 1996; Cenedese, 1998). Afanasyev et al. (2009) used a wedged-shape cuvette filled with the same concentration of dyes to calibrate the layer thickness, and then calculated the complete (both time and space dependent) depth field in a rotating fluid.

In our experiments we need to determine the fresh layer volume and also differentiate between fluids originating from the two different freshwater sources. For this purpose, we extend the existing one color optical thickness method to two colors. The relationship between intensity and thickness depends on the dye color, since attenuation coefficients are different for different dyes. To account for this, we determine a color-specific thickness calibration and apply it differentially according to the color of each pixel. We use the color ratio $\frac{R}{R+B+G}$ based on pixel values in the RGB colorspace to differentiate between two color of each pixel. After generating the two-dimensional (intensity-color ratio) calibration map, we determine the depth field for both the com-

bined two plume system and each separate plume. We conduct two non-rotating tests to determine the sensitivity of this two-dimensional thickness calibration to dilution and mixing. The technique is also validated with a known dye solution volume using both non-rotating and rotating control volume experiment. The technique is applied to the two-plume experiment. We calculate the bulge volume growth rate and the coastal current freshwater transport based on the measured layer depth field. Finally, we use the color ratio to determine the fraction of fluid at a given location in the plume originating from each sources.

2.2 Experimental setup

The experiments were performed in an annular rotating tank with $\mathbf{R} = 92$ cm and $\mathbf{r} = 22$ cm (Figure 2.1$\boldsymbol{a}$). The tank was mounted on a standing table, which was leveled such that the water level difference over one rotation is less than 0.1%. The table was rotating counter-clockwise throughout the experiment. The details of the rotating table facility are described in Horner-Devine (2006).

The experiment water tank was 25 cm deep and made of transparent Plexiglas, with a 0.5 cm thick Plexiglas lid placed above it to minimize the wind shear stress. A 91 cm $\times$ 122 cm $\times$ 0.8 cm LED Edge-lit light panel (Luminous Film, 2000 Lx daylight, 36.0 Watts) was placed under the clear water tank to provide a uniform light source. The difference in luminance from edge to center of the light panel is less than 2%. A sheet of Plexiglas with tracing film on top of it was attached between the light source and the tank bottom to diffuse the light entering the tank and further improve its uniformity. This small variation was further corrected using a reference image taken before the experiment. Images were acquired using a Panasonic PV-GS320 3-CCD color video camera that was located 155 cm above the light panel and

co-rotating with the water tank (Figure 2.1***b***). The video camera operated at 30 frames per second with a resolution of 760 × 480 (horizontal by vertical) pixels. The 3-CCD color video camera measured the intensity of light in the R, G, and B color bands separately and saved it as digital data on MiniDV tapes. It should be noted that the algorithm used to generate the final RGB values that were recorded on the tape is inherently lossy and the resolution of the system is somewhat degraded in this process.

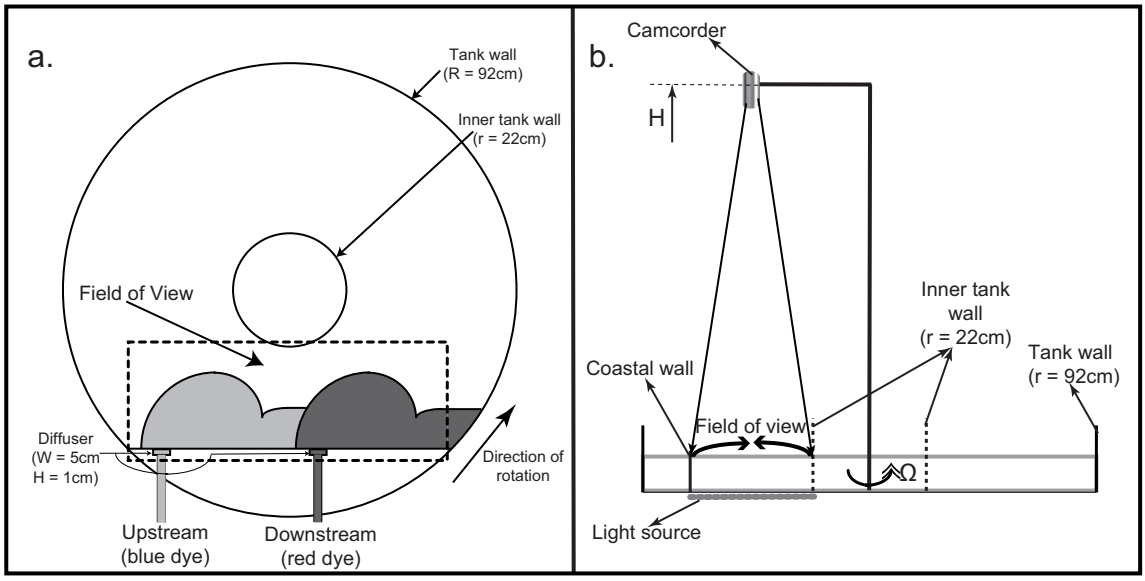

Figure 2.1: Schematic of the tank configuration viewed from above (***a***), and the rotating table viewed from the side (***b***)

.

Prior to each experiment, the tank was filled with salt water and allowed to achieve solid-body rotation by spinning up for 60 minutes, which is sufficient larger than the homogeneous spin-up time scale $E^{-1/2}f^{-1} = 5$ minutes, where $E = \nu/fH^2$ is the Ekman number (Wedemeyer, 1964). To generate the inflow fluids, 1 ml of pure food dye (deep blue and cherry red from ESCO FOODS Inc) was diluted to 2000 ml using

de-ionized (DI) water. The two sources of buoyant fluid were introduced into the tank just below the free surface of the ambient salt water through 5 cm $\times$ 1 cm diffuser boxes. Each diffuser consisted of a 6.25 cm^3 chamber filled with sponge to provide uniform outflow velocity distribution. They were affixed to the back of the coastal wall and separated by 18.7 cm. The flow rates were held constant by two identical magnetic drive centrifugal pumps (MARCH MFG INC, Model 893-001-03), and measured independently by two ball float flow meters (Key Instruments, 0 cm^3/s to 26.29 cm^3/s with 1.05 cm^3/s accuracy). The temperature of the buoyant source and the ambient tank water was measured before and during the experiments using a thermometer (DELTATRAK, -50 ^{o}C to 200 ^{o}C with 0.1 ^{o}C accuracy), and the salinity was measured with a refractometer (Cole-Parmer EW-02940-41, 0 to 10% with 0.1% accuracy).

2.3 Measurement technique

To calculate the thickness field of the two-layer buoyant rotating gravity current, the two-dimensional calibration map was generated based on the measured intensity-thickness and color ratio-thickness relationships. The thickness calibration included five different red and blue dye ratios: pure red, pure blue, 1:1, 1:3, and 3:1 (hereafter referred to as red, blue, b1:r1, b1:r3, and b3:r1, respectively). Each thickness calibration was done by filling a wedge-shaped cuvette which was attached to the coastal wall in the tank before the experiment.

2.3.1 Intensity-thickness relation

As described in Cenedese and Dalziel (1998, 1999), the dye attenuation theory derived from the classical Lambert-Beer Law gives the attenuation ratio

$$\frac{I(h,c)}{I_0(h,0)} = e^{-ach}, \tag{2.1}$$

where $I(h,c)$ is the transmitted intensity of light passing through a distance h of fluid with dye concentration c, and a is the attenuation coefficient. The effects of absorbed light by the tank bottom and lid, as well as the reflected light by various interfaces between different media are minimized by normalizing the intensity of dyed water to the transmitted intensity for the same thickness of undyed water, $I_0(h,0)$, at each pixel.

For a dyed fresh buoyant layer on an undyed salty ambient water layer, the actual relationship is approximately exponential but the asymptote is nonzero (Cenedese and Dalziel, 1998)

$$\frac{I(h_1,c;h_2,0)}{I_0(H,0)} = e^{-ach_1} + b, \tag{2.2}$$

where h_1 and h_2 are the thicknesses of dyed buoyant and undyed salty water, respectively, $H = h_1 + h_2$ is the total water thickness, and b is the asymptotic value of I/I_0 as the layer of dyed water thickness $h_1 \to \infty$ (i.e., $H \to \infty$). This relation was derived for monochrome image of a colored dye illuminated with white light. In our experiments, the color image is captured in a primitive RGB base, and the intensity is calculated by averaging the red, green and blue values for each pixel (Gonzalez et al., 2004). This relation allows us to normalize the intensity of light transmitted through the two-layer system to a one layer system with a total undyed thickness H (Figure 2.2***a***). This normalization is applied to each pixel in all images throughout the experiment. The background intensity I_0 is the reference image captured just before the fresh dyed water is injected into the tank.

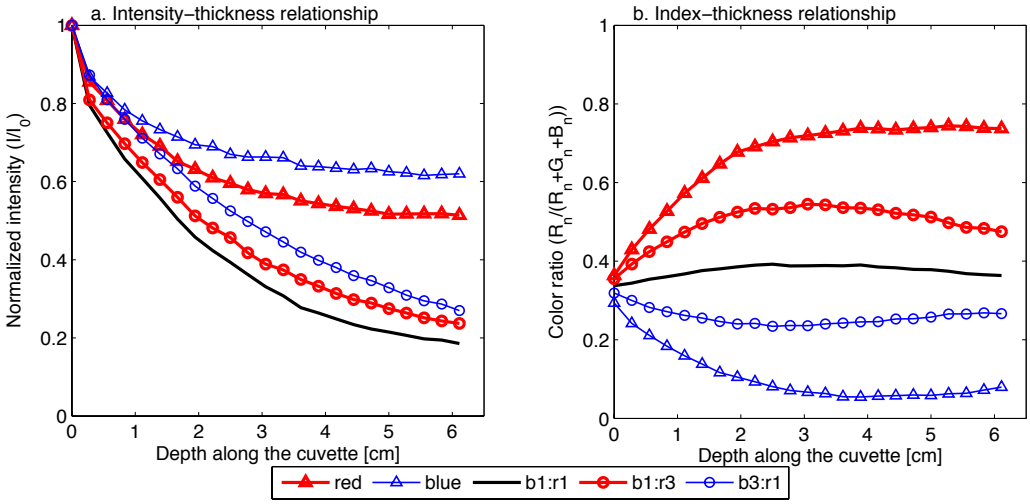

Figure 2.2: The layer thickness dependence of normalized intensity (I/I_0) for five different mixtures of blue and red dye solution (***a***) and the dependence of color ratio ($R_n/(R_n + G_n + B_n)$) for five different mixtures (***b***). All mixtures have $I/I_0 = 1$ at zero thickness, and decay exponentially with increasing thickness (Equation 2.2) with different attenuation coefficients.

2.3.2 Color ratio-thickness relation

In the two-dye experiment it is necessary to differentiate between the blue and red water masses. Figure 2.2***a*** suggests that the intensity-thickness relationships depend on dye colors. Therefore, the calibration uses a color ratio to define the relative color content at each point. We introduce a color ratio $Ci = \frac{R_n}{R_n+B_n+G_n}$ for this calibration, where R_n, G_n, and B_n are the R, G, B values normalized to the background R_0, G_0, B_0 values, respectively. In our experiments, the RGB color ratio was found more effective than other colorspace descriptions such as HSI, HSV or Lab that we tested. The profile of the color ratio Ci along the cuvette varies nonlinearly with the thickness of the mixtures in cuvette (Figure 2.2***b***). All five different mixtures have a color ratio = 0.3333 at zero thickness because the no-dye image has equal values

of R_n, G_n, and B_n. For thickness > 0 the color ratio increases for the red and b1:r3 cases, decreases for the blue and b3:r1 cases and remains approximately constant for the 1:1 mixture. Finally, all the lines become approximately flat for thickness greater than 3 cm. The decrease or increase tendence of color ratios for larger thickness region is due to saturation of the R or B values. This does not have a significant effect on our experiments since the thickness is generally below 3 cm and can be avoided by further diluting the source dye.

We combined the intensity-thickness profiles (Figure 2.2***a***) and color ratio-thickness profile (Figure 2.2***b***) to develop a two-dimensional calibration map (Figure 2.3). Thickness data were interpolated onto a 91 $\times$ 91 grid with intensity as abscissa, color ratio as ordinate, and thickness as color index.

2.3.3 Buoyant water volume calculation

The depth field generated by two-dimensional calibration is used to calculate the freshwater volume in the buoyant layer. It is important to note that the optical thickness method measures the effective layer thickness, defined as

$$h_e = \frac{1}{C_0} \int C(z) dz \simeq \frac{\bar{C}}{C_0} h_{real}, \tag{2.3}$$

where C and C_0 are the dye concentration in the plume and the source, respectively. Here, $\bar{C}$ is the vertically averaged dye concentration in the plume. In the two-plume system, mixing occurs both between the two dyed freshwater plumes and between each dyed freshwater plume and undyed salt water. The dye concentration is lower in the plume than in the source (i.e. $C < C_0$) because of mixing. Thus, the real thickness of dyed water in the tank is always larger than the effective thickness we measured, as the plume is continually diluted by entrained ambient salt water. However, since h_e

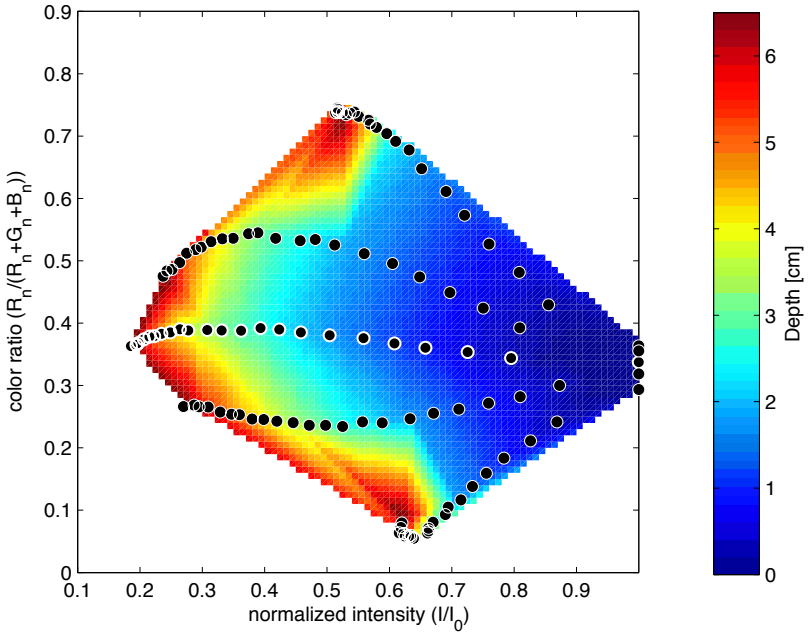

Figure 2.3: Two-dimensional (intensity-color ratio) calibration map generated from two thickness dependent relationships, with intensity as abscissa, color ratio as ordinate, and thickness as color index. Color ratio vs. normalized intensity of five different mixtures shown in Figure 2.2 and used to generate the calibration map are also plotted in the figure.

represents the amount of fresh water at each pixel location, it is the correct thickness for determining the volume of fresh water fluid masses. We calculated the total volume of fresh water by

$$V = \varepsilon \sum_{xpixels} \sum_{ypixels} (h_e), \tag{2.4}$$

where $\varepsilon = 0.0112\text{cm}^2$ is the area of each pixel.

2.4 Sensitivity and validation tests

2.4.1 Dilution sensitivity test

The optical thickness method is sensitive to the selected dye concentration because the intensity depends on the product of the dye layer thickness and the dye concentration. We conducted two tests to assess the sensitivity of the results to the dilution and hence optimize the selection of dye concentration. The normalized intensity decreases approximately exponentially with the increasing dye concentration for a fixed dye layer thickness of h = 3.25 cm (Figure 2.4). Cenedese and Dalziel (1999) suggested a value c_p as the maximum dye concentration, where the slope of the curve at c_p is four times of the slope at $c = 0$. The dye concentration should be in the range of $0 < c < c_p$ to prevent a small error in normalized intensity leading to a large error in concentration. In our experiment, we determined $c_p = 1.04$ ml/l for red dye and $c_p = 1.60$ ml/l for blue dye. We selected a dye concentration $c = 0.5$ ml/l which satisfied the above criteria for both dyes based on Equation 27 in Cenedese and Dalziel (1999) with a maximum depth of 6 cm.

Another dilution test was designed to verify that the diluted calibration would provide more detailed information in a small range without changing the overall intensity-thickness relationship. We diluted the 0.5 ml/l dye water source at three different dilution factors: 1:1, 1:3, and 1:7. The normalized intensity against modified thickness plot shows a good agreement when each original thickness is divided by its corresponding dilution factor (Figure 2.5). Therefore, the dilution does not affect the effective depth and the dyed water volume we are trying to calculate in our experiment.

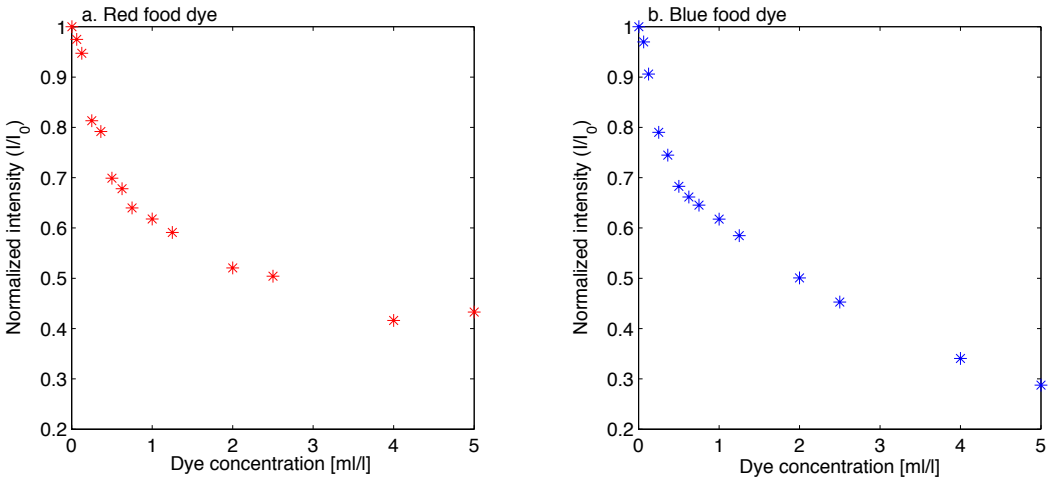

Figure 2.4: Relationship between normalized intensity (I/I_0) and the dye concentration for the red food dye ($\boldsymbol{a}$) and the blue food dye ($\boldsymbol{b}$).

2.4.2 Mixing sensitivity test

We used a cylinder mixing experiment to test the sensitivity of the two-color optical thickness method to mixing. Equation 2.3 suggests that the effective thickness should remain unchanged before and after the mixing. This is because the product of the real depth and the dye concentration will not change based on the mass conservation, although they both changed separately. The experiment employed a Plexiglas bottomless cylinder supported by two blocks on the bottom so that the buoyant water in the cylinder cannot expand laterally while the heavy salty water can exchange with the ambient water through the bottom. Selected volumes of fresh dye water were carefully introduced into the cylinder at the surface with a sponge end to minimize the initial mixing. We then used a piece of plastic plate to stir the surface dyed water gently. We took images both before and after the mixing for comparison. The ratio of intensity after mixing to before mixing was selected as a quantitative criterion to

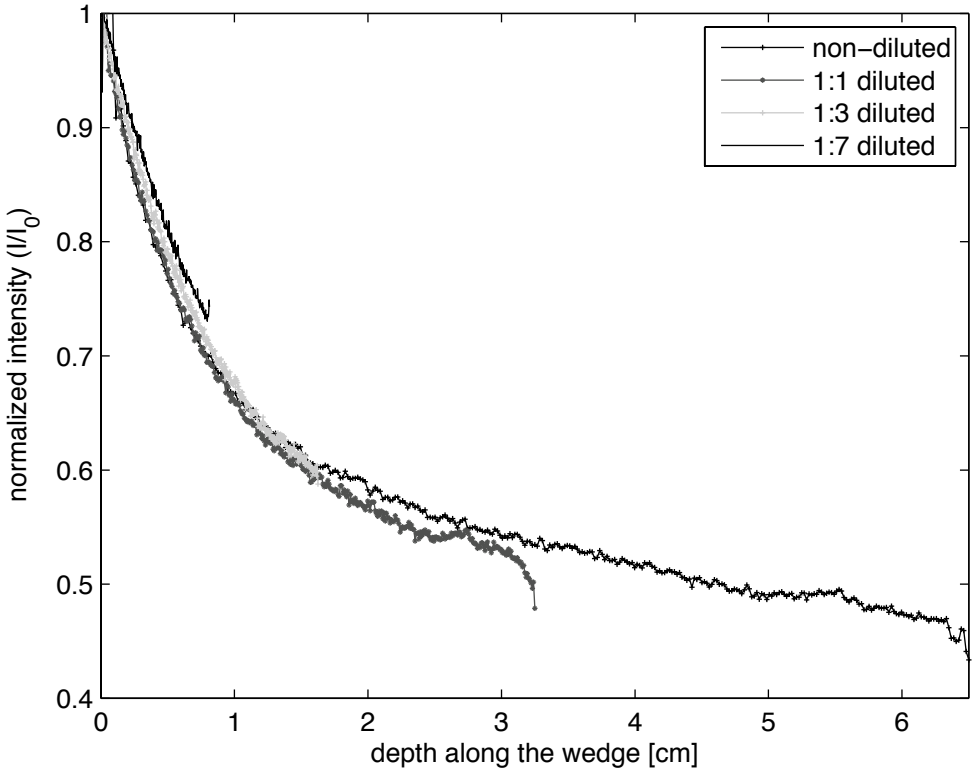

Figure 2.5: Red dye dilution test comparing non-diluted dye water to 1:1, 1:3, 1:7 DI water dilution. The normalized intensities I/I_0 are along the calibration wedge and depths for different dilutions are scaled by their corresponding dilution ratios.

determine whether mixing affected the effective thickness. We did the mixing test for both 0.5 cm and 3 cm thickness of blue and red dye water. For all tests the ratio was 1.0 with an average error of 0.61%.

2.4.3 Control volume Cylinder test

We carried out two validation tests to determine the accuracy of the technique. The bottomless cylinder used in the mixing test was placed in a non-rotating water tank

and partially filled with a known volume of buoyant dyed water to create a layer of known thickness over the salt ambient water. We used the dye concentration 1 ml/l and 0.5 ml/l (hereafter referred as non-diluted and diluted, respectively) in this test. We compared the thickness determined from the optical thickness technique with the known layer thickness to verify whether the measurement is accurate. For this calculation, the normalized intensity and color ratio were calculated from the cylinder RGB image for the 1cm by 1cm square at the center of cylinder. Then the depth was determined by interpolation in the parameter space defined by Figure 2.3 and averaged over the $1cm^2$ area. The calculated thicknesses based on the calibration map were plotted against the known thicknesses (Figure 2.6). Note that the calculated thickness is outside of our calibration space for depth greater than 5 cm for some undiluted dye. Slight differences in the color ratio and intensity between the calibration cuvette images and the experimental field of view appear to shift these points out of range of the calibration parameter space in Figure 2.3. For the remaining undiluted cases and the diluted cases, the calculated thickness shows good agreement to the known thickness, with the average error less than 10% for diluted dye and 20% for non-diluted dye. This is also consistent with the Cenedese and Dalziel (1999) criterion. A dye concentration of 0.5 ml/l is below the cut-off, while 1 ml/l is very near the cut-off which is expected a higher error in determine the layer thickness.

2.4.4 Rotating table volume test

A further test was devised to determine the ability of this technique to accurately measure the volume in a more complex flow, using the two-river experiment, as described in §2.2. In these experiments, inflow flow rate Q, table rotation period T and reduced gravity g' were varied. Here $g' = \frac{\Delta\rho}{\rho_0} g$, where $\Delta\rho = \rho_0 - \rho$ is the density dif-

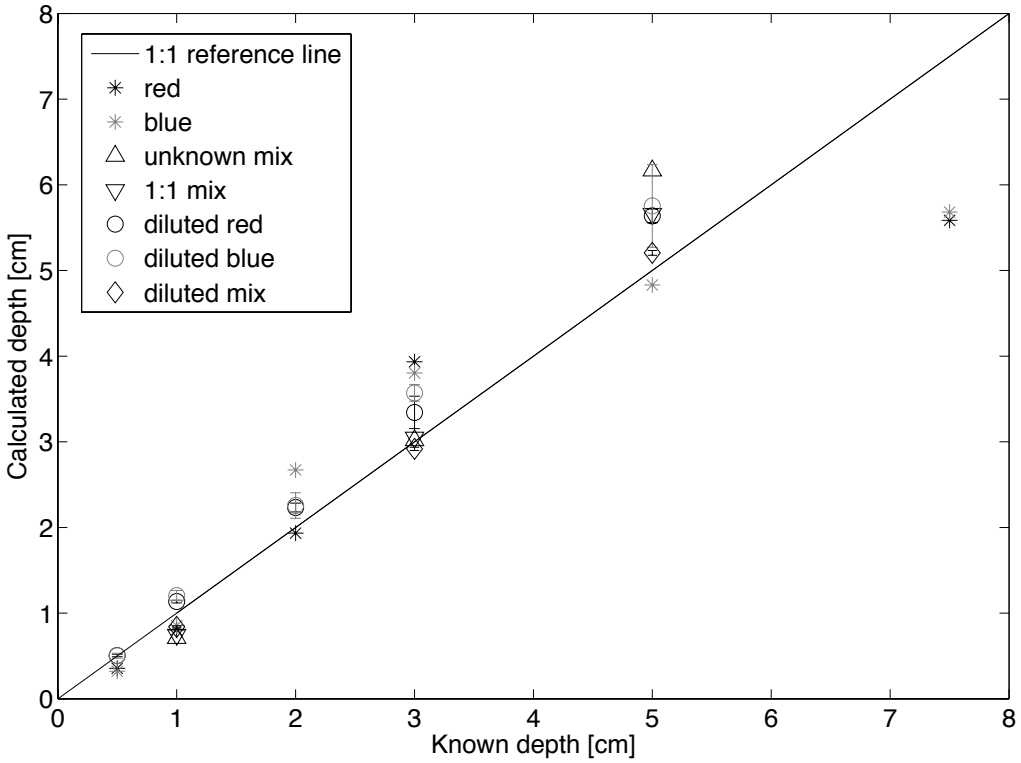

Figure 2.6: The cylinder layer thickness validation test with four non-diluted dyes (red, blue, unknown mix, 1:1 mix) and three diluted dyes (red, blue, mix). Errorbars are shown for the non-diluted dye cases. Many points with the layer thickness larger than 5 cm are missing because they are out of calibration map region.

ference between the source and ambient water, ρ_0 is the density of the salty ambient water, ρ is the density of fresh water, and g is the gravitational acceleration. For the particular run discussed here, the upstream and downstream source flow rates were equal, at 8 cm^3/s, the rotation period was 15 s, and the reduced gravity g' was 4.5 cm/s^2. We only considered the data from the first 25 s of the experiment, which was before the river plume left the camera field of view. We calculated the total volume based on the measured depth field, and compared it with the known inflow volume.

The raw RGB image of the two plumes and the corresponding computed depth field at 25s are shown in Figure 2.7. The upstream (blue) plume enters the system through a diffuser between $x = 3.5$ cm to $x = 8.5$ cm and the downstream (red) plume enters between $x = 27.2$ cm to $x = 32.2$ cm. The interaction of the two plumes will be discussed briefly in §2.5.

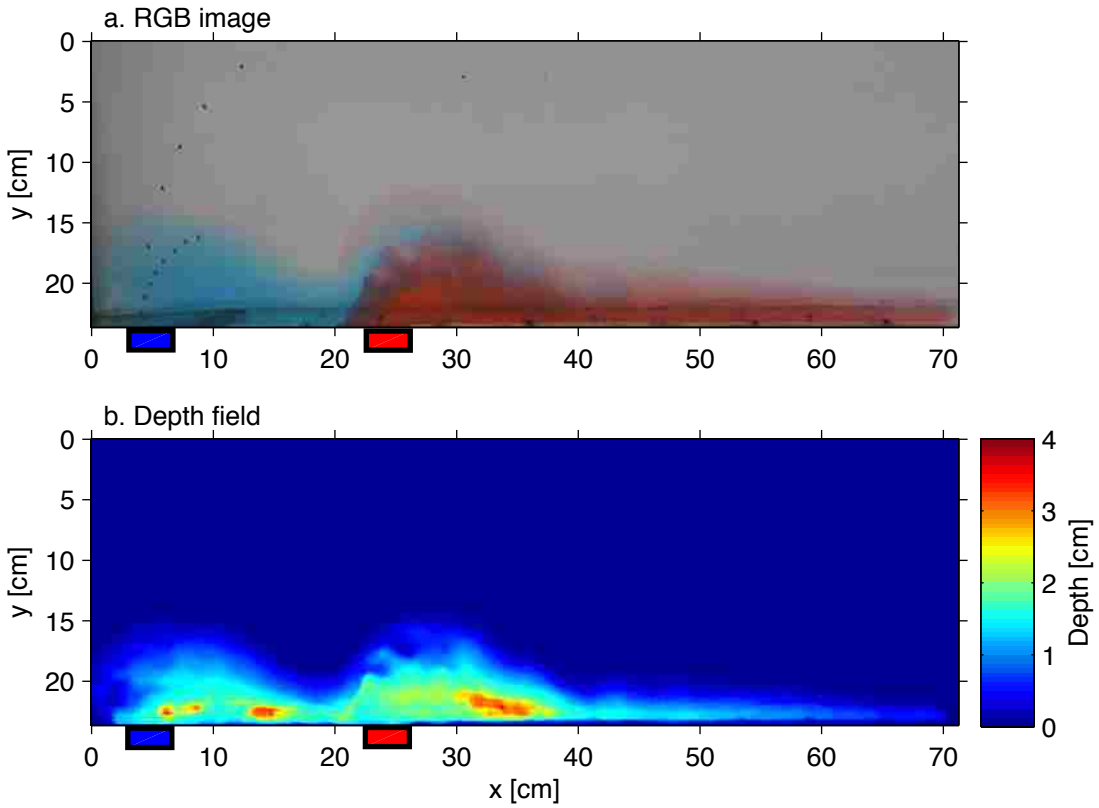

Figure 2.7: Raw RGB video image (***a***) and depth field (***b***) generated from the two-dimensional calibration map of Run7 after 25s. The blue and red boxes indicate the position of upstream and downstream sources, respectively.

If we assume the layer thickness is constant within one pixel, the volume of each pixel equals the area of that pixel multiplied by its average depth. The total volume

of freshwater in the two plume system can be calculated from Equation 2.4. This calculated volume should be equal to the volume of buoyant water discharged into the tank through both sources combined, which is given by

$$V_{in} = Q_{in}t. \tag{2.5}$$

The agreement between the measured plume volume and the freshwater input (Figure 2.8) confirms that the method accurately accounts for the entire plume volume. The root mean squared error for the first 25s is 6.41 cm^3, less than 4% of the total volume.

It is worth noting that this two-dimensional optical thickness technique may be sensitive to individual cameras. To address this question, we have recently introduced a research grade single-CCD bayer pattern camera (Point Grey Research Inc. GRAS-14S5C-C) for comparison. Although the pixel count on this camera is significantly higher than 3-CCD camera, the de-mosaicing of the Bayer information results in an effective pixel resolution that is approximately the same as the 3-CCD camera. The research grade camera is a 14-bit CCD and so the resolution of the color information is finer, although the effective camera resolution is not as good as 14-bit. The comparison between two cameras suggests that the calibration maps are different case to case, especially for the larger layer thickness. Two calibration maps are consistent at the smaller thickness region, while the research grade camera shows more variation in the deeper region. However, since most points in the plume are located in the shallower region, results from both two cameras satisfy the volume balance.

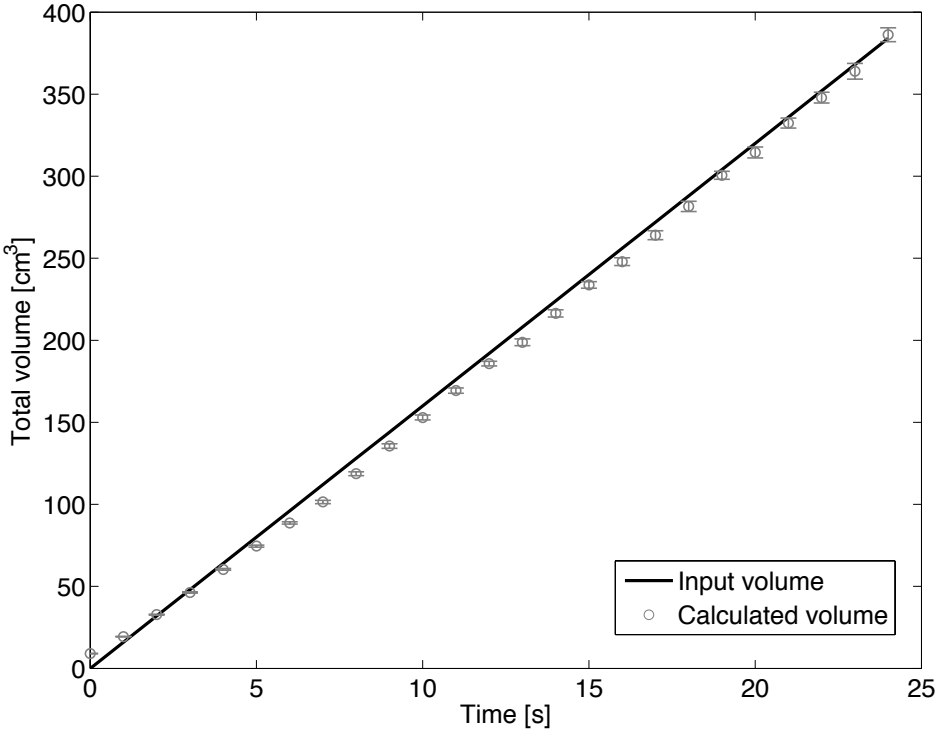

Figure 2.8: Comparison of the calculated total volume based on depth field (circles) to the total volume discharged into the tank (black line) before any buoyant fluid exists the view field ($0 < t < 25s$). The rms error is less than 4%.

2.5 Application

In this section we describe the application of the two-dimensional optical thickness method to the interaction of two river plumes in a two-layer rotating environment. As described in §2.2, blue and red dyes represented upstream and downstream fresh water rivers, respectively. Effective depth fields of both the red dyed plume and blue dyed plume were calculated, and the bulge volume and coastal current transport were subsequently determined from the depth field.

2.5.1 Separated bulge volume

One main purpose of the two-plume experiment is to test whether the downstream bulge volume reaches steady state due to the momentum flux from the upstream coastal current. To address this question, we calculate the downstream (red) bulge volume at various times. To evaluate the effective depth of each of the fluids in the mixing region, we assume their percentages vary linearly with the color ratio. Because there is some variation of color ratio in pure red and pure blue, we define the water with color ratio < 0.3 as water that originated from the upstream source, with color ratio > 0.5 as water that originated from the downstream source, and in between the percentage of the fluids from upstream increase linearly with the color ratio (Equation 2.6)

$$h\%_{downstream} = \begin{cases} 0 & \text{if } Ci \leq 0.3; \\ 0.5 + 5 \times (Ci - 0.4) & \text{if } 0.3 < Ci \leq 0.5; \\ 1 & \text{if } Ci > 0.5. \end{cases} \tag{2.6}$$

The result of plume separation at 6T is shown in Figure 2.9. The purple region between the two plumes may be explained by two possible reason. First, it is the mixing region between the two plume. The interaction between the upstream coastal current and the downstream bulge has high mass exchange and then forms this mixing region. Alternatively, it may be due to the subduction of the upstream plume under the downstream plume, as described by the two-plume theory in Cenedese and Lerczak (2008). In their analytical model and laboratory experiments, the two river plumes tend to align vertically with the upstream coastal current underneath the downstream plume because the upstream fluid has more opportunity to mix with the higher density ambient water. Viewed from above, it tends to be purple because a

portion of upstream plume is covered by the downstream plume.

In order to compute bulge volume we need to identify the region of the field of view occupied by the bulge and exclusive of the coastal current. This is somewhat complicated due to the fact that the bulge expands in the alongshore direction. We assume that the bulge has a linear alongshore growth rate and adjust the field of view for our image interrogation accordingly. For the upstream bulge, the situation is different because it would never continue to grow laterally because it hits the downstream plume. We calculated the upstream and downstream bulge volume separately based on Equation 2.4 from their depth fields. Both plumes grow at exactly the same rate and the sum of their volume is equal to the total entering freshwater volume (Figure 2.10 insert).

2.5.2 Two river plumes evolution

Six examples of two plume evolution are shown in Figure 2.11 ***a, b, c, d, e*** and ***f***, corresponding to $t = T, 5T, 10T, 20T, 30T$, and $37T$ ($T = 15$ s), respectively. The upstream plume reaches the downstream plume after $0.6T$, and the two plumes begin to interact with each other at the end of first period (Figure 2.11***a***). After one rotation period, the downstream bulge tends to grow alongshore, while the upstream bulge tends to grow offshore and wrap around the downstream plume bulge (Figure 2.11***b*** and ***c***). Later, the downstream bulge is sucked into the upstream bulge, forming a bigger re-circulating bulge. A small bulge separates from the big bulge and propagates downstream (Figure 2.11***d***). This cycle continues, i.e. the big bulge accumulates the inflow fluid and becomes unstable, a small bulge separates from the big bulge and propagates downstream, then the big bulge returns to its stable state (Figure 2.11***e*** and ***f***). It is interesting to note that fluid from the downstream source is drawn all

the way to the upstream source and even appears to be entrained into the outer edge of the upstream plume (Figure 2.11*e*). We also observe that the width of the band of mixed fluid between the two plumes increases around $t = 5 - 10T$ and then decreases afterwards. The reasons for this will be investigated in future studies.

2.5.3 Coastal current transport

The coastal current in the river plume system is held to the wall due to Coriolis forces. The flow approaches a state of geostrophic equilibrium in which buoyancy and Coriolis forces are in balance and further release of potential energy is impossible (Griffiths and Hopfinger, 1983).

The alongshore velocity in the coastal current can be derived based on a two-layer model that has a quiescent lower layer and geostrophic cross-shore momentum balance. Thus,

$$u = -g\frac{\Delta\rho}{\rho_0 f}\frac{\partial h}{\partial y} = -\frac{g'}{f}\frac{\partial h}{\partial y}, \tag{2.7}$$

where h is the buoyant plume thickness, u is the alongshore velocity, f is the Coriolis parameter. Note that ρ, h, u are depth-averaged values, but they can vary as a function of y, the cross-shore distance. The alongshore coastal current transport can be calculated by integrating the velocity over the coastal current section area,

$$Q_{cc} \equiv \iint u dA = \int_0^W \int_{-h}^0 u dz dy = \int_0^W -\frac{g}{f\rho_0}\frac{\partial \Delta\rho h}{\partial y} h dy. \tag{2.8}$$

As suggested by Fong and Geyer (2002) a freshwater transport is defined based on the further assumption: that the density anomaly is approximately proportional to the salinity anomaly, $\Delta\rho = \beta\Delta S$, where $\beta = 0.79$ kgm^{3}psu^{-1}. Thus, the freshwater

transport is

$$Q_{fcc} \equiv \iint u\frac{\Delta S}{S_0}dA \approx \frac{1}{\beta S_0}\int_0^W \int_{-h}^0 u\Delta\rho dz dy = \frac{1}{\beta S_0}\int_0^W -\frac{g}{f\rho_0}\frac{\partial(\Delta\rho h)}{\partial y}\Delta\rho h dy. \tag{2.9}$$

Here h is the real plume depth including the initial fresh dyed water and the salty undyed water which has been entrained into the plume during the mixing process. As discussed in §2.3.3, the measured effective depth is a function of the concentration ratio times the real depth (Equation 2.3). Assuming that the water in the plume is well mixed, one can easily convert the concentration ratio to the density anomaly ratio

$$\frac{C}{C_0} = \frac{V_F}{V_T} = \frac{\Delta\rho}{\Delta\rho_{\max}}, \tag{2.10}$$

where V_F and V_T are the fresh water and total water volume, respectively, and $\Delta\rho_{\max}$ is the density difference between inflowing fresh water and ambient salty water, $i.e. \Delta\rho_{\max} = \rho_{ambient} - \rho_{inflow}$.

Substituting Equation 2.3 and Equation 2.10 into Equation 2.9, the freshwater transport is

$$Q_{fcc} = -\frac{g(\Delta\rho_{\max})^2}{\beta S_0 f\rho_0}\int_0^W \frac{\partial h_e}{\partial y}h_e dy = -\frac{g'_{\max}\Delta\rho_{\max}}{\beta S_0 f}\int_{h_e@(y=0)}^{h_e@(y=W)} h_e dh_e, \tag{2.11}$$

where $g'_{\max}$ is the reduced gravity based on $\Delta\rho_{\max}$. For a given inflow and ambient salinity (density), the freshwater transport is only a function of the coastal current effective depth, h_e. From the measured coastal current effective depth field, we can

calculate the freshwater transport by numerically integrating the effective depth over its entire width

$$Q'_{fcc} = -\alpha Q_{fcc} = -\alpha \frac{g'_{\max} \Delta\rho_{\max}}{\beta S_0 f} \sum_{i=1}^{N} h_e(i)[h_e(i+1) - h_e(i)], \tag{2.12}$$

where α is an $\mathcal{O}(1)$ empirical constant. We can then determine the value of α based on the total volume balance. The calculated coastal current transport with $\alpha = 1$ are shown in Figure 2.12.

Theoretically, we can derive a freshwater mass conservation equation similar to the one in §2.4.4. The volume of buoyant water discharged into the tank should be equal to the calculated plume volume within the camera field of view plus the freshwater transport out of view through the coastal current, expressed as

$$V_{in} = Q_{in}(t - t_0) = V_{field} + \sum Q'_{fcc} \Delta t. \tag{2.13}$$

For this case, the empirical constant α must be 0.6 to balance the flow into and out of control volume (Figure 2.13). This relatively low empirical constant might be due to two possible reasons. Imaging of the region very near the coastal wall is degraded due to the presence of the bottom of the wall in the images. This may artificially increase the transport estimate. Another plausible explanation is that the two-layer system with a quiescent lower layer is not a proper assumption in this two plume system if the interaction between two plumes is similar to scenario $\mathcal{A}$ in Cenedese and Lerczak (2008). In this case, it is actually a three-layer system with a quiescent bottom layer. The middle (blue) and upper (red) layer cannot be considered a simple geostrophic current together.

2.6 Conclusion

A modified optical thickness method is used to calculate the depth field of two interacting water sources by combining the reduction in intensity of transmitted light and the RGB color ratio of a dyed buoyant layer. A procedure to generate a two-dimensional calibration map from two depth-dependent relationships is presented. The measured depth field is used to calculate the total buoyant gravity current volume in the field of view. The technique is successful in measuring the dyed freshwater depth in a cylinder depth test with 10% average error. This technique was then applied to a two plume experiment to measure the depth field of both plumes. Prior to the time that the plume water exits the field of view, the technique is successful in calculating the buoyant gravity current volume to within 4% error of prescribed volume input.

We also formulate an expression for the freshwater transport in the coastal current based on the obtained depth field and the assumption that the coastal current in a cross-shore geostrophic balance. The computed transport closes the freshwater budget for the system, but requires an empirical coefficient $\alpha = 0.6$. Although this coefficient is significantly below unity, the fact that the computed transport only departs from that needed to close the balance by a constant implies that our expression captures the principal dynamics of the system.

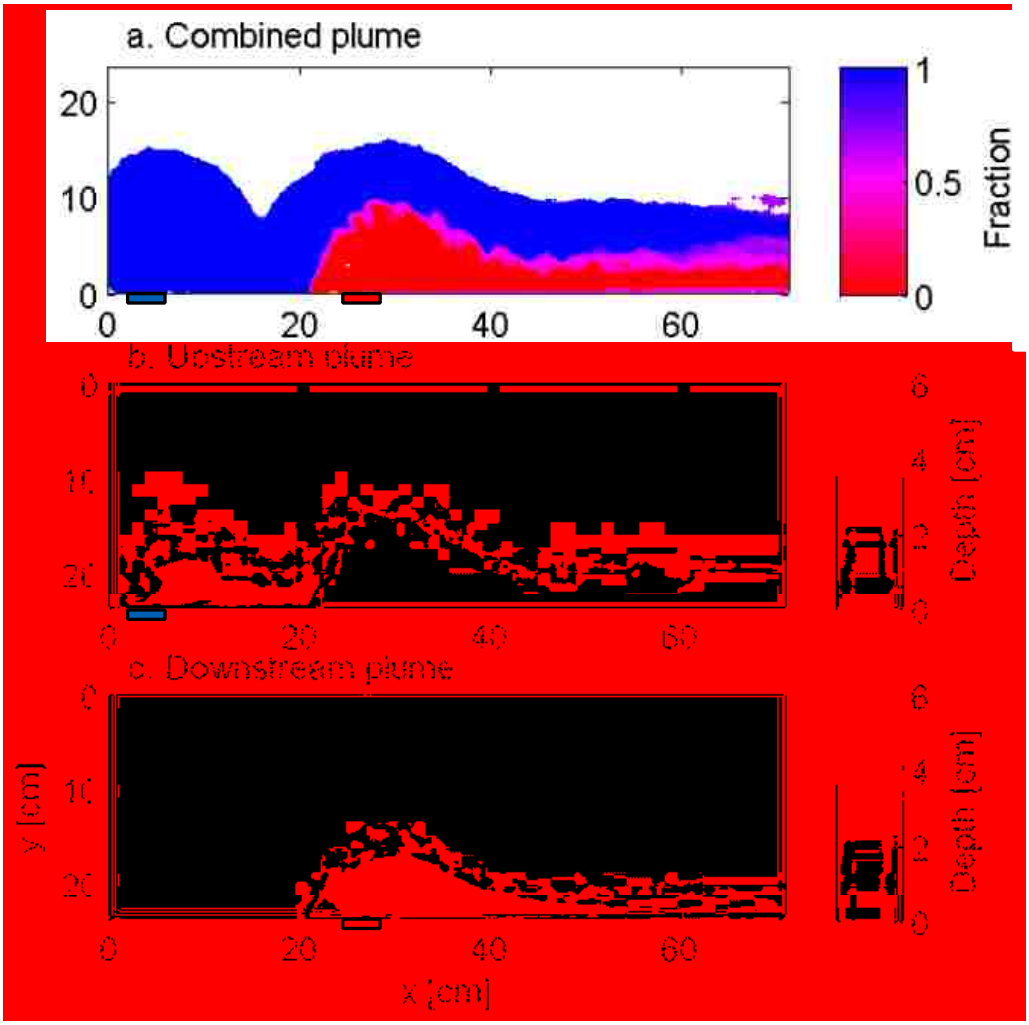

Figure 2.9: Discrimination of red and blue source fluid in the plume. Combined plumes showing fraction of blue source fluid at each pixel at t = 6T (***a***), upstream (blue) plume depth field (***b***) and downstream (red) depth field (***c***). The purple region in panel (***a***) indicates the mixing region. The blue and red boxes indicate the position of upstream and downstream sources, respectively.

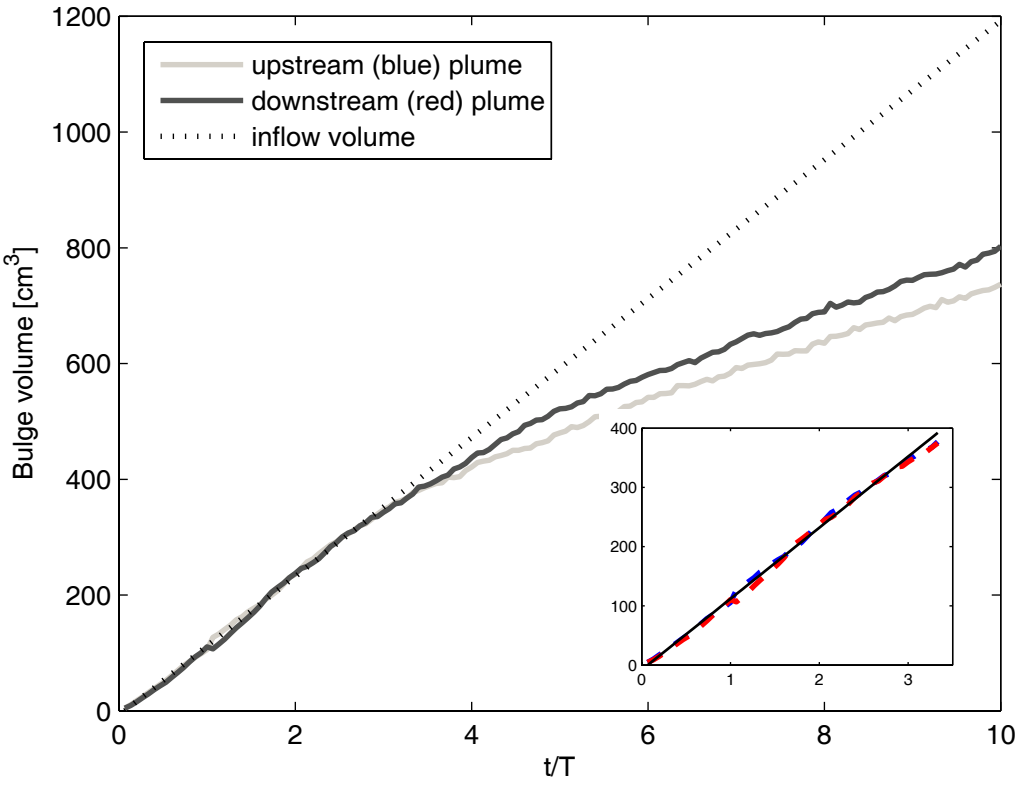

Figure 2.10: Upstream and downstream river bulge volume growth ($0 \leqslant t \leqslant 10T$) and comparison to the real inflow volume. The insert is the zoom-in of first 3.5 T. Blue and red dashes represent the upstream and downstream plume, respectively

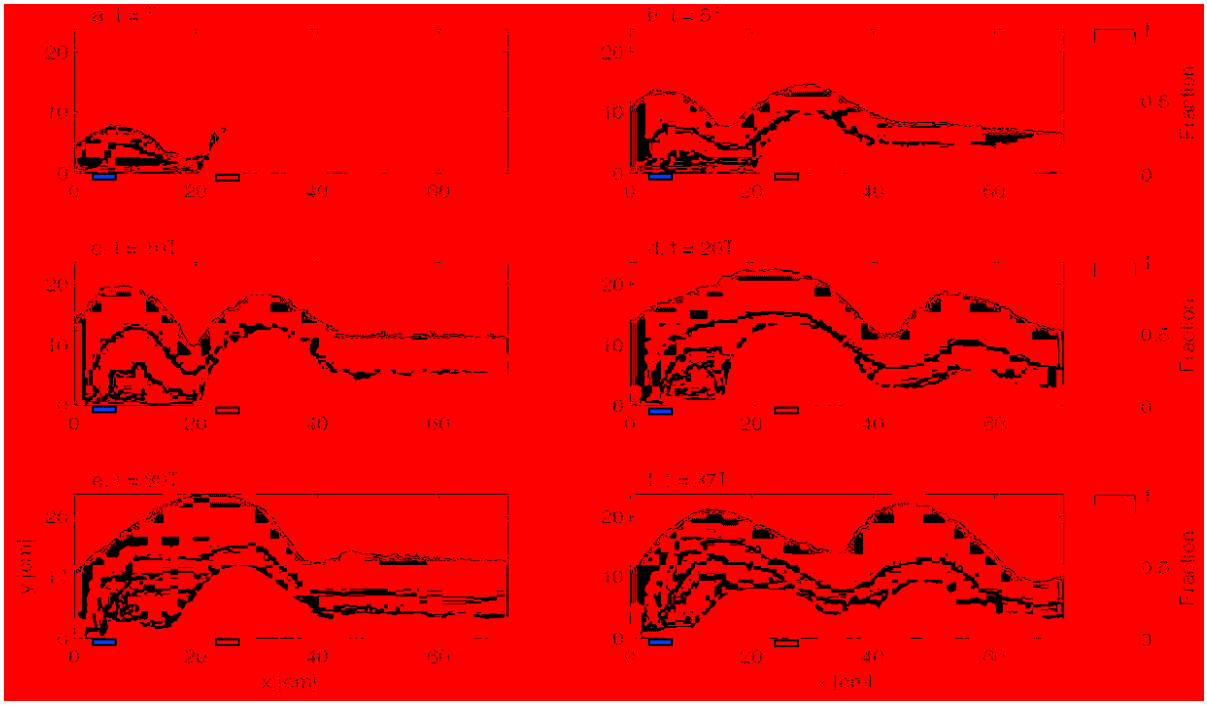

Figure 2.11: Fractional source content of two plume system for run 7 at t = T (***a***), t = 5T (***b***), t = 10T (***c***), t = 20T (***d***), t = 30T (***e***), and t = 37T (***f***). The 0.05 cm, 1 cm, 3 cm, and 5 cm depth contours are shown. Blue and red boxes indicate the position of upstream and downstream sources, respectively.

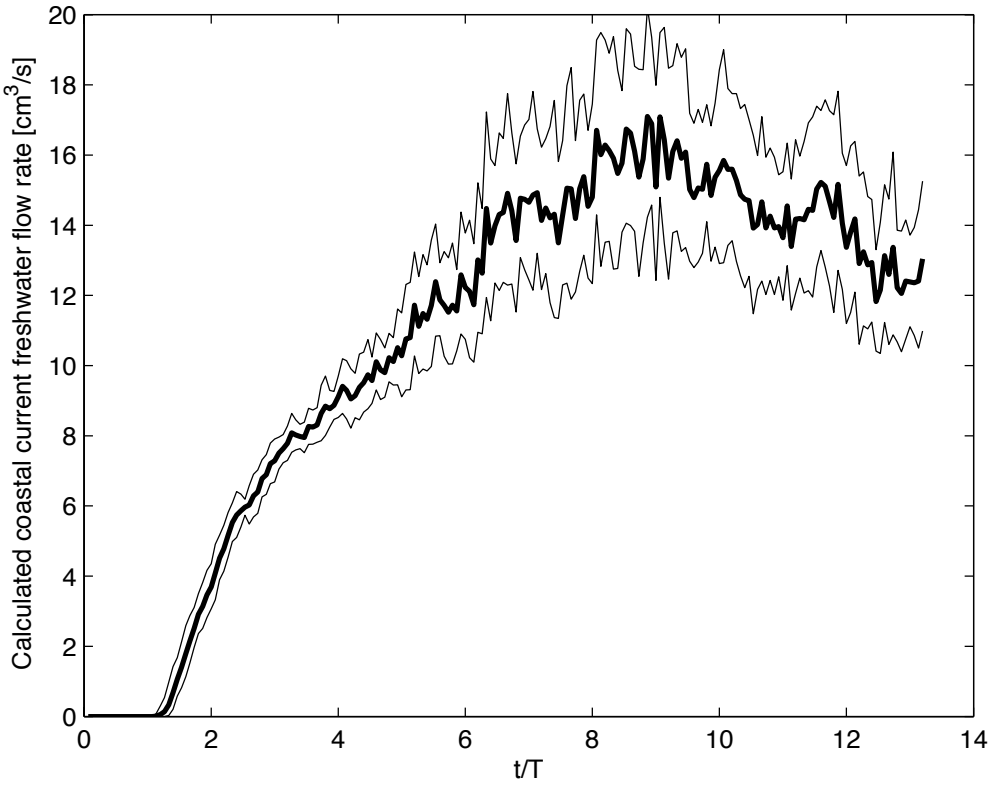

Figure 2.12: Freshwater coastal current transport computed by Equation 2.12 with the empirical coefficient $\alpha = 1$ ($0 \leqslant t \leqslant 13T$) (thick line). Two thin lines represent the error bound, based on the standard deviation of coastal current depths.

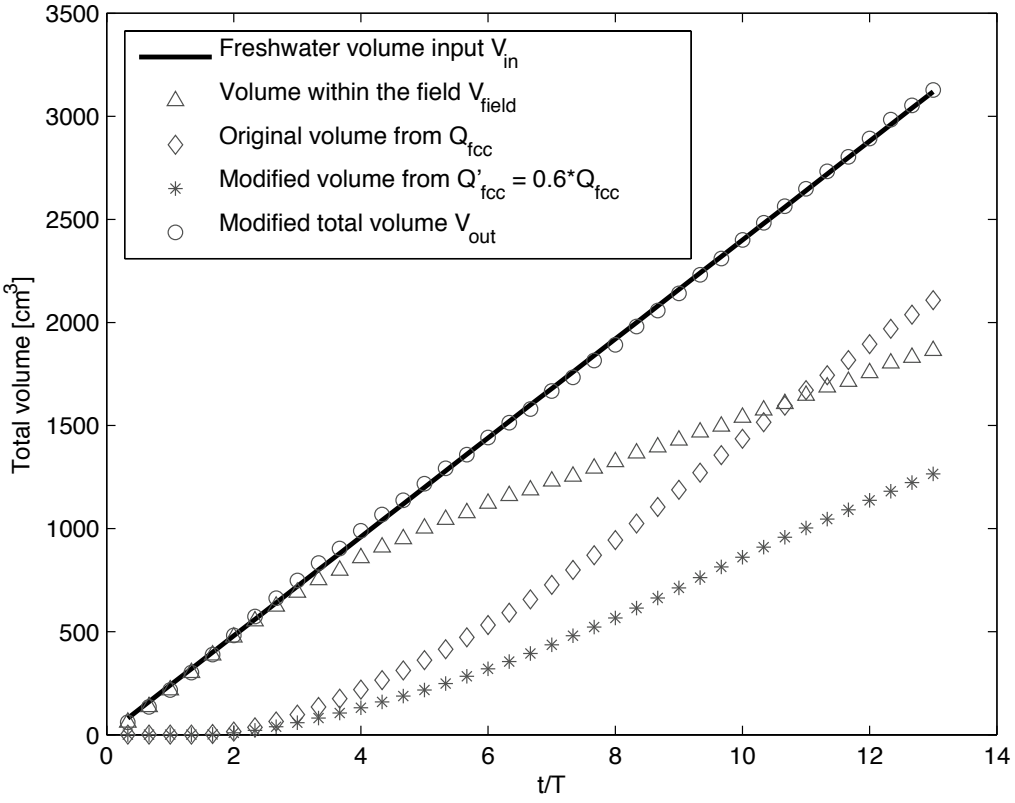

Figure 2.13: Total freshwater volume balance ($t = 0 - 13T$). The total volume input (black line) is balanced by the total output ($\circ$), which is the sum of volume within the field ($\triangle$) plus the freshwater transport in the coastal current ($*$). Note that the modified freshwater transport ($Q'_{fcc} = \alpha Q_{fcc}$) equals empirical coefficient ($\alpha = 0.6$) times the calculated freshwater transport ($Q_{fcc}(\diamondsuit)$).

Chapter 3

IMPACT OF LATERAL SPREADING ON BUOYANCY FLUX IN A RIVER PLUME [2]

We investigate the relationship between lateral spreading and mixing in stratified gravity currents by comparing laterally confined and unconfined currents in a series of laboratory experiments. The vertical turbulent buoyancy flux is determined using a control volume approach coupled with velocity and density fields derived from combined particle image velocimetry (PIV) and planar laser induced fluorescence (PLIF). Lateral spreading is determined in the unconfined experiments based on plan-view imaging using the Optical Thickness Method (OTM). We find that lateral spreading dramatically modifies the plume structure; the spreading plume layer consists of approximately linear density and velocity profiles that extend to the surface, whereas the channelized plumes have regions of uniform density and velocity near the surface. Lateral spreading decreases the average plume density. However, the local turbulent buoyancy flux in the spreading experiments is approximately equal to that in the confined experiments. This apparent paradox is resolved when the plume areas are taken into account. The total mixing integrated over the horizontal plume area is almost an order of magnitude higher in the spreading experiments. Thus, spreading does not appreciably alter the turbulent mixing processes at the base of the plume. However, it significantly increases the area over which this mixing occurs and, through this

[2]This chapter duplicates a manuscript of the title as 'Laboratory investigation of the impact of lateral spreading on buoyancy flux in a river plume' by Yuan, Y and A. R. Horner-Devine which currently submitted to Journal of Physical Oceanography. All text, tables and figures are identical with the exception of the relabeling of figures, tables and equation number.

mechanism, increases the net dilution of river water at a fixed distance from the river mouth. Finally, we hypothesize that the spreading does not significantly increase the local turbulent buoyancy flux because spreading occurs preferentially near the surface, whereas buoyancy flux is greatest in the core of the current.

3.1 Intronduction

Rivers play a critical role in the exchange of material between land and the ocean. The concentration of river-borne matter and the buoyancy of river-influenced coastal waters is determined in large part by the intense mixing that occurs in the initial adjustment of the freshwater as it is discharged into the ocean. During this process outflowing buoyant river water propagates along the ocean surface and expands laterally due to the horizontal baroclinic pressure gradients. Most field observations model plume propagation and mixing using theory derived from classical two-dimensional laboratory experiments, however, which do not account for the possible effects of lateral spreading. In this contribution we compare the dynamics and mixing in laboratory generated constant source buoyant gravity currents with and without lateral spreading.

Much of our understanding of gravity current propagation is based on early lock exchange experiments, in which fluids of different densities are initially separated by a vertical barrier and then released suddenly by removing the gate. Based on potential flow theory von Karman (1940) predicted that the denser fluid current ρ_i propagates into a semi-infinite lighter ambient fluid of density ρ_0 with a mean velocity

$$U_f = \sqrt{2g'h_f}, \tag{3.1}$$

where $g' = \frac{\Delta\rho}{\rho_0}g$ is the reduced gravity, g represents gravity, $\Delta\rho = \rho_0 - \rho_i$ is the density difference between two fluids, and h_f is the frontal depth. This was later revisited by Benjamin (1968), who arrived at the same conclusion based on energy-conserving theory for inviscid fluids. More recently Shin et al. (2004) performed experiments on surface gravity currents in a deep ambient fluid, suggesting that the Froude number

$Fr = U/\sqrt{g'h}$ approaches 1 in the limit of an infinitely deep environment rather than the larger value of $\sqrt{2}$ predicted by classical work of von Karman (1940) and Benjamin (1968).

There are two effects not considered in these classical theories, which are important to the interpretation of river plumes as gravity currents. First, the lock exchange experiments involve a fixed volume of fluid, while the river inflow is fed by constant freshwater flux or tidally varying discharge from the estuary. Simpson (1997) showed that the frontal speed of a lock-exchange flow decreases with the fractional depth while a constant flux flow does not depend on the fractional depth. Hallworth et al. (1996) concluded that the entrainment into the head of a constant flux gravity current is smaller than in the release of a fixed volume of fluid. They attributed this difference to the continual replenishment of fluid in the head by the constant feed of undiluted fluid from the tail. They compared the entrainment mechanisms and regions for constant-volume and constant-flux gravity currents. Unlike a concentrated frontal bore followed by a thin tail in the fixed volume case, the depth of the front and tail were the same in the constant flux case. Kilcher and Nash (2010) described a recent field study on the Columbia River plume and showed that varying flowrates result in significant differences in plume structure, mixing and momentum balance.

A second important difference is that most lock exchange experiments use a configuration in which the gravity current is confined in a straight channel. A few previous studies use axisymmetric configurations such as sector tanks to incorporate the lateral effects (Britter and Simpson, 1978; Chen, 1980; Didden and Maxworthy, 1982; Huppert and Simpson, 1980; Patterson et al., 2006). Simpson (1997) stated that the streamwise vorticity structures are different when spreading dense fluid in a sector tank instead of a parallel channel. Patterson et al. (2006) also observed the modifica-

tion of vortex structure on the dense fluid from the 10 degree sector tank lock release. Dense fluid propagates at a relatively constant depth in the two-dimensional case, while in the axisymmetric case, most of the dense fluid appears to be concentrated within the front bore. Chen (1980), followed by Wright et al. (1991) and Maclatchy (1999), considered the radially spreading surface flow generated from a center vertical buoyant jet. Didden and Maxworthy (1982) compared the spreading of plane and axisymmetric gravity currents in laboratory experiments, suggesting that the frontal propagation relationships were different in those two configurations. Cantero et al. (2007a) showed that in the cylindrical configuration Kelvin-Helmholtz (K-H) vortices formed at the interface, eventually generated a vortex ring. The concentrated vorticity at the head of the cylindrical current initially intensifies due to vortex stretching (Patterson et al., 2006), and eventually the current has a highly turbulent front with a relatively shallow calm body (Cantero et al., 2006). There are two possible explanations for the shallow calm body. First, as discussed above, the volume of the gravity current is fixed with no continuous source to support the current. Second, the body may be thinned due to spreading effects. The front is followed by a backward-facing hydraulic jump, which is the result of a post-rarefaction wave that is reflected from the origin and propagates radially outward more rapidly than the front itself (Rottman and Simpson, 1983, 1984). Ungarish and Zemach (2005) provided a complete overview of the modeling of high Reynolds number gravity currents in two-dimensional and axisymmetric configurations. Such flows are of interest in describing the spreading of freshwater discharging from a river mouth.

Although these two configurations model spreading effects, the current is either forced to spread cylindrically or modified by the tank shape in these cases. At river mouths the freshwater is initially channelized in the estuary and subsequently begins

to spread once it reaches the coastal ocean. During this transition to the unconfined state it undergoes vertical and lateral adjustments and the spreading rate is set dynamically based in part on the initial momentum and the density of the buoyant layer. Thus, the dynamics of a constant-source unconfined gravity current is expected to be different from both the axisymmetric and the sector tank gravity currents. To author's knowledge, the laboratory and numerical investigation of freely propagated gravity currents has only been reported by Rocca et al. (2008), who focused on the bottom roughness effects on three-dimensional gravity current propagation.

Luketina and Imberger (1987) presented field observations of a tidally pulsed buoyant plume and found an overturning roller at the plume front. Surface water behind the front overtook the roller and formed an energetic mixing area following the front, consistent with the previous laboratory work from Britter and Simpson (1978). Other field observations (Wright and Coleman, 1971; Hetland and MacDonald, 2008) suggest that the lateral spreading of buoyant plumes should behave like a lateral lock-exchange flow, where the spreading rate is proportional to the local internal gravity wave speed, c: $DW/Dt = 2c$, where W is the plume width. Since the streamwise propagation speed of the buoyant layer well behind the front is initially set by the outflow momentum, this implies that the lateral spreading depends on the inflow Froude number $Fr_i = U_0/\sqrt{g_0' H_0}$, where U_0, g_0' and H_0 are inflow velocity, reduced gravity and water depth, respectively. Hetland and MacDonald (2008) and Chen et al. (2009) both suggested that lateral spreading might be significantly affected by the mixing in the near-field region and that the spreading rate is complex. The spreading process in a geophysical scale plume is not well represented by the previous laboratory experiments performed with cylindrical configurations or in sector tanks.

Many laboratory gravity current experiments assume inviscid and immiscible flu-

ids. Previous studies show that turbulent mixing is generated by shear-induced instabilities (i.e., Kelvin-Helmholtz (K-H) instabilities and Holmboe instabilities). Thorpe (1973) used laboratory experiments to investigate the evolution and development of K-H instabilities and turbulence at the interface of a stratified two-dimensional shear flow. Christodoulou (1986) provided a complete overview of turbulent mixing at the density interface through theoretical analysis and re-examination of available buoyant overflow experimental data (Ellison and Turner, 1959; Chu and Vanvari, 1976; Buch, 1980; Pedersen, 1980). He developed a general law that the entrainment rate ($E = w_e/U$) is a function of the bulk Richardson number, $Ri_b = \frac{g'H}{U^2}$, in which w_e is the vertical velocity through the reference isopycnal, U is the characteristic horizontal velocity, and H is the plume thickness. This conclusion suggested that the mixing took place through vortex entrainment for small bulk Richardson number (supercritical conditions) and by cusp entrainment at $Ri_b > O(1)$ (subcritical conditions). Both mechanisms are active in the intermediate range when Ri_b is near its critical value of unity.

Following from Ivey and Imberger (1991), MacDonald and Geyer (2004) used the non-dimensional variable $\frac{\varepsilon}{\Delta u g'}$ to represent how much mean flow energy that is converted into turbulent kinetic energy by shear flow. We adopt the scale from MacDonald and Chen (2012) using the turbulent buoyancy flux, $B = \frac{g}{\rho_0}\overline{\rho' w'}$, in place of ε. B and ε are directly proportional if the turbulence is homogeneous and stationary, $P = \varepsilon + B$. Here ε represents the rate of dissipation of turbulent kinetic energy (TKE), and $P = -\overline{u'w'}\frac{\partial u}{\partial z}$ is the TKE production. In addition, Ivey and Imberger (1991) suggested that K-H billows will have an overturn Froude number $Fr_T = (L_o/L_t)^{2/3}$ close to unity, where $L_o = (\varepsilon/N^3)^{1/2}$ is the Ozmidov scale, L_t is the representative turbulent length scale and $N^2 = -\frac{g}{\rho_0}\frac{\partial \rho}{\partial z}$ is the buoyancy frequency.

Hence the prediction from the above is that the mixing efficiency $R_f = \frac{B}{P}$ for this particular mechanism should be around 0.2. MacDonald and Chen (2012) suggested that a quadratic relationship exists between mixing and spreading parameters from which they concluded that lateral spreading affects the energetics of the local turbulence field. Their theoretical model based on the longitudinal stretching of K-H billows, was used in the analysis the 2007 Merrimack River data set.

The manuscript is organized as follows. In Section 2, we describe the confined and unconfined experimental configurations and the two main measurement approaches. We present the experimental results in Section 3. Finally, in Section 4 we describe the observed relationship between spreading and mixing, and presents possible hypothesizes to explain the result.

3.2 Experimental setup

A schematic of the laboratory set-up is shown in Figure 3.1. All experiments were conducted in a water tank (hereafter called the plume basin), which is 400 cm long, 250 cm wide and 50 cm deep. The buoyant water source was a 600 l constant head tank located 5 m above the level of the plume basin. The inflow was introduced into the plume basin through a small estuary tank, containing a diffuser board and a honeycomb to achieve uniform flow characteristic and a 50 cm channel section. Each experiment started by opening the estuary gate and the buoyant water valve simultaneously. After propagating across the plume basin, mixed fluid exited the system over an adjustable weir at the downstream end of the basin.

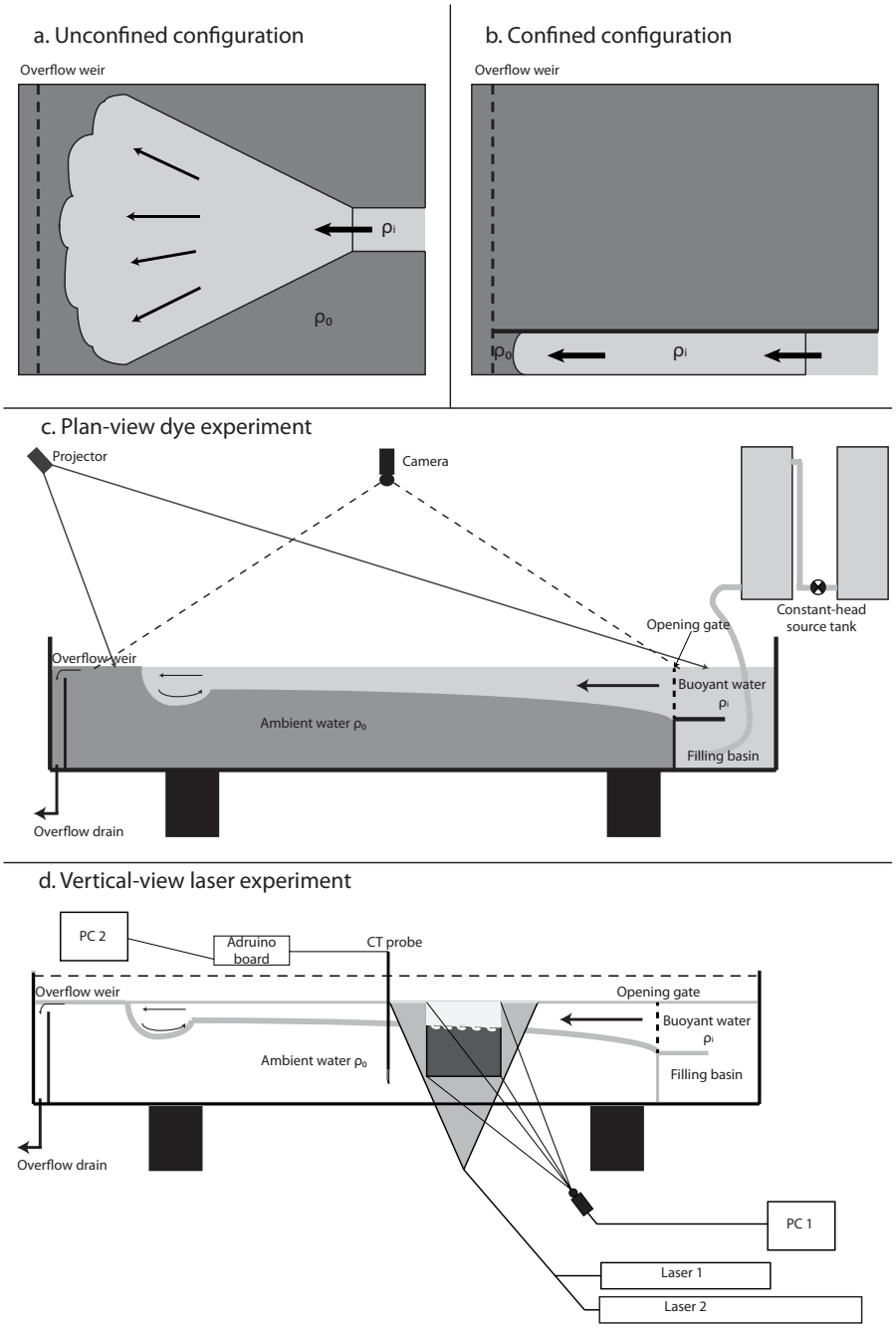

Figure 3.1: Schematic of laterally a) unconfined (spreading) and b) confined (channelized) gravity currents and schematics of experimental facility and instrumentation for c) the plan-view dye experiments and d) vertical-view laser experiments. The plan-view imaging was done only in the spreading experiments (a), while the vertical-view laser experiments were repeated for both spreading (a) and channelized (b) experiment.

Two configurations were designed with different estuary tank locations to determine how lateral spreading affects plume structure. In the unconfined case the estuary tank was located at the center of one end of the plume basin (Figure 3.1a). By lifting the gate and opening the valve, the buoyant fluid was released from the estuary channel into the ambient water where it was allowed to spread freely. For the confined case the estuary tank was oriented between the tank wall and a vertical plastic wall so that these formed transparent lateral boundaries (Figure 3.1b). The current stayed within the channel as in the classical lock-exchange experiment, but received a constant flux of buoyant fluid.

For visualization purposes, the freshwater was dyed with colored food dye and detailed plume depth field was measured using the optical thickness method (OTM) (Cenedese and Dalziel, 1998; Yuan et al., 2011). The food dye was added in the source water and illuminated by a point light source located above the plume basin. A sequence of images was acquired with a digital camera mounted perpendicular to the water surface. Freshwater thickness fields were calibrated before each experiment using a wedge-shape cuvette. This technique measures the freshwater depth rather than the real plume thickness (Yuan et al., 2011). These experiments, which we will refer to as the plan-view experiments (Figure 3.1c) provided comprehensive imaging of the entire plume structure.

We investigated the detailed interfacial dynamics and mixing processes in the plume (Figure 3.1d) using a combined particle image velocimetry (PIV) and planar laser induced fluorescence (PLIF) technique developed by Cowen et al. (2001). A description of this method and its implementation for stratified flows using a similar set-up are given by Horner-Devine (2006). This technique measures velocity and density fields at short time intervals from a sequence of image triplets taken with a digital

camera fitted with a wavelength cut-off filter. It requires laser sheets from both YAG and Argon ion lasers located beside the plume basin. The laser beams are directed horizontally beneath the plume basin and steered vertically through a cylindrical lens to produce vertical laser sheets that are located on the plume axis and are carefully aligned in the streamwise direction. A 1024 by 1024 pixel CCD camera is positioned 1 m from the plume centerline, and provides images in the vertical streamwise plane of the plume with a 12 cm by 14 cm field of view. The velocity field is obtained from the first two images within one triplet sequence. These images are illuminated by the YAG laser, which has a wavelength higher than the cut-off wavelength so that the light scattered from the particles can pass the filter. The images are processed to generate velocity fields using matPIV (Sveen, 2004). The third image in the sequence is illuminated by the Argon ion laser and processed using the PLIF technique (Crimaldi, 2008). The PLIF concentration images are converted to density using a MicroScale Conductivity and Temperature Instrument (MSCTI) probe located besides the laser field. The probe was mounted to a vertical profiler generated by a step motor and controlled by an Adruino board. The basic experimental parameters are provided in Table 3.1. Each of the spreading experiments was carried out twice to obtain plan-view OTM fields and vertical slice PIV-PLIF fields, while the channelized experiments were only conducted for the PIV-PLIF measurement. The inflow conditions for each experiment were characterized in terms of the inflow Froude number, Fr_i.

3.3 Results

3.3.1 General plume description

As described in the previous section, all of the unconfined runs in this study were done twice for plan-view flow visualizations and vertical-view PIV-PLIF analysis,

Table 3.1: The parameters of the experiments.

	g_0'(cm^2/s)	Q_0(gpm)	U_0(cm/s)	Fr_i	Re
SP1	2.11	6	2.52	0.78	7568
SP2	2.01	9	3.78	1.19	11352
SP3	1.80	12	5.05	1.68	15136
SP4	1.74	15	6.31	2.14	18920
SP5	5.05	6	2.52	0.50	7568
SP6	5.28	9	3.88	0.74	11352
SP7	5.40	12	5.05	0.97	15136
SP8	5.64	15	6.31	1.19	18920
CH1	2.13	6	2.52	0.73	7277
CH2	2.35	9	3.78	1.29	12613
CH3	2.22	12	5.05	1.43	14554
CH4	2.34	15	6.31	1.84	18920
CH5	5.38	6	2.52	0.49	7568
CH6	5.20	9	3.78	0.79	11825
CH7	4.97	12	5.05	1.01	15136
CH8	5.02	15	6.31	1.26	18920

while only vertical-view experiments were conducted for the confined runs. This is because the current propagation in confined runs has been intensively studied in the literature and the plume was too thick to use the optical thickness method in the plan-view experiments. The development of a freely spreading gravity current is shown in the first row of Figures 3.2 (a-c) and 3.3 (a-c), presenting freshwater thickness field snapshots of the flow. Corresponding vertical density fields overlain with simultaneous velocity profiles from the vertical PIV-PLIF measurement are shown below the plan-view images (Figures 3.2d-f and 3.3d-f). To study effects of the lateral spreading, vertical density fields and velocity profiles for confined cases at the same conditions are plotted in the third row in Figures 3.2 (g-i) and 3.3 (g-i) at the same time.

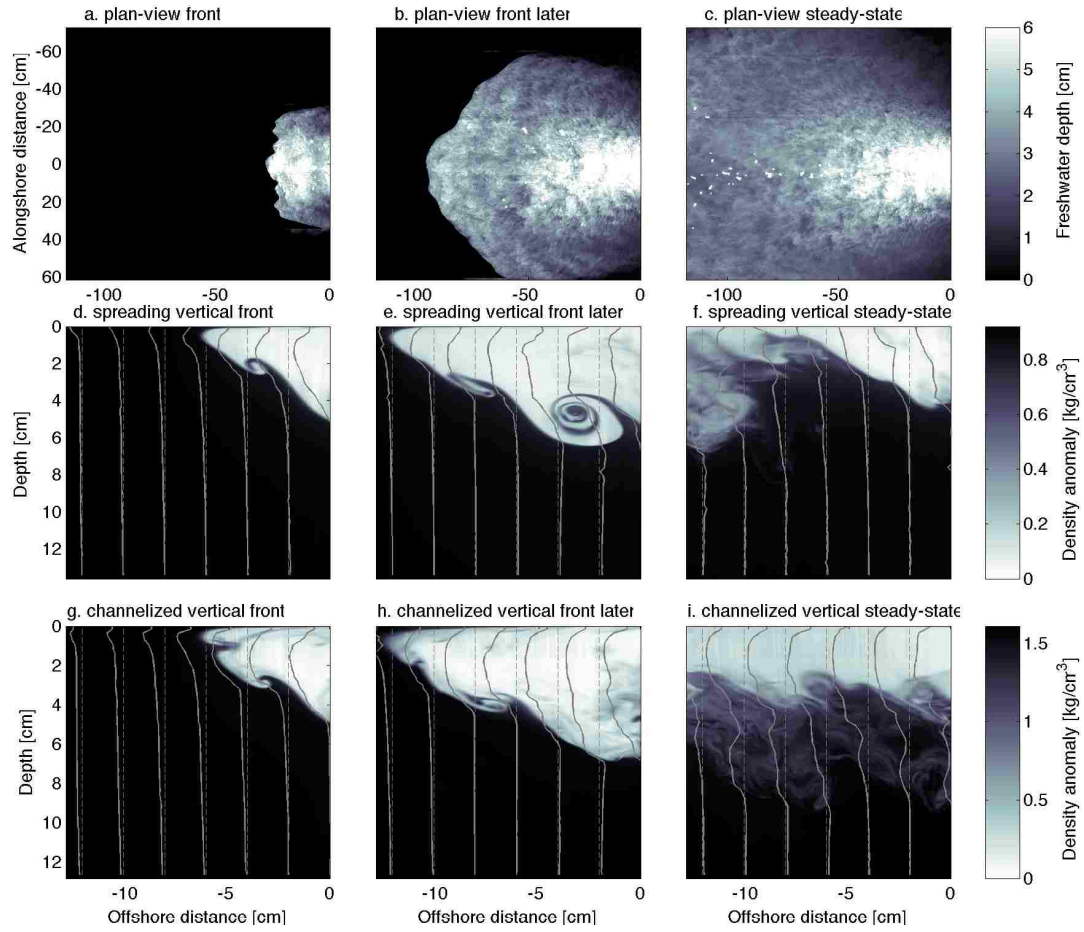

Figure 3.2: High Fr_i spreading (SP3) and channelized (CH3) runs. Spreading runs plan-view freshwater thickness field (a-c), spreading runs x-z slice density field with superimposed horizontal velocity profiles normalized by frontal speed (d-f), and channelized runs x-z slice density field with superimposed horizontal velocity profiles normalized by frontal speed (g-i).

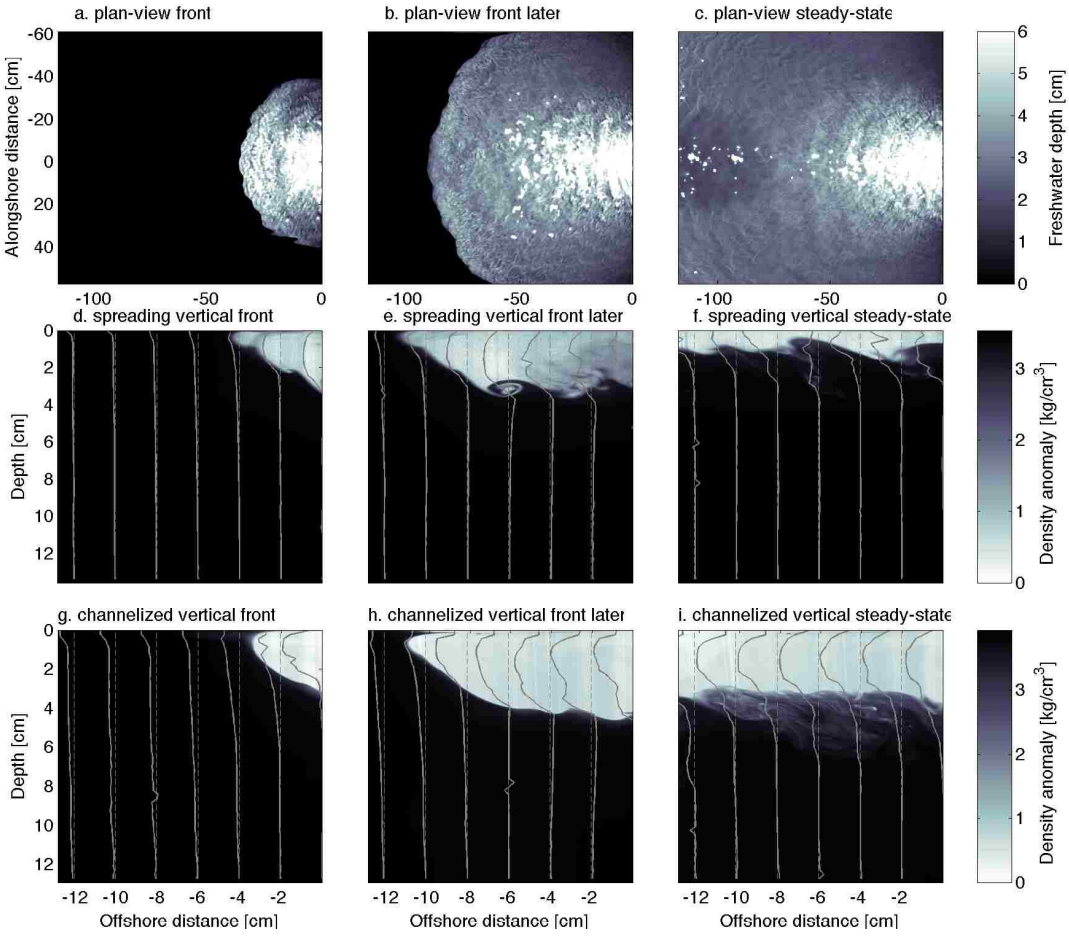

Figure 3.3: Same as Figure 3.2 but for low Fr_i runs (SP5 and CH5)

In the unconfined case the inflowing buoyant water is observed to spread laterally and form a cone-shaped surface layer. The structure and evolution of this surface layer depends on the inflow Froude number. In the high inflow Froude number run ($Fr_i = 1.68$), the flow is supercritical and the plume is a jet-like current with an offshore velocity much higher than the cross-stream velocity (Figure 3.2a-c). In the low inflow Froude number case ($Fr_i = 0.74$) the flow is subcritical and the plume shape is semi-circular (Figure 3.3a-c).

There are several points worth noting regarding lateral spreading. First, although the plume shoals significantly in unconfined cases, the frontal bore has a thickness similar to the confined case. This is because the frontal bore entrains the fluid behind it, leaving a relatively thin trailing layer. The frontal bore in the freshwater thickness field appears as a bright (deep) ring with a darker ring inside of it indicating a band of reduced layer thickness (Figures 3.2a-b and 3.3a-b). This structure can also be found in the vertical density field: an approximately 6 cm deep frontal bore is followed by less than 2 cm layer (not shown in the figure). In the confined case, although the frontal bore is also approximately 6 cm thick, the trailing current has almost the same thickness as the front. This phenomenon is consistent with the previous laboratory study (Patterson et al., 2006) and numerical simulation (Cantero et al., 2007a) on cylindrical spreading gravity currents.

In the unconfined cases the density field show a clear shear-induced vortex billow in the front bore (Figures 3.2e and 3.3e). Unlike the Kelvin-Helmholtz instabilities at the interface between two fluids, the length scale of this vortex is almost half of the plume thickness. There is a sharp interface on the front side of the bore and mixing is energetic on the trailing edge where the plume layer is thin. By contrasts, mixing in the confined current happens within a fairly uniform mixing layer at the interface (Figures 3.2h and 3.3h). There is neither a sharp interface region nor a highly energetic mixing region as seen in the unconfined case.

This wave-like structure persists throughout unconfined runs; it is observed in the plan-view depth field as deep bands near the river mouth (Figures 3.2c and 3.3c) and in the vertical density fields as plume thickness variations (Figures 3.2f and 3.3f). In the confined case, the plume thickness remains constant with a uniform mixing layer at the interface between the plume layer and the ambient fluid (Figures 3.2i and 3.3i).

Velocity profiles normalized by the maximum offshore velocity and superimposed onto the density fields clearly show that fluid in the plume body approaches the front with a velocity higher than that of the frontal bore (Figures 3.2e, h and 3.3e, h). This result is in agreement with earlier numerical simulations (Hartel et al., 2000) and laboratory observations (Thomas et al., 2003) of a two-dimensional gravity current, which find that velocities just behind the gravity current head were typically 20% higher than the frontal velocity. The axisymmetric gravity current was reported to have velocities in the tail up to 40% of that of the front (Patterson et al., 2006). This velocity difference between plume body and front was observed more clearly in the supercritical inflow run (Figure 3.2) than the subcritical inflow run (Figure 3.3).

3.3.2 Plume depth

After sufficient time the plume is considered to be in a steady state because the fluids entering into the basin from the estuary and leaving the basin from the weir are balanced. This steady state has been confirmed from sensitivity tests performed prior to the plan-view experiments. The mean plume freshwater thickness, which is based on an average over 100 seconds (500 images), is highest near the plume center and decreases both in the offshore and in the cross-stream direction (Figure 3.4a). The depth contours in high Fr_i run are half ellipses with major semi-axes located at the plume center. Depth contours in the low Fr_i run are almost semi-circles (not shown).

A centered non-normalized Gaussian fit was successful in describing the lateral distribution of plume freshwater thickness at each plume axis location in every case. Plume freshwater thickness at three plume axis locations (light gray, gray and black indicated in depth field) is plotted in figure 3.4b. The Gaussian fits show an offshore

decrease in plume freshwater thickness and a corresponding increase in width. Plume width is defined to be proportional to the variance of the Gaussian fit $b = C\sigma$, with an unknown coefficient C and in the present experiment we assume $C = 4$. Plume freshwater thickness decreases exponentially (Figure 3.4c), while the estimated plume width increases exponentially with offshore distance (Figure 3.4d).

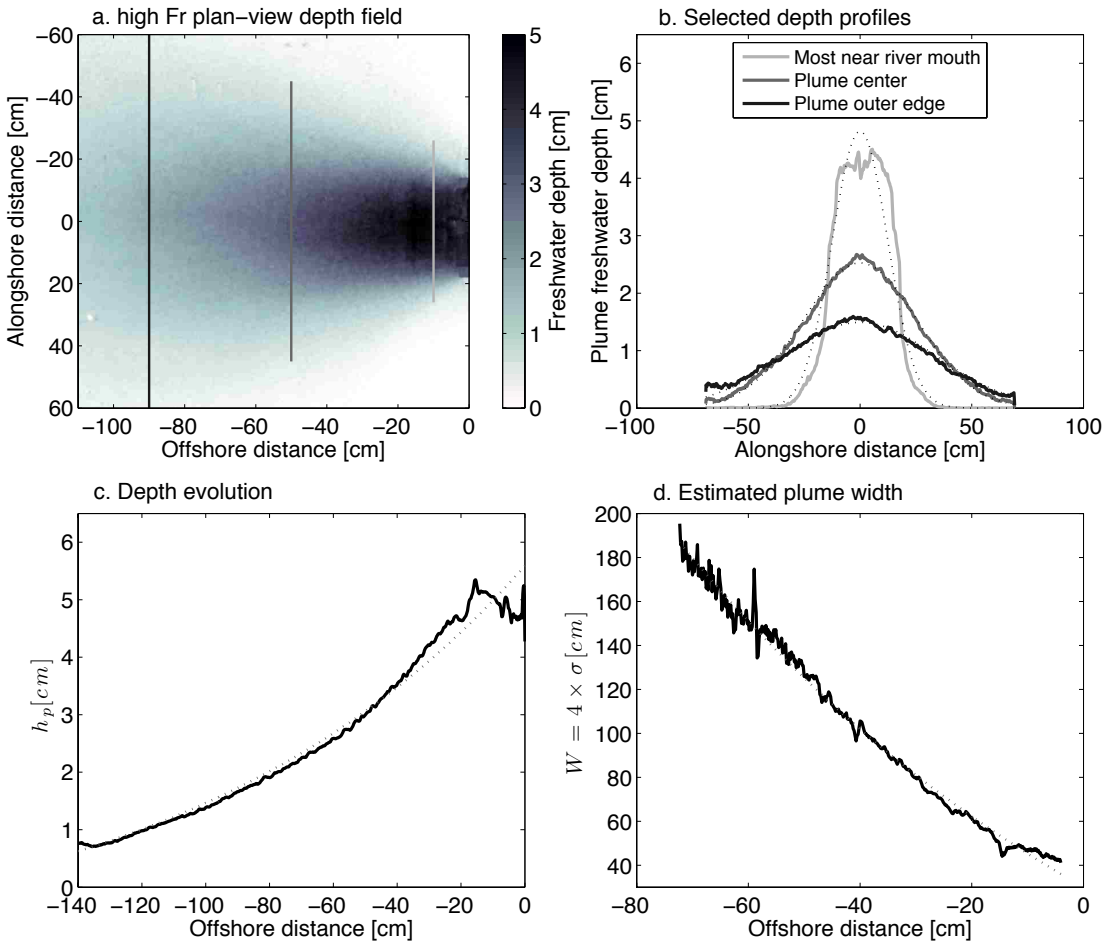

Figure 3.4: a) Plan-view depth field, b) depth profiles at three locations (dash lines are the Gaussian fit to each profiles), c) plume axis depth evolution (dash line is the exponential fit to the depth evolution), and d) estimated plume width based on Gaussian fit (dash line is the exponential fit to the plume width) for a high Fr_i spreading run (Figure 3.2 SP5).

3.3.3 Plume width and global spreading rate

Hetland and MacDonald (2008) define the global spreading rate as $\alpha = \frac{\Delta r/r}{\Delta b/b}$, which relates the relative change in width to the relative change in radial distance. They use this parameter to differentiate between divergent plumes ($\alpha < 1$), in which the lateral expansion of the flow is faster than the outward propagation, and convergent plumes ($\alpha > 1$) in which the plume spreads more slowly than it propagates away from the estuary mouth.

For the present data, the plume width grows exponentially with the plume axis, x, which is equivalent to the radial distance, r. We determine the spreading rate by fitting an exponential curve $\sigma = ax^n + c$ to the width (recall that $b = 4 \times \sigma$) profile for every case. A simple derivation shows that the global spreading rate, α, is the reciprocal of the exponent n:

$$\frac{db}{b} = \frac{1}{n}\frac{dx}{x}. \tag{3.2}$$

The spreading rate alpha decreases with increasing Fr_i (Figure 3.5), indicating a shift toward divergent plumes (e.g. Figure 3.2a-c) for higher Fr_i. A divergent plume is more like an energetic jet, which has high offshore flow relative to the lateral spreading. Lower Fr_i has a higher spreading rate α, where the plume is convergent (Figure 3.3a-c). In this case inflow momentum is less important, radial and lateral spreading are balanced, and the depth contours are circular.

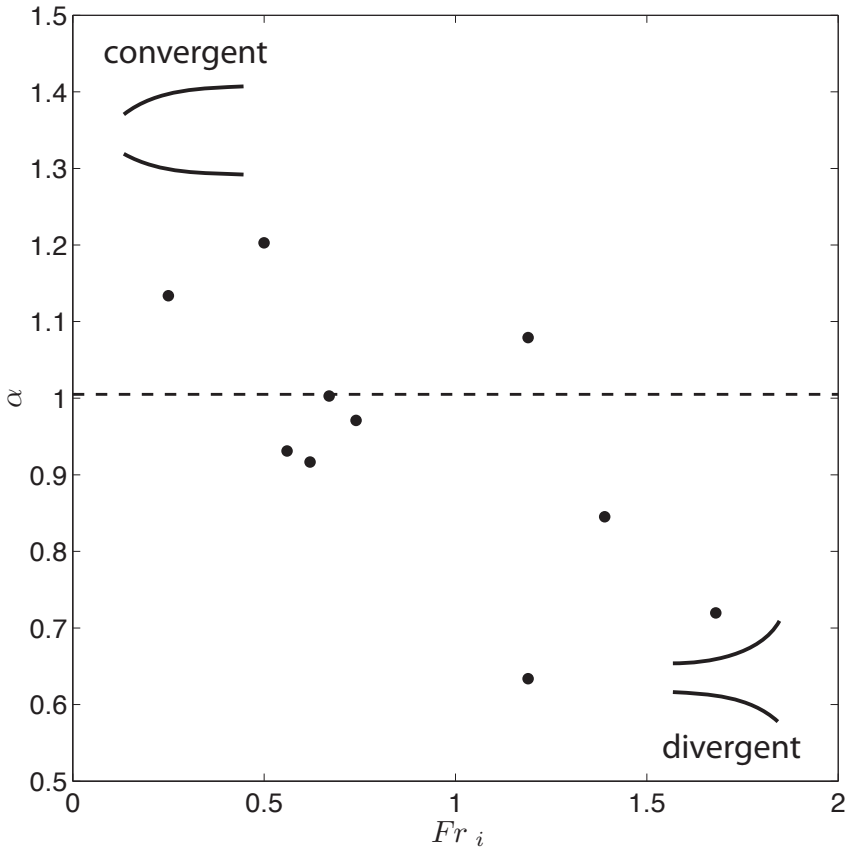

Figure 3.5: Plot of spreading rate α vs. Fr_i. The dash line is $\alpha = 1$, indicating the pure radial spreading $u/\delta = x$. Schematic representations of convergent and divergent plumes, adopted from Hetland and MacDonald (2008), are shown above and below the $\alpha = 1$ line.

3.3.4 Density and velocity profiles

In Figure 3.6 the average plume density and velocity profiles are plotted for all sixteen runs with different inflow Froude numbers. The profiles are averaged in time over the steady state period and in the streamwise direction over the PIV/PLIF field of view. The vertical axis is normalized by the plume thickness, H_p, which is defined as the

depth of the 95% total freshwater flux contour. Here, the freshwater flux is calculated from the density and velocity field using $Q_f(x,z) = \int_z^0 \rho(x,z)u(x,z)dz$.

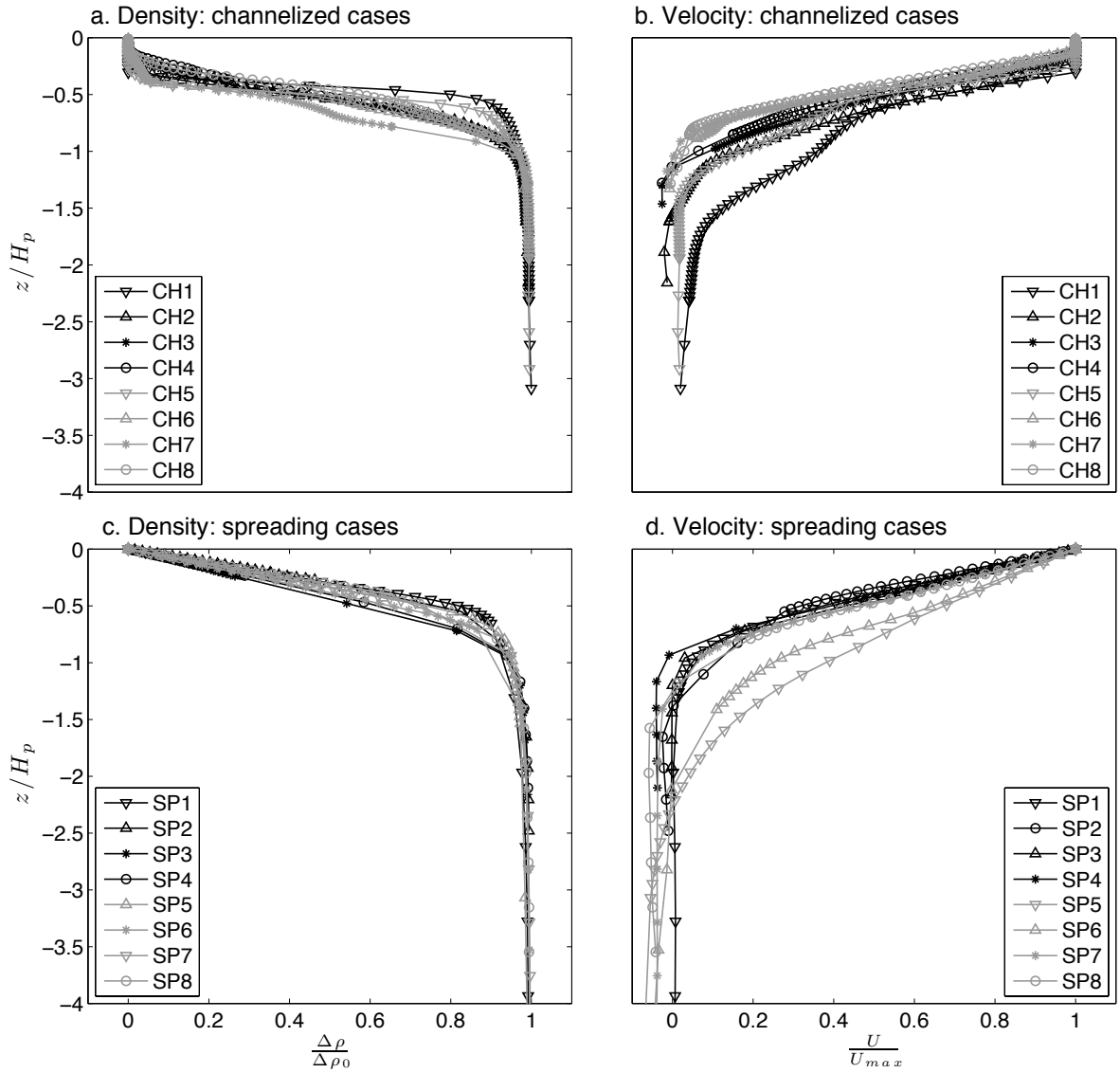

Figure 3.6: Normalized density (a and c) and horizontal velocity (b and d) profiles for channelized (upper) and spreading (lower) runs

Density and the velocity profiles are noticeably different in the channelized and spreading cases. In the channelized case, both density and velocity profiles are step-wise functions with a mixing layer in between the near-surface uniform density layer and underlying quiescent ambient water. This structure is similar to the density and velocity profiles in channelized gravity current laboratory experiments (Britter and Simpson, 1978; Didden and Maxworthy, 1982) and in the two-layer flow in salt-wedge estuary channels (MacDonald and Horner-Devine, 2008; Tedford et al., 2009a). The near-surface uniform density layer disappears in the spreading cases; velocity increases (density decreases) approximately linearly all the way to the water surface. This is consistent with field observation in the ebb tide at Columbia (Kilcher et al., 2012), Fraser (MacDonald and Geyer, 2004), and Merrimack (MacDonald et al., 2007) river plumes.

In spreading and channelized runs, there is good agreement between the normalized density and velocity profiles (Figure 3.6), except runs SP5 and SP6. The co-location of the density gradient and velocity shear is essential for generating K-H instabilities (Thorpe, 1971). Run SP5 and SP6 are both low Fr_i runs, in which the interface thickness for density and velocity profiles are apparently different and there is an offset between the maximum gradient of each profiles. Holmboe instability is possible in stably stratified flows in which the shear interface thickness is larger than the density interface thickness and the inflection points of the two profiles are displaced (Lawrence et al., 1991). Instabilities observed at the interface for run SP6 (Figure 3.3f) have a similar character to the Holmboe instabilities observed in exchange flow laboratory experiments by Tedford et al. (2009b). These low Fr_i instabilities will not be investigated in more detail here, except to note that they may indicate that the plume is in a slightly different mixing regime for these two runs.

3.3.5 Plume density

The average density of the plume layer at a point sufficiently far from the river mouth determines the buoyancy available to drive far field plume processes such as alongshore penetration and freshwater flux, and is related to the net dilution of river-borne matter. The average density at this point is a consequence of the mixing and advection processes in the near-field region. Here we compare the average plume density at the offshore end of our measurement region to see if there is a difference between spreading and channelized plumes. We define the buoyancy anomaly β as:

$$\beta = \frac{\Delta\rho_0}{\Delta\rho} = \frac{\rho_a - \rho_i}{\rho_a - \rho_p}, \tag{3.3}$$

where $\rho_p = \frac{1}{H_p}\int_{-H_p}^{0} \rho(z)dz$ is the plume density averaged vertically over the entire plume layer. The buoyancy anomaly β is the reciprocal of the normalized density anomaly, $\frac{\Delta\rho}{\Delta\rho_0}$, which quantifies the net mixing, or plume dilution, that has occurred between the river mouth and the measurement location (Hetland, 2010). Larger values of β indicate to a higher average plume density at the measurement location, thus more mixing has happened within this region. We observe that β is higher in the spreading cases than the channelized cases (Figure 3.7): the average value of β in the channelized cases is 2.784 ± 0.41, while in the spreading cases is 3.747 ± 0.55. For the spreading cases, higher Fr_i leads to higher β. Note however that the two lowest β in spreading experiments correspond to SP5 and SP6, which were discussed in the previous section. The dependence on Fr_i is lower when these points are excluded. The buoyancy anomaly β shows little dependence on Fr_i in the channelized cases over the parameter range of these experiments.

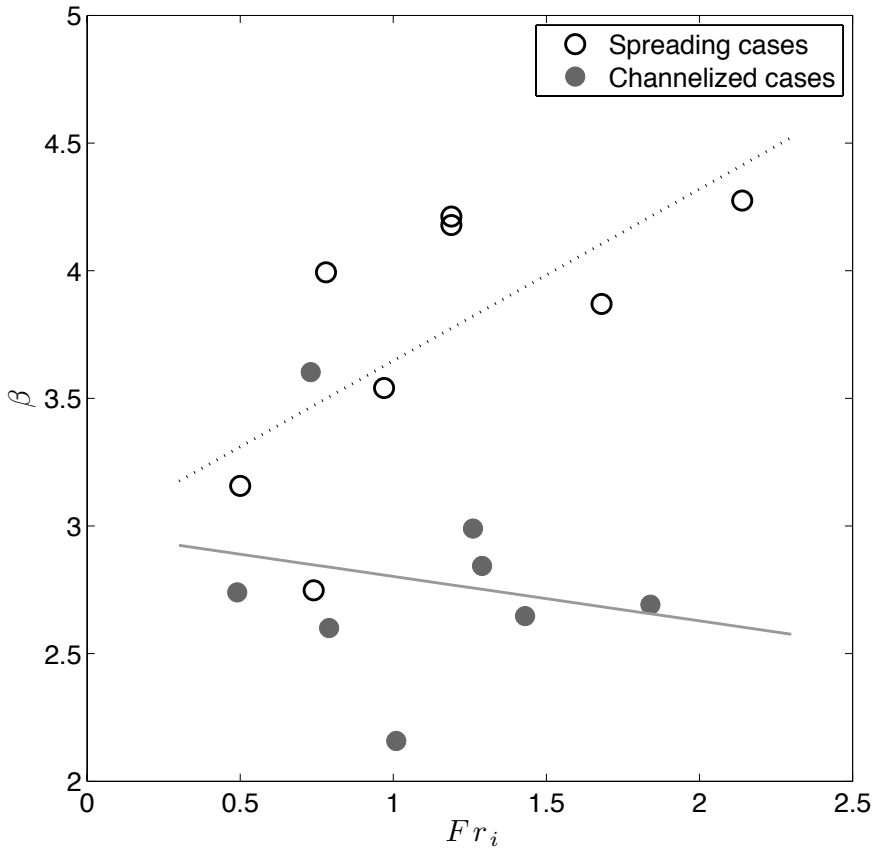

Figure 3.7: Depth averaged plume bouyancy anomaly normalized by inflow density anomaly with different Fr_i for spreading (open circles) and channelized (filled circles) runs. Dash line and solid line are the linear fits to the spreading and channelized runs, respectively.

We expect, however, that buoyant anomaly in the channelized runs is strongly influenced by the near-surface uniform density layer, which is not actively mixing due to the lack of density gradient. Thus, the difference in β between the spreading and channelized runs may be attributed to the disappearance of this surface layer in the spreading cases, rather than differences in the intensity of mixing processes at

the interface. In order to test this we limit the averaging in ρ_p to include only the mixing layer. The plume buoyancy anomaly with only the mixing layer β_{ML} is the same in the spreading (3.747 ± 0.55) and channelized (3.735 ± 0.92) runs, within the experimental errors. Thus, the modification of the density in the mixing layers is the same in both cases, suggesting that the intensity of mixing is the same. This result suggests that the differences observed in the buoyancy anomaly β (Figure 3.7), must be due to advection processes rather than mixing. Differences in entrainment and buoyancy flux will be examined in more detail in sections 3.3.6 and 3.3.7.

Based on a simple theoretical model Hetland (2010) predicts that the buoyant anomaly at the end of near-field plume is a function of $w_e W_0^2/Q_f$, where w_e is the entrainment velocity, and W_0 and Q_f are the inflow width and freshwater flowrate, respectively. The field of view in our experiment is close to the end of the near-field region, though it is likely to be somewhat inside the near-field due to constraints in the experimental set-up. The density anomaly at this point may provide insight into how $\Delta\rho$ changes with inflow conditions and lateral boundary conditions. In the Hetland (2010) model increasing freshwater inflow results in a decreasing density anomaly at the end of near field region. The decrease in the density anomaly, which appears as a decrease in β, with Fr_i observed in the spreading cases (Figure 7) is consistent with this prediction. However, as noted above, no relationship is observed between β and Fr_i in the channelized runs.

3.3.6 Total vertical density flux and entrainment velocity

A direct measurement of the bulk entrainment into the freshwater plume is obtained by calculating the total vertical density flux through the plume base using a control volume approach (MacDonald and Geyer, 2004). This technique has been success-

fully applied for measuring buoyancy, momentum and sediment fluxes in the Marrimack (MacDonald et al., 2007) and Columbia (Kilcher et al., 2012; Nowacki et al., 2012). MacDonald et al. (2007) confirm that the control volume results have an excellent agreement with the Regional Ocean Modeling system (ROMS) numerical model output, and are consistent with direct measurement of turbulent dissipation by autonomous underwater vehicle (AUV) microstructure. In our control volume formulation, lateral flux is constrained using a plume width function, b, which is confirmed using the plan-view experiments. The entrainment velocity w_e and vertical density flux $Q_v = \frac{g}{\rho_0}\overline{\rho w}$ are calculated based on conservation of volume and mass within control volume according to,

$$\iint_{CS} \vec{U} \cdot d\vec{A} = \frac{\partial}{\partial t}\left[\iiint_{CV} dV\right]; \tag{3.4}$$

$$\iint_{CS} \rho\vec{U} \cdot d\vec{A} = \frac{\partial}{\partial t}\left[\iiint_{CV} \rho dV\right]. \tag{3.5}$$

By assuming steady state conditions, the right hand side of both equations reduces to zero. With the assumption that there is no flux through the water surface and lateral boundaries, we find that the flux through the lower boundary equals the difference between outflow and inflow horizontal volume and mass fluxes:

$$\frac{\partial}{\partial x}\left[\int_{-h}^{0} budz\right] - \overline{w}b = 0; \tag{3.6}$$

$$\frac{\partial}{\partial x}\left[\int_{-h}^{0} \rho budz\right] - \overline{\rho w}b = 0; \tag{3.7}$$

The lower boundaries were selected to be the isohalines within the plume layer. This choice provides enhanced resolution of salt flux near the plume base, where there is strong stratification (MacDonald and Geyer, 2004). In this case, the entrainment velocity w_e is actually the diahaline velocity across selected isohalines. Profiles of w_e show that it is negative at the surface and positive below the plume base (Figure 3.8a, c). This is consistent with the entrainment velocity profile from the Fraser River plume lift-off (MacDonald and Geyer, 2004), indicating a developing mixing layer that is entraining fluid from both the surface and deep water.

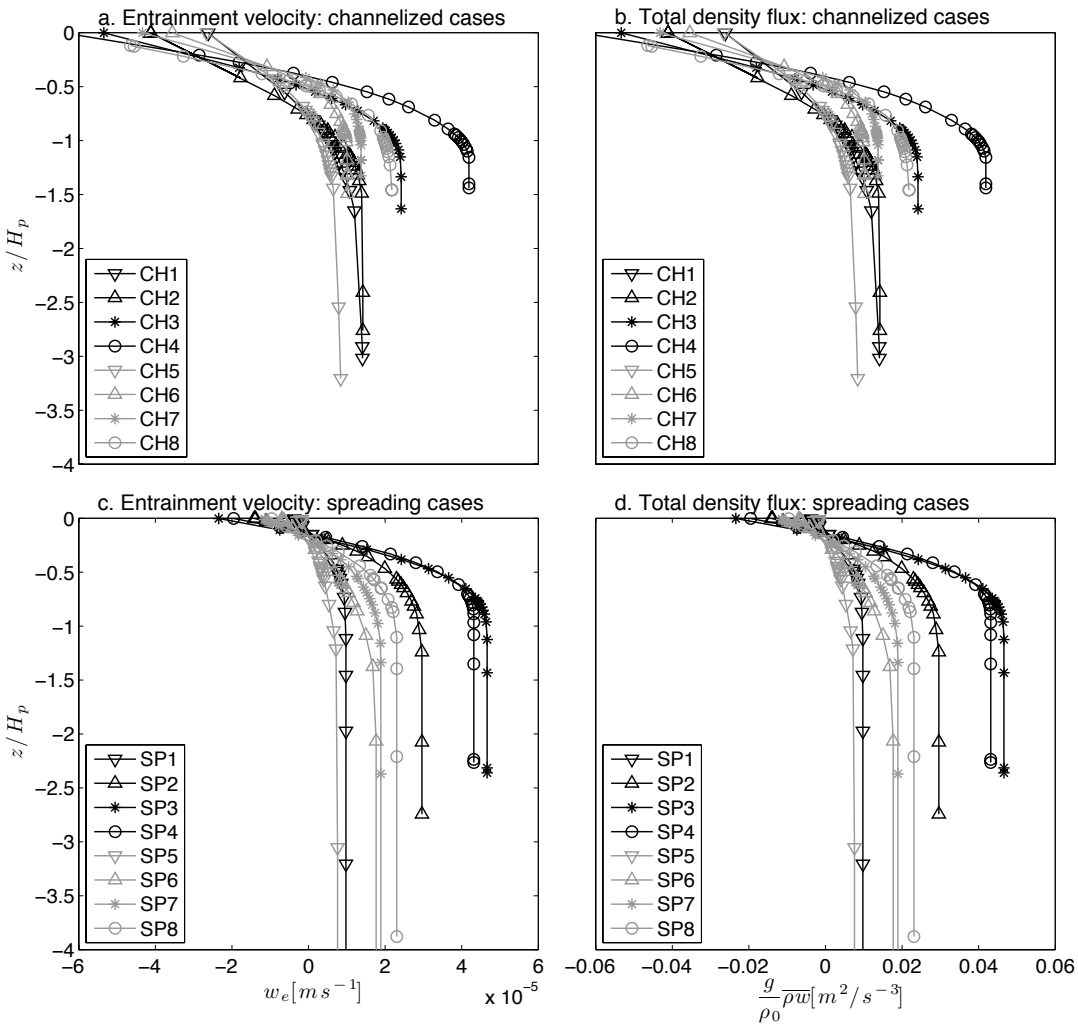

Figure 3.8: Plume entrainment velocity w_e (a and c) and total vertical density flux (b and d) for channelized and spreading experiments.

Channelized and spreading cases both show similar trends in total vertical density fluxes and entrainment velocities (Figure 3.8). Note that in the channelized cases the maximum positive and the maximum negative entrainment velocity are almost the same, while in the spreading cases the maximum positive entrainment velocity from

below is larger than the maximum negative entrainment velocity at the surface. This is because there is a distinct, uniform upper layer in the channelized case from which the buoyant fluid can be entrained down to the mixing layer. In the spreading case, however, there is no such freshwater source at the surface so the entrainment into the mixing layer from above (negative w_e) is smaller than from below (positive w_e).

The entrainment rate is defined as $E = w_e/U$, where U is the layer-averaged velocity in the plume. Morton et al. (1956) first developed the idea of an entrainment rate to quantify the flow of ambient fluid into the turbulent layer. Ellison and Turner (1959) carried out surface jet experiments in a long, narrow, rectangular channel, similar to our channelized configurations. They calculated E based on conservation of volume and related it to the local bulk Richardson number Ri_b. They concluded that E decays exponentially according to Ri_b^{γ} and that entrainment becomes negligible for $Ri_b > 0.8$ in the surface jet. Christodoulou (1986) summarized all available experimental results for a variety of flow types and proposed governing laws for the dependence of the E on Ri_b. He finds that $\gamma \approx -1/2$ at small Ri_b and progressively increases to $-3/2$ for large Ri_b in buoyant overflows.

The entrainment rate E from the present experiments are plotted against bulk Richardson number in Figure 3.9a, along with those of Ellison and Turner (1959); Chu and Vanvari (1976); Pedersen (1980); Buch (1980), as summarized by Christodoulou (1986). Our data are in the small Ri_b regime and are in good agreement with the result from Ellison and Turner (1959) at similar Ri_b range. Two low Fr_i runs have a low entrainment rate with a low Ri_b (diamonds in Figure 3.9a inset), which may be in a different regime than the other runs as described previously. Excluding those two points, data from the present experiments fit the $Ri_b^{-1/2}$ in the region of $Ri_b < O(1)$. This Ri_b region is described by Christodoulou (1986) as the region where the mixing

takes place through vortex entrainment.

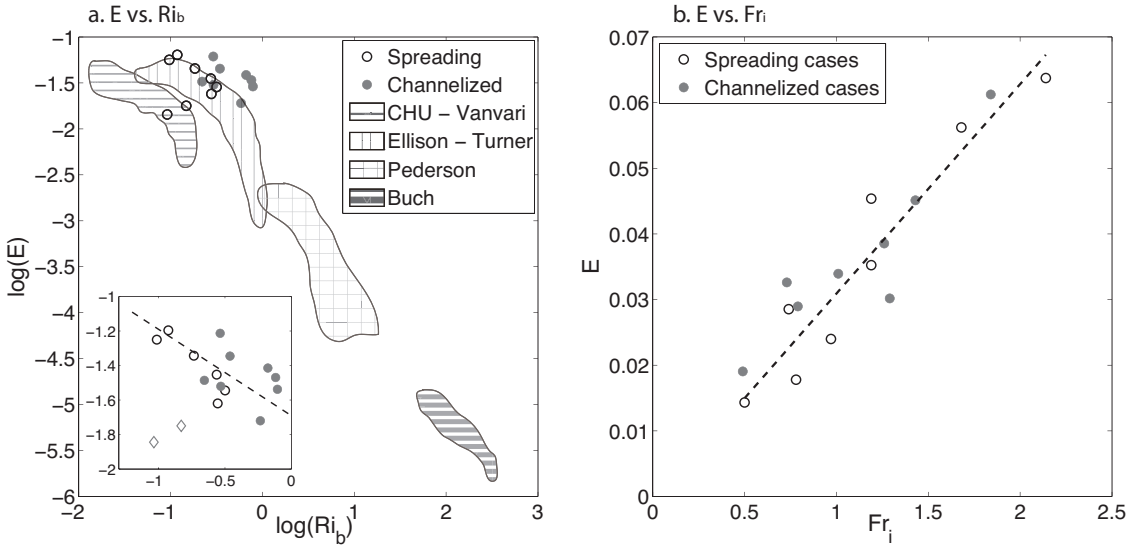

Figure 3.9: a) Plot of entrainment rate (E) vs. bulk Richardson number (Ri_b). Data represented by the shaded regions are drawn from reviews by Christodoulou (1986) with the data from laboratory experiments by Chu and Vanvari (1976); Ellison and Turner (1959); Pedersen (1980) and field observation by Buch (1980). The insert of (a) is the zoom-in of data from present experiments. The dash line is the fit to $E = aRib^{-1/2}$ law to all data as suggested by Christodoulou (1986) (excluding two low Fr_i runs (diamonds) in spreading cases). b) Plot of entrainment rate (E) vs. inflow Froude number (Fr_i) for spreading and channelized cases.

It is also valuable to investigate the dependence of E on Fr_i, which is an independent parameter describing the strength of the inflow as opposed to Ri_b which characterizes the sheared flow observed in situ. We observe a clear linear relationship between E and Fr_i for all experiments (Figure 3.9b). The data shows no significant difference between spreading and channelized cases, suggesting again that local mixing is not modified by lateral spreading. Entrainment parameterizations based on the bulk Richardson number such as Ellison and Turner (1959) require a priori

knowledge of the current properties, which makes the analytical theory complex or even unsolvable (Hetland, 2010). Simpler parameterizations, such as E = constant or w_e = constant have also been commonly used in numerical modeling, but do not capture the dependence of mixing on inflow conditions. Our result indicates a simple relation between the entrainment rate and inflow Froude number, $E = aFr_i + b$.

3.3.7 Turbulent buoyancy flux

The turbulent buoyancy flux is a direct measure of mixing due to turbulence that can be estimated from the available data using the control volume method (MacDonald and Geyer, 2004). It is defined as:

$$B = \frac{g}{\rho_0}\overline{\rho' w'} = \frac{g}{\rho_0}\left(\overline{\rho w} - \bar{\rho}\bar{w}\right). \tag{3.8}$$

where $\frac{g}{\rho_0}\overline{\rho w}$, $\frac{g}{\rho_0}\bar{\rho}\bar{w}$ are the total and mean vertical density fluxes through isohalines, respectively. Here the mean vertical velocity on the bottom bounding isohaleine $\bar{w}$ is taken to be the same as the entrainment velocity w_e. The mean flux is the same order of magnitude as the total and the turbulent buoyancy flux is approximately two orders of magnitude smaller. In all cases, shapes of the turbulent buoyancy flux profiles are relatively similar (Figure 3.10). The peak buoyancy flux occurs approximately one quarter of the plume depth below the surface in spreading cases and slightly lower than half the depth in channelized cases. All profiles decrease to zero at the ambient water interface, and are forced to be zero at the water surface. This profile shape is consistent with field observations from the Fraser (MacDonald and Geyer, 2004) and Merrimack (MacDonald et al., 2007) river plumes. The buoyancy flux profiles generally have a higher peak in the channelized cases than in the spreading cases, especially for the high flowrate runs (stars and open circles in Figure 3.10a). In the

channelized cases the turbulent buoyancy flux decreases to zero right at the plume base $z/H_p = -1$), while in the spreading cases it decreases to zero around $z/H_p = -0.8$.

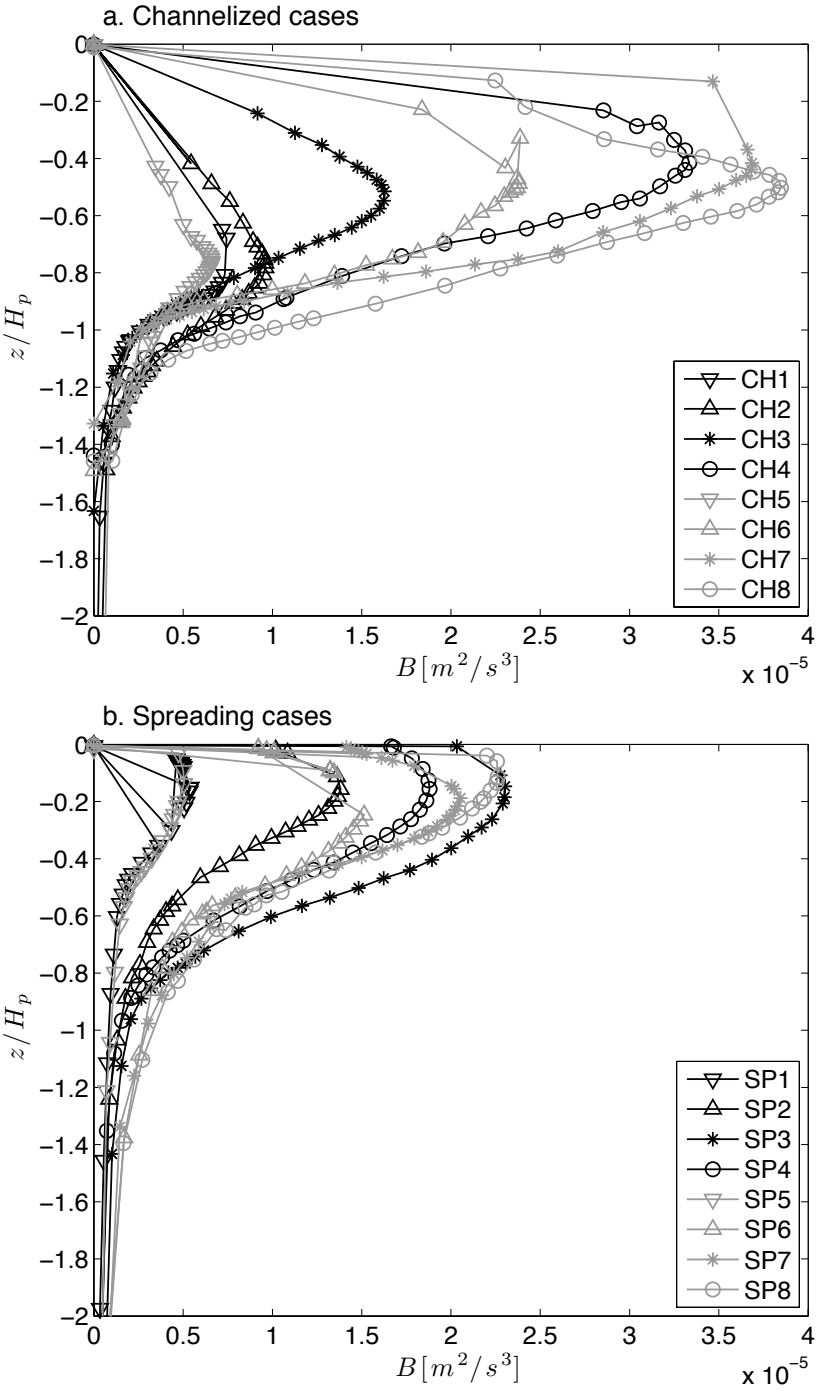

Figure 3.10: Turbulent buoyancy flux between inflow and at the end of field of view for a) channelized and b) spreading runs

The depth averaged buoyancy flux over the plume layer is defined as:

$$\bar{B} = \frac{1}{H_p} \int_{-H_p}^{0} B(z) dz. \tag{3.9}$$

The average flux is then normalized to form the mixing parameter $\xi = \frac{\bar{B}}{\Delta u g'}$, (MacDonald and Geyer, 2004; MacDonald and Chen, 2012), , where Δu is the velocity difference between upper and lower layers. In our case $\Delta u = u_p$, because there is no velocity in the ambient water. Because the shapes of the profiles are similar, the relationship between B values in different experiments is similar if we use the maximum flux $B_{\max}$ instead of the depth average value. The value of ξ increases with Fr_i as expected (Figure 3.11a). Most importantly, however, there is no difference between the values of ξ in spreading and channelized cases (Figure 3.11a). The average value of ξ is $(1.04 \pm 0.69) \times 10^{-4}$ in the spreading cases and $(1.38 \pm 1.01) \times 10^{-4}$ in the channelized cases. This somewhat surprising result is evidence that local turbulent mixing processes are unaffected by plume spreading.

One significant difference between spreading and channelized cases is that the plume horizontal surface area is much higher in spreading cases (Figure 3.4a). When lateral spreading thins the plume, the horizontal interfacial area occupied by the mixing layer increases from a channelized rectangle to a cone-shaped area. The plume area is an order of magnitude larger in the spreading cases than in the channelized cases (Figure 3.11b). To account for the total mixing, we define the area-integrated turbulent buoyancy flux $\xi_A = \xi \frac{A_S}{A_C}$, where A_S and A_C are the horizontal surface area in a given spreading run and the corresponding channelized run with the same inflow conditions, respectively. The area-integrated turbulent buoyancy flux in the spreading runs is almost ten times larger than the channelized cases (Figure 3.11c). The average value of ξ_A is $(4.43 \pm 3.30) \times 10^{-4}$ in the spreading cases and $(1.44 \pm 1.16) \times 10^{-4}$

in the channelized cases. Thus spreading dramatically increases the total turbulent mixing, even though it doesnt appear to change the local mixing processes.

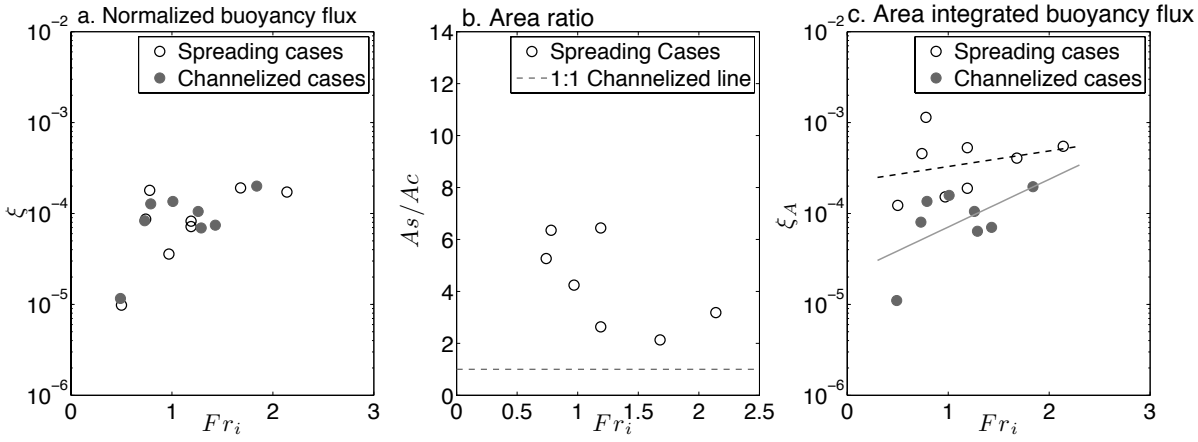

Figure 3.11: Plots of a) normalized buoyancy flux $\xi = \frac{\bar{B}}{\Delta u g'}$, b) ratio of Plume area in spreading cases (A_S) to channelized cases (A_C), and c) area integrated turbulent buoyancy flux $\xi_A = \xi \frac{A_S}{A_C}$ vs. Fr_i for spreading (open circles) and channelized (filled circles) runs. Linear fits in c) are applied separately for spreading (dash line) and for channelized runs (solid line).

The area integrated turbulent buoyancy flux appears to be less sensitive to Fr_i in spreading cases than in channelized cases (Figure 3.11c), although this difference is admittedly driven by a couple of the low Fr_i runs. This difference in dependence may be because the low Fr_i case has a higher spreading rate (Figure 3.5), thus a wider plume and a larger interfacial surface area. So the increased plume width compensates when Fr_i is low.

3.4 Discussion

The results from the present experiments support the conclusion that lateral spreading significantly modifies the plumes vertical structure (Figure 3.6) and the plume density

anomaly (Figure 3.7). However, these experiments do not support the hypothesis that lateral spreading increases the local mixing, as quantified by the entrainment rate (Figure 3.9b) and the turbulent buoyancy flux (Figure 3.11a). We observed increased mixing in the spreading cases compared with the channelized experiments (Figure 3.11c), but this is shown to be the result of the increased interfacial surface area of the spreading plumes (Figure 3.11b), rather than any impact of spreading on the local mixing processes.

The results of the present experiments motivate the following question: why doesn't lateral spreading impact turbulent mixing in the plume, even when it significantly modifies the vertical plume structure? We investigate two possible mechanisms that may explain this result in section 3.4.2.

3.4.1 Applicability of the laboratory experiments to river plumes

Here we use three important non-dimensional parameters for comparing the turbulent mixing in the laboratory, field and numerical methods:

$$I = \frac{\varepsilon}{\nu N^2}; \qquad \eta = \frac{L_o}{H_p}; \qquad \xi = \frac{\bar{B}}{\Delta u g'}; \tag{3.10}$$

The first parameter, I, commonly referred to as the buoyancy Reynolds number, can be interpreted as the ratio of the destabilizing effects of turbulent stirring to the stabilizing effects resulting from the combined action of buoyancy and viscosity (Ivey et al., 2008). When I is above a threshold value of $20 - 30$ the turbulence in the stratified fluid can be maintained (Stillinger et al., 1983). Shih et al. (2005) suggest three discernible regimes of turbulent flow based on their DNS results: a diffusive regime where $I < 7$; an intermediate regime where $7 < I < 100$; and an energetic regime where $I > 100$.

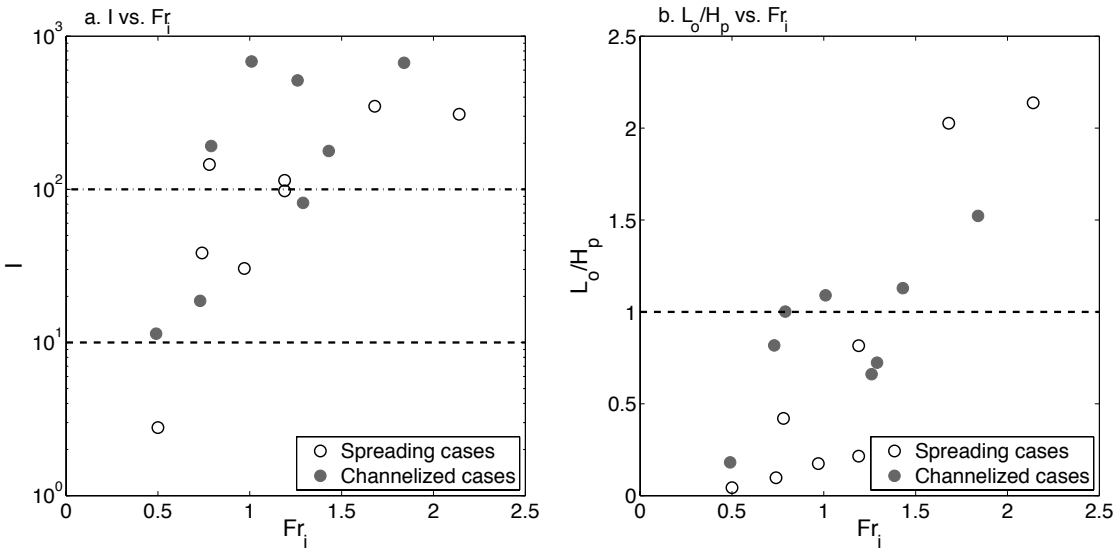

Figure 3.12: Plots of a) $I = \varepsilon/\nu N^2$ vs. Fr_i, dash line and dash-dot lines are two thresholds for turbulent regime, $I = 10$ and $I = 100$.b) Ozmidov scale L_o normalized by plume thickness H_p vs. Fr_i, dash line is the reference for $L_o = H_p$

The turbulent kinetic energy dissipation rate ε could not be measured directly in our experiments. In order to estimate an approximate value for ε we assume the turbulent field is homogeneous and isotropic and the flux Richardson number $Ri_f = B/P$ is at its maximum value 0.2. This assumption is valid in stratified shear flow, when the Kelvin-Helmholtz billows are the primary mechanism of turbulence generation (MacDonald and Geyer, 2004). With these assumptions we can estimate ε based on the difference between the production and buoyancy flux, ($\varepsilon = \frac{1}{1-Ri_f}\bar{B}$). The values in our experiments range from 10^{-5} to 10^{-4} m^2/s^3, which are typical of observations in stratified coastal environments (Orton and Jay, 2005; MacDonald et al., 2007) and one order of magnitude smaller than the lift-off zone in Fraser River plume (MacDonald and Geyer, 2004).

The present results for I are plotted in figure 3.12a, with two thresholds delineat-

ing the three regimes indicated by a dashed line ($I = 10$) and dash-dot line ($I = 100$). One of the low Fr_i spreading runs falls in the diffusive regime where the flow is mostly dominated by molecular diffusivity. Most of the data are in the transition or energetic regime in the range of $10 < I < 1000$. They are slightly higher than previous laboratory experiments by Ivey and Imberger (1991) of I between approximately 10 and 100. Geyer et al. (2010) observed secondary instability along the braids of turbulent core in a high Reynolds number estuary for $I = 100 - 500$. We observe similar structure in the high Fr_i run (Figure 3.2e) at $I = 300$. Recent field observations have suggested values of I are on the order of 10^4 to 10^5 in the highly stratified Columbia River estuary during ebb tide (Kay and Jay, 2003) and in the Fraser River plume (MacDonald and Geyer, 2004).

Previous studies have suggested that mixing in gravity driven currents is accomplished through the generation of Kelvin-Helmholtz instabilities as density overturns with scales of similar size to the Ozmidov scale, $Lo = (\varepsilon/N^3)^{1/2}$ (MacDonald and Geyer, 2004). These overturns are clearly seen in the mixing layer of the plume in both cases (Figure 3.2 and 3.3). Thus Ozmidov scale provides an indication of the scales of the turbulent eddies and should be on the similar order of magnitude to the current thickness. An important question for the current experiments is whether the thinness of the plume layer limits the scales of turbulent mixing and, in particular, if this effect could differentially influence the mixing in the thinner spreading plume runs. Figure 3.12b shows estimates of L_o normalized by the plume thickness H_p. For the majority of the experiments Lo is comparable in magnitude but less than the plume thickness H_p. We observe that L_o/H_p increases with Fr_i and that L_o exceeds H_p in a few high Fr_i experiments. This indicates that the plume thickness has the potential to inhibit the turbulence. However, there is no indication that the influ-

ence of the surface is greater in the spreading or channelized experiments. Thus we conclude that the conclusion that depth limitation cannot explain the result that the local mixing processes are unaffected by spreading.

Finally, the mixing parameter $\xi = \frac{\bar{B}}{\Delta u g'}$ represents the efficiency with which energy is extracted from the mean flow and converted into turbulent energy (MacDonald and Geyer, 2004; MacDonald and Chen, 2012). The values of ξ observed in the present experiments are in the range from 10^{-5} to 10^{-3} (Figure 3.11a), the upper end of which are comparable to field observations of approximately 2.6×10^{-4} (MacDonald and Geyer, 2004). The channelized cases can be compared with the experiments of Ellison and Turner (1959), which have a similar geometry. In those previous experiments they obtain an entrainment coefficients on the order of 10^{-2}. MacDonald and Chen (2012) suggest that with some reasonable assumptions, this value can be converted to a comparable value of ξ also on the order of 10^{-2}, which is significantly higher than the results reported here. We note, however, that the present results agree well with the non-spreading limit $\xi_0 = 5 \times 10^{-5}$ described in MacDonald and Chen (2012).

Although the Reynolds numbers of the laboratory-generated plumes (table 3.1) are significantly lower than most plumes observed in the field, the buoyancy Reynolds number I and the mixing parameter ξ are both in the same approximate range, suggesting that the turbulence is sufficiently active to represent the processes observed in the field. Furthermore, we conclude that depth limitation, while it is more significant in the laboratory experiments than the field, does not appear to influence the finding that mixing is unaffected by spreading.

3.4.2 Two possible mechanisms

The results presented in section 3.3.4 describe important differences in the structure of channelized and spreading currents. The buoyant current in the channelized case has a step-wise density and velocity structures, as is commonly observed in the two-layer exchange flow in estuary channels (Figure 3.13a line in the dark gray area). It has a minimum density (maximum velocity) in the near-surface uniform density layer, a maximum density (zero velocity) in the bottom layer and a mixing layer in between in which the density increases and velocity decreases continuously. The thickness of this mixing layer increases as the current propagates offshore because it entrains water from both the upper and lower layers. In the spreading case, however, the near-surface uniform density layer disappears and the vertical plume structure consists of a $1-1/2$ layer system with a mixing layer that extends approximately linearly to the water surface (Figure 3.13a line in the light gray area). This structure is consistent with field observations in near-field river plumes (e.g. MacDonald and Geyer (2004); MacDonald et al. (2007); Kilcher et al. (2012)). Despite the difference in the structure of the spreading and channelized currents, the properties of the mixing layer such as the mixing layer thickness, the density structure and the velocity structure are almost identical in both cases for the same inflow conditions. In addition, mixing properties such as the entrainment velocity and turbulent buoyancy flux are similar in the spreading and channelized cases.

We consider two mechanisms that may explain the unexpected result that local mixing processes are not affected by plume spreading. Both invoke the idea that there is vertical structure to the spreading and mixing processes and that the influence of spreading on mixing will be minimized if the two processes are misaligned spatially. The proposed mechanisms leading to this misalignment are different in the region very

near the river mouth and in the rest of the near-field plume. They are described below and summarized schematically in Figure 3.13. First, in the jet-to-plume transition region immediately offshore of the river mouth where the current transforms from a buoyant jet into a river plume, the spreading occurs primarily in the near-surface uniform density region while most mixing occurs at the plume base. Second, although the spreading and mixing occur within the same layer in the near field region, their structures are offset such that spreading does not significantly impact the region of maximum mixing. Two mechanisms may act independently or together in different regions (Figure 3.13a).

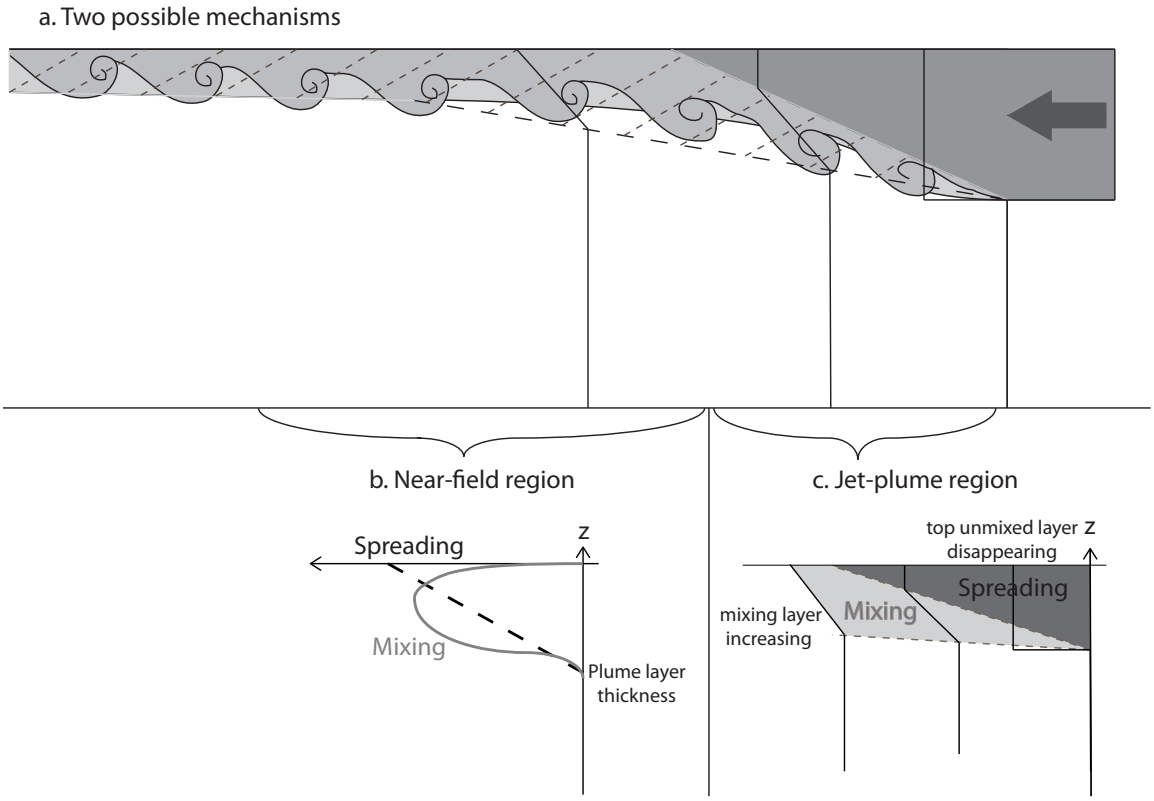

Figure 3.13: Schematic representation of spreading and mixing in the jet-plume and near-field plume regions showing a) transformation of vertical density structure, and the relationship between spreading and mixing in b) the near-field plume and c) the jet-plume region.

Jet-to-Plume region

The near-field region near the river mouth is one of the most energetic regions in the river plume. Total mixing in this region is of the same order of magnitude as it is in the mid-field and far-field plumes, even though the near-field is orders of magnitude smaller in area (Hetland and MacDonald, 2008). In the spreading case, the flow evolves in this region from a channelized current in the estuary into a buoyant river plume. As the current moves offshore, the density and velocity profiles change

dramatically from two-layer step-wise profiles to mixing layer profiles (Figure 3.13a).

Lateral spreading is due to the horizontal pressure gradient between two cross-stream adjacent points. This pressure gradient is highest at the water surface and decreases to zero at the plume base. Our hypothesis is that in this transition region the spreading occurs most in the near-surface uniform density layer (Figure 3.13c dark gray area) while the most energetic mixing region is at the plume base (Figure 3.13c light gray area). Thus, the mixing layer does not spread significantly; instead it rises to the water surface to replace the plume layer lost to lateral advection. The result of the lateral spreading is that the near-surface uniform density layer disappears, as shown in the cartoon of this jet-plume region (Figure 3.13c).

Jirka et al. (1981) describe the jet-plume region as the region where momentum dominates over buoyancy and the impact of the initial channel geometry disappears. They define a jet-plume length scale as $L_M = (Q_0 U_0)^{3/4}/(Q_0 g_0')^{1/2}$. The jet-plume length scale is relatively small compared to the whole plume and is even smaller than the near-field plume scale. In this region the plume behaves much like a buoyant jet, driven by the enhanced velocities of the discharge as it initially enters the coastal region.

In our experiments, the jet-to-plume length scale is 8.77 cm for $g' = 2$ cm/s^2 (3.51 cm for $g' = 5$ cm/s^2). This means that our control volume box from the river mouth to offshore PIV/PLIF field of view ($\approx$ 30 cm), extends well beyond the jet-to-plume region. This is consistent with the observation that the density profiles in the spreading are fully developed mixing layer profiles. We suggest that spreading in this region is due primarily to lateral slumping of the initially uniform density surface layer and that mixing, which is primarily at the base of this layer is unaffected.

Near-field region

Seaward of the jet-to-plume region, the spreading plumes are characterized by linear density and velocity profiles (Figure 3.6a line III). Profiles of vertical buoyancy flux in the spreading cases have maxima at $z \approx -H_p/4$ (Figure 3.10) and decrease to zero both at the surface and at the plume base.

As discussed in the previous section, lateral spreading is due to a cross-stream horizontal pressure gradient. The pressure gradient (dP/dy) is expected to be a linear function of depth within the plume: highest at the water surface and decreasing to zero at the plume base. Although we cannot directly calculate the spreading rate based on the horizontal pressure gradient, it is reasonable to assume the spreading rate should have the same shape as the pressure gradient.

In addition, we can calculate the local lateral spreading rate (dv/dy) along the plume axis directly from the measured velocity field based on the continuity equation:

$$\frac{dv}{dy} = -(\frac{du}{dx} + \frac{dw}{dz}). \tag{3.11}$$

The local lateral spreading profile is calculated by averaging the dv/dy field horizontally and then normalizing it by its maximum value. In Figure 3.14 the normalized spreading rate is plotted against the normalized depth and fitted by an exponential curve to compare with the normalized buoyancy flux profiles. The lateral spreading rate has its maximum value at the water surface and is highest within the top half of the layer before decreasing dramatically in the lower half of plume layer. Meanwhile, the mixing profile has its maximum at $z \approx -H_p/4$ and decreases both upward and downward. The spreading rate at the location of the maximum buoyancy flux is between 20% to 50% of the maximum spreading rate at the surface. Throughout

the lower three-quarters of plume layer lateral spreading is significantly reduced and is not expected to influence mixing. This lower three-quarters of the layer is where the most effective entrainment happens, i.e., entraining dense fluid from the ambient water ($w_e > 0$) in Figure 3.8.

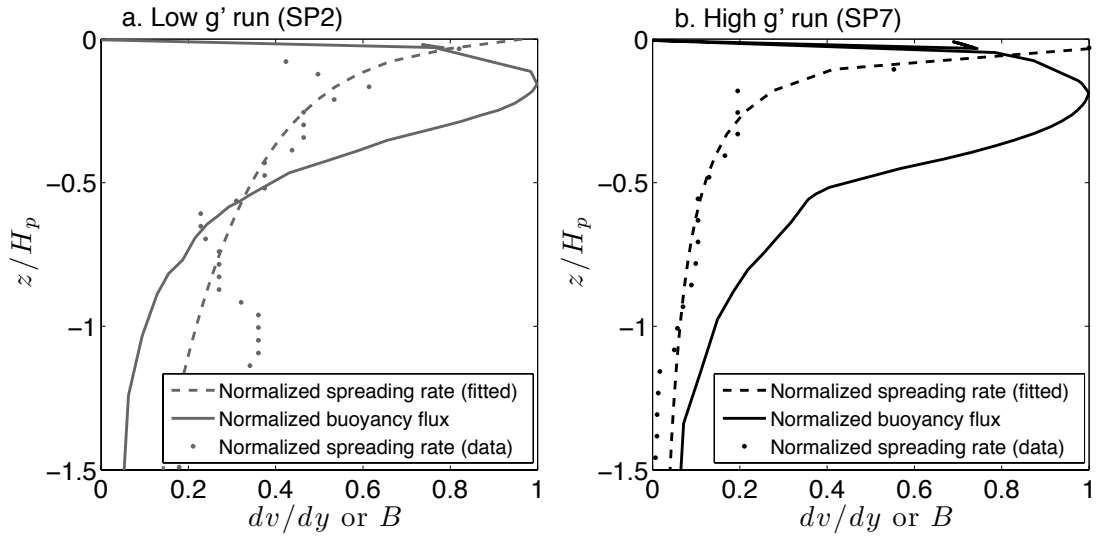

Figure 3.14: Compare normalized spreading rate (dv/dy) profiles (dots) fitted by exponential decay (dash line) to the normalized turbulent buoyancy flux profiles (solid lines) for a) low g' SP2 and b) high g' SP7 run.

This mechanism is similar to mechanism described for the jet-to-plume region; the maxima in the spreading and mixing profiles are not coincident. The spreading at the top unmixed layer and mixing (entrainment) at the plume base with no overlap in the jet-to-plume region is the extreme case of the offset mixing and spreading profiles discussed here (Figure 3.12b).

The lateral spreading rate is commonly known to be related to the local internal gravity wave speed, i.e., $\sqrt{g'h}$ (Wright and Coleman, 1971; Hetland and MacDon-

ald, 2008). In our experiments and in previous studies that use the control volume method, the lateral spreading rate is assumed to be independent of depth (MacDonald and Geyer, 2004; Kilcher et al., 2012). This assumption agrees reasonably well with field data, although authors have hypothesized that observed discrepancies may be attributed to the depth dependence in the spreading. Our analysis supports this hypothesis; suggesting that the vertical structure of lateral spreading rate actually may play an important role in determining the relationship between lateral spreading and its effect on mixing.

3.5 Conclusion

This paper presents a direct comparison between channelized and freely spreading buoyant gravity currents with a continuous freshwater source in laboratory experiments. The configuration of the experiments simulates a coastal river inflow with a simplified geometry in order to better understand the role of lateral spreading on the mixing and dilution of river water as it enters the coastal ocean.

Consistent with predictions from previous work (Wright and Coleman, 1971; Hetland and MacDonald, 2008), we observe that the lateral spreading rate is highly dependent on the inflow condition as characterized by Fr_i: the plume is convergent when $Fr_i < 1$ and divergent when $Fr_i > 1$ (Figure 3.5). As a consequence of these changes to the spreading rate, the increase in plume area due to spreading within a given distance from the river mouth is significantly greater for low Fr_i than high Fr_i plumes (Figure 3.11b).

Lateral spreading dramatically modifies the plume's vertical structure; the spreading plume layer consists of approximately linear density and velocity profiles that extend to the surface, whereas the channelized plumes have regions of uniform den-

sity and velocity near the surface (Figure 3.6). In addition, the average density of the plume layer at a fixed distance from the river mouth is higher in the spreading experiments than in the channelized experiments (Figure 3.7).

We estimate the entrainment rate E and the turbulent buoyancy flux B using the control volume method described by MacDonald and Geyer (2004). The entrainment rate is in good agreement with other laboratory data and fits the $Ri_b^{-1/2}$ law (Ellison and Turner, 1959; Christodoulou, 1986) in the low Ri_b region. A key outcome of this work is the observation that there is no difference between the entrainment rate or buoyancy flux in the channelized and spreading cases. This indicates that lateral spreading does not modify the local mixing efficiency, counter to the expectations outlined in MacDonald and Chen (2012). We hypothesize that this is because the spreading occurs preferentially near the surface, whereas buoyancy flux is greatest in the core of the current.

We conclude that spreading significantly increases the total mixing in the plume (Figure 3.11c). However, the increase in mixing is due to the increase in the area of the plume (Figure 3.11b) as opposed to changes in the local mixing processes associated with spreading (Figure 3.11a). As estuary water enters the coastal ocean, lateral expansion occurs preferentially near the surface, eliminating the uniform density layer observed at the surface in the estuary and shifting the mixing layer upwards to the water surface. Near-surface water is thus redistributed across a much wider area, where it then forms the plume base and is susceptible to mixing. The result of the lateral advection of fresh near-surface water is that the plume layer is more diluted on average in the presence of spreading than an equivalent channelized flow.

Chapter 4

IMPACT OF LATERAL SPREADING ON AN ENERGETIC BUOYANCY DRIVEN CURRENT: THE GENERATION OF NON-LINEAR INTERNAL SOLITARY WAVES WITH TRAPPED CORES

We observe the non-linear internal solitary wave phenomenon in the laterally unconfined energetic gravity current in non-rotating laboratory experiments. The current is visualized based on plan-view imaging using the Optical Thickness Method (OTM), and vertical-view by combining particle image velocimetry (PIV) and planar laser induced fluorescence (PLIF). We observe that large-scale structures are continuously generated at the river mouth and propagates offshore in supercritical spreading cases, whereas in channelized cases the current has classical Kelvin-Helmholtz billows at the interface. We conclude that these large-scale structures are the nonlinear solitary waves with trapped cores, which are generated in the supercritical flow via shoaling of the single moving layer. The freely spreading freshwater outflow into the unbounded heavier ambient water is analogue to the two-layer exchange flow over the topography change, such as the sill and contraction situation. The river mouth acts like the narrowest point in the contraction after which the flow width starts to expand as the current flowing into the unbounded ambient water, while the lateral spreading shoals the current depth vertically. We find that lateral spreading dramatically modifies the plume structure; the channelized plumes have regions of uniform density and velocity near the surface and approximately linear density and velocity profiles at the interface, where as the spreading plume layer consists of this linear density and veloc-

ity profiles extending to the surface. This modification is essential in generating the non-linear internal solitary waves, especially trapped cores within those waves. Our results are consistent with predictions from the two-layer shoaling numerical model: the top uniform density layer greatly inhibits the formation of nonlinear solitary wave with trapped cores.

4.1 Introduction

In this experiment, fluids of different densities initially at rest are separated by a vertical gate in a tank. When the gate is removed, a pump is simultaneously activated and light water is fed into the filling basin at a constant flowrate. Light fluid flows on top of the dense ambient water driven by the baroclinic pressure gradient. This pressure gradient is maintained by a constant inflow source and the flow reaches quasi-steady state by balancing the inflow from the source tank and outflow through the weir. Figure 4.1 shows the configuration for the experiments: a channelized release in which fluids on both sides of the gate are constrained within lateral boundaries is shown in Figure 4.1a and a lateral spreading release in which the width of the dense ambient fluid tank is eight times that of the light fluid filling basin is shown in Figure 4.1b.

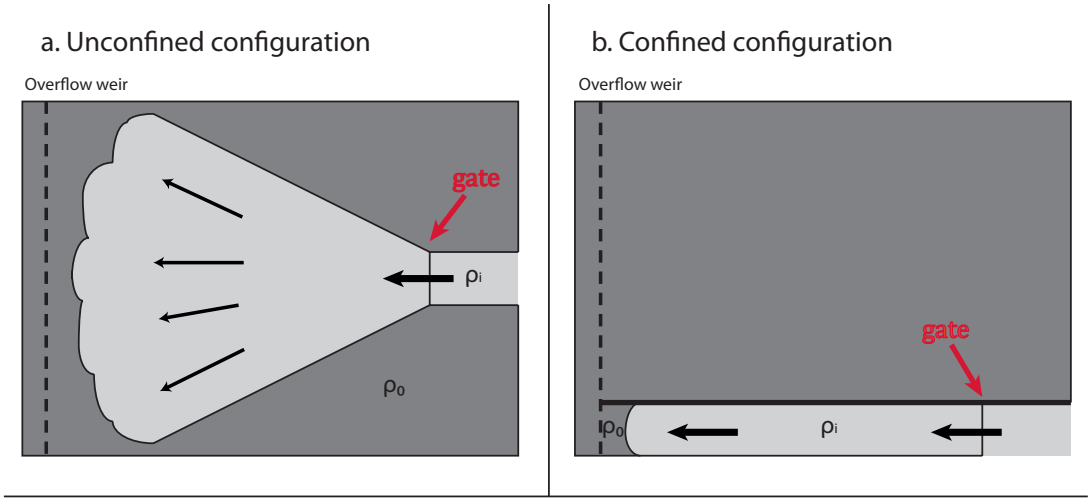

Figure 4.1: Schematic of laterally a) unconfined (spreading) and b) confined (channelized) gravity currents.

There are several important differences between two-dimensional and axisymmet-

ric flows in the fixed volume release experiments. With no parallel restraining boundaries, a fluid released into another fluid of different density spreads out in all directions. This will affect the propagation speed simply based on the mass conservation. In early cylindrical spreading experiments, after a rapid initial collapse, a roughly axisymmetrical spread of the fluid was observed (Penney and Thornhill, 1952). Hoult (1972) used the cylindrical box model to show that the distance travelled by the front varies with the time, t, to the power of 1/2. Sector tank experiments show the distance from the start is proportional to $t^{2/3}$ (Simpson, 1997).

In addition, Simpson (1997) stated that the dense fluid spreading in the sector tank forms a concentrated front or multiple fronts, leaving only a thin layer of heavy fluid in tails near the ground. This multiple-front phenomenon was also observed in cylindrical release laboratory experiments (Chen, 1980; Maclatchy, 1999) and numerical models (Cantero et al., 2007a), in which they described the multiple fronts as vortex rings. Vorticity is concentrated in the multiple fronts of cylindrical currents and is intensified due to vortex stretching with the decreasing of cross-sectional area (Patterson et al., 2006). The front is followed by a backward-facing hydraulic jump, which is the result of a post-rarefaction wave that is reflected from the origin and propagates radially outward more rapidly than the front itself (Rottman and Simpson, 1983, 1984). In experiments in which channel width is suddenly doubled, the leading-edge vortex rolled up as the width of the front increased and reached almost down to the bottom of the channel. Ungarish and Zemach (2005) provided a complete overview of the modeling of high Reynolds number gravity currents in two-dimensional and axisymmetric configurations. Cantero et al. (2007a) show that in the cylindrical configuration Kelvin-Helmholtz (K-H) vortices form at the interface, while at the bottom boundary they set up and form a vortex ring, and eventually

the current has a highly turbulent front with a relatively shallow calm body. The coherent K-H vortices undergo azimuthal instabilities and break up into small-scale turbulence. Such instabilities grow in size and extend to the current front interface, which corresponds to the lobes and clefts structure along the front first observed by Simpson (1997). The stretching of the vortex rings along the azimuthal direction stabilizes the Kelvin-Helmholtz structure and slower down the transition into fully developed three-dimensional turbulence (Cantero et al., 2007a). This stabilization due to azimuthal stretching of vortex rings has a stronger influence in the low Reynolds number case than the high Reynolds number experiments.

Alahyari and Longmire (1996) also observe this vortex pair structure in the axisymmetric gravity current head during the inertia-buoyancy phase of axisymmetric laboratory gravity current experiments. Using particle image velocimetry, velocity fields are determined which clearly show a cyclic process of vortex pair formation in the head: a counterclockwise vortex first forms at the leading edge due to baroclinic vorticity, followed by the formation of a clockwise vortex along the bottom surface, and convection of heavy fluid forward by the vortex pair. The induced velocities caused by the vortex pair results in a high-speed flow and the fluid from behind is continuously pumped into the developing head of the current (Alahyari and Longmire, 1996). This vortex pair phenomenon has also been observed in velocity field of cylindrical release in the laboratory experiments by (Patterson et al., 2006) and DNS models by Cantero et al. (2007a). The vortex pair is believed to explain the remarkably larger head which forms in axisymmetric gravity current experiments than in 2D gravity current experiments.

However, none of these previous experiments have considered gravity currents supplied by a steady input of dense (or light) fluid. Usually, within one tidal cycle

the freshwater inflow is constant rather than a sudden release of a fixed volume of fluid. One example of constant inflow source flow is the warm outflow from a power station. These so-called starting plumes are different from the lock exchange flows (Simpson, 1997). In the fixed volume release experiment, the current transitions through different phases, namely acceleration, slumping, inertial and viscous, while the steady input current does not reach the latter two phases at all. It has been shown that for an inlet Froude number greater than 1 there exists an entraining hydraulic jump at the interface between the fluids, which has been called the lift-off region in the context of river plumes. This hydraulic jump is able to entrain a varying amount of ambient fluid to satisfy a range of downstream conditions. The spread of cylindrical plumes with constant flux has been analyzed and described by Chen and List (1976), Britter (1979) and Linden and Simpson (1985) using laboratory simulations. All the available experiments show periodic oscillations in the form of the multiply fronts when the gravity current spreads out after passing through a narrow slot. These oscillations correspond to the multiple-fronts phenomenon observed in the vertical shadowgraph images in the sector tank release experiment (Patterson et al., 2006) and the density contours in the DNS numerical simulations (Cantero et al., 2007a).

Several researchers have reported similar concentric rings or multiple fronts in their field observations. McClimans (1978) reported this phenomenon in a natural buoyant discharge into a fjord. Garvine (1984) showed a multiple fronts structure in thermal images of the plume of the warmer Quiault River discharging into the Pacific Ocean. A frontal ring structure is derived from Garvine's numerical modeling and compared to Chen's (1980) solution. Garvine (1984) suggested that the interaction of the leading front and the nonlinear internal waves are present in radial, gravitational spreading gravity currents. This might be the source of the multiple rings structure

observed in the thermal plume images, but his numerical model only predicts the frontal ring, not multiple rings with consecutive fronts. Luketina and Imberger (1987) observed concentric form lines, which are the surface manifestation of the multiple rings, in Koombana Bay. They revealed a subfrontal feature with large horizontal density gradients approximately 90 m behind the leading edge of the plume in one CTD yo-yo section. The subfront has a slightly higher propagation speed then moved toward and was pulled into the frontal bore structure. There is strong convergence and downwelling at the leading edge of each subfront. Similar to a large rotor in the plume front, a smaller rotor in the streamline data was observed within the subfronts. Recently Halverson and Pawlowicz (2011) also reported multiple instances of steep salinity gradients in the CTD transect at Fraser River plume.

To study the generation mechanism of this multiple fronts structure in the river plume system, we conducted two sets of laboratory experiments with laterally confined (Figure 4.1a) and unconfined (Figure 4.1b) configurations. The former configuration simulates the current in the channelized estuary and the latter one simulates when the gravity current leaves the river mouth and flows into the unbounded ocean. We expect to observe the multiple fronts structure in the laterally unconfined situation, which is similar to the classical cylindrical dense current release lock-exchange experiment. The manuscript is organized as follows. We first review the two-way exchange flow theory in §4.2. We examine the exchange flow through a contraction/sill and show how, by allowing the buoyant fluid to spread laterally, the river plume system might be a source of internal solitary waves with trapped cores. Experimental set-ups are described in §4.3 which are exactly the same as the experiments for Chapter 3. In §4.4.1 we discuss the plan-view depth fields from the qualitative dye laterally unconfined experiments to show the general plume properties. The large-scale structure

will be first observed in the depth field and their propagation speed and frequency will be calculated. In §4.4.2 we examine the differences in vertical structure and vortex dynamics between experiments with and without lateral boundaries. We discuss the spectral analysis and spatial linear stability analysis to show that the large-scale structures are internal solitary waves generated when current flow into the laterally unbounded ambient water. We also show that the river plume system is a potential source of generate large-scale structure in addition to the small-scale Kelvin-Helmholtz instability in the typical shear stratified flow. Finally, we discuss the formation of the trapped vortex cores within this non-linear internal solitary waves in §4.4.3.

4.2 Background theory

Benjamin (1968) developed a theory for the propagation of a steadily advancing current in a fixed-volume release experiment. In a frame of reference moving with the front, the fluid in the current is at rest. By assuming that energy is conserved within the control volume, he determined the frontal Froude number $F_H = U/\sqrt{g'H}$ to be one-half in the case where the moving current depth is half of the channel depth, where U is the current speed, H is the channel depth and $g' = \frac{\rho_1 - \rho_2}{\rho_2} g$. More recently, Shin et al. derived a new energy-conserving theory for partial depth releases including the wave propagation in the system and determined the frontal Froude number to be $F_H = 1$. Typically, the gravity current generated by releasing a fixed volume of fluid into a fluid of different density in the lock-exchange experiment is unsteady without the source supply. In the case of the constant river outflow, it has been shown that the two-way exchange flow theory derived by Farmer and Armi (Farmer and Armi, 1986; Armi and Farmer, 1986) is better suited to describe the flow properties of the steady input plume than the traditional energy conserving theory. Here we briefly

review the concept of internal hydraulic controls and their relevance to the internal waves. We hypothesis that the way lateral spreading impacts on the river outflow is similar to the stratified flow exists a restrictions, such as a horizontal expansion and the vertical depth shoaling through the topographic changes. We will review the energetic stratified flow over such topographic changes in the literature, especially the internal solitary waves generated at their hydraulic control points. Finally, a numerical simulation of trapped vortex cores formation within these internal solitary waves vis depth shoaling by Lamb (2002) is reviewed and analogized to the present study.

4.2.1 Hydraulics of two-way exchange flow

The hydraulic theory for the flow of two fluids of different densities through variations in geometry is described in Armi (1986). The special case of two counter-flowing layers in a contraction is considered by Armi and Farmer (1986). They defined the hydraulic composite Froude number:

$$G^2 = F_1^2 + F_2^2 \qquad \text{for} \qquad g' \ll g, \tag{4.1}$$

where $F_i^2 = U_i^2/g'y_i$ is the densimetric Foude number for layer i, U_i is the flow speed, y_i is the layer thickness and $g' = g\frac{\Delta\rho}{\rho_2}$ is the reduced gravity, in which subscript $i = 1$ stands for the upper light fluid layer while subscript $i = 2$ stands for the lower heavy fluid layer. Exchange flows through the contraction normally have two control locations, at which the flow is critical to long internal waves, i.e., $G = 1$. 'Weak', 'moderate' and 'strong' barotropic flow regimes are differentiated by the net barotropic flowrate based on the value of G in the two-layer system.

The flow regime investigated in this manuscript considers the limit of moderate and strong barotropic flow. In this case, when the barotropic flow exceeds its critical

value, a transition occurs from two-way exchange flow into a single-layer flow because one layer is arrested. Under this condition the Froude number depends solely on the layer that flows. Here we define the intermediate and strong barotrapic flow ($U_0 \geq U_T$) in river plume as 'inverted box flows' (Figure 4.2), which is modified from definition of 'box flows' described by Armi and Farmer (1986). Inverted box flows of this type have a common geophysical analogy in the river plume and salt wedge at the mouth of an estuary. In the extreme case, when $U_0 > \sqrt{g'y_i}$ then $G > 1$, where the subscript i refers to the single moving layer. Under this supercritical inflow conditions, currents can no longer be satisfied at the narrowest section, which is then filled with a single moving layer. Downstream of the narrowest section the flowing layer decelerates and at some width b_f reaches critical conditions: $F_i^2 = 1$. In the river plume system, the narrowest section is the river mouth and the hydraulics control point is the 'lift-off' region.

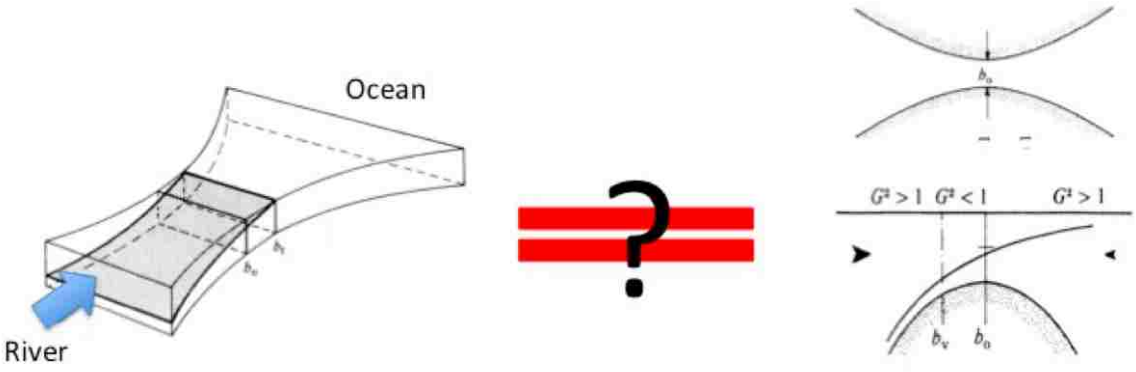

Figure 4.2: Schematical comparison between 'inverted box flows' (*left*) and classical two-way exchange flow over sill and contraction (*right*). 'Inverted box flows' is modified from the definition of 'box flows' model described by Armi and Farmer (1986) Figure 10: perspective view of intermediate box flow in which the interface meets the surface upstream of the narrowest section. The classical two-way exchange flow model is after Farmer and Armi (1986) Figure 12: the sketch of plan view and side view of two-way exchange past a coincident sill and contraction with strong barotropic component.

4.2.2 Generation of internal solitary waves: stratified flow over contraction and sill

Energetic two-layer flow over the sill and contraction often relates to the internal solitary waves (ISW), which are released at the hydraulic control point. In this section I review some reported nonlinear internal solitary waves in ocean and analogize their generation to the energetic near-field river plumes.

Farmer and Smith (1980) reported a phenomenon associated with internal wave formation in which water is stratified across Knight Inlet by tides. Farmer and Armi (1999) followed by Afanasyev and Peltier (2001) investigated the detailed internal solitary wave generation and breaking over the sill. They observed the development of finite-amplitude Kelvin-Helmholtz billows in the shear layer on the downstream side

of the sill crest. Clear evidence of shear instability within internal solitary waves was obtained in acoustic images taken in Knight Inlet Farmer and Smith (1980). Within one tidal cycle the flow over the sill in Knight Inlet is considered to be in quasi-steady state and the supercritical condition over the crest is believed to be nevertheless able to support a train of large amplitude lee waves. There is an enhancement of the amplitude as the waves move into the narrower section of the inlet, which is associated with a net deepening of the surface layer. This internal bore structure travels on a shallow top layer and is similar to that observed during a period of weak stratification by Farmer and Smith (1977). Pawlak and Armi (2000) simulated mixing and entrainment in the arrested wedge flow over the sill in their laboratory experiments. The temporal sequence of density profiles clearly reveals large-scale structure with a wavelength of approximately 40cm. Spectral analysis of the density field indicates two frequency peaks, with the lower one corresponding to these larger-scale structures. Small-scale Kelvin-Helmholtz instabilities were observed to develop within the mixing layer, concentrated primarily in the 'nodes' of the lager-scale structure.

The Strait of Gibraltar is another illustrative example of a two-way flow through a strait that includes both a sill and a separate contraction (Farmer and Armi, 1986). The semi-circular banded structure is the surface manifestation of an internal undular bore, which forms when the flow goes through the complex topography radiating into the Alboran Sea. Kinder (1984) addressed this feature as the release of energy associated with deformation of the interface downstream of the sill crest as the outflowing tide slackens and subsequently evolves into a train of nonlinear internal waves (Farmer and Armi, 1986). In this moderate flow regime by a strong tide, flow passes through an asymmetric structure of maximal two-way exchange, in which the two sides of the narrowest section both are supercritical ($G > 1$).

4.2.3 Formation of trapped vortex cores within ISW via shoaling in depth

Moum et al. (2003) observed internal solitary waves propagating shoreward over Oregon's continental shelf from high acoustic backscatter data. They provided a vivid illustration of shear instability along the ISW. K-H instabilities start to be generated about half-way to the wave trough and the size of K-H billows increase toward the trough. At the trailing edge of the ISW, K-H billows is much less organized, suggesting turbulent breakdown. The local compression of isopycnals during ISW passages generates small-scale shears and corresponding small-scale instabilities at the wave trough. These ISWs are continually triggering instabilities at the wave edge as they propagate. Lamb and Farmer (2011) simulate the ISW under this condition from numerical model, suggested that the K-H billows along the wave edge occur when Ri_g is less than 0.1 and $L_x/\lambda > 0.8$, where L_x is the length of unstable region with $Ri_g < 0.25$, $Ri_g = \frac{g}{\rho_0}\frac{\partial\rho/\partial z}{(\partial u/\partial z)^2}$ is the gradient Richardson number, and λ is a half wavelength of the wave. The simulated ISW has a trapped surface core which is similar to the phenomenon when ISW shoaling in depth (Lamb, 2002). Lamb (2002) also found that waves with trapped cores are easily formed in the density field for which buoyancy frequency increases monotonically towards the surface. An upper mixed layer completely eliminates the formation of waves with trapped cores.

4.3 Experimental setup

This experiment was conducted in a 4 m $\times$ 2.5 m $\times$ 0.7 m plume basin, which is exactly same as in §3.2. The inflow was introduced into the plume basin through a small estuary tank, containing a diffuser board and a honeycomb to achieve uniform flow characteristic. Each experiment started by opening the estuary gate and the buoyant water valve simultaneously. After propagating across the plume basin, mixed

fluid exited the system over an adjustable weir at the downstream end of the basin.

All sixteen experiments (eight for spreading and eight for channelized case) were conducted in a plume basin. Here we mostly focus on the two highest Fr_i cases (details in §3.2 SP4 and CH4). The inflow condition for both experiment were characterized in terms of the inflow Froude number, $Fr_i = \frac{U_0}{\sqrt{g_0' H_0}}$, where U_0, g_0' and H_0 are the inflow velocity, inflow reduced gravity and inflow depth, respectively. In the unconfined case (SP4, $Fr_i = 2.14$) the estuary tank was located at the center of one end of the plume basin. By lifting the gate and opening the valve, the buoyant fluid was released from the estuary channel into the ambient water where it was allowed to spread freely. For the confined case (CH4, $Fr_i = 1.84$) the estuary tank was oriented between the tank wall and a vertical plastic wall so that the current was forced to stay within two lateral boundaries.

The plan-view experiment was only conducted in the spreading case with the freshwater thickness data measured by the optical thickness method. It provided comprehensive imaging of the entire plume structure from the freshwater thickness field. Vertical laser experiment provides the density and velocity field for both spreading and channelized cases using a combined particle image velocimetry (PIV) and planar laser induced fluorescence (PLIF) technique (Horner-Devine, 2006). This technique measures velocity and density fields at short time intervals from a sequence of image triplets taken with a digital camera fitted with a wavelength cut-off filter. The velocity field is obtained from the first two images, in which small PIV particles illuminated by YAG laser, using matPIV code (Sveen, 2004) in matlab program. The third image in the sequence is illuminated by the Argon ion laser with florescent dye and processed using PLIF technique (Crimaldi, 2008). The field of view of this method is a small vertical plane (12 cm $\times$ 14 cm) along the plume center line ($y = 0$), only tenth of the

area in the plan-view experiment.

4.4 Results

4.4.1 Plan-view plume depth field

The development of a freely spreading gravity current is shown in Figure 4.3 a and b for an supercritical inflow plume ($Fr_i = 2.14$) , presenting freshwater thickness field snapshots of the flow. The inflowing buoyant water is observed to spread laterally and form a cone-shaped surface layer. The structure and evolution of this surface layer highly depend on the inflow Froude number. The flow is supercritical and the plume is a jet-like current with an offshore velocity much higher than the cross-stream velocity. Although the plume shoals significantly in unconfined cases, the frontal bore (Figure 4.3 a and b red arrows) has a thickness similar to the confined case. This is because the frontal bore entrains the fluid behind it, leaving a relatively thin trailing layer. The frontal bore in the freshwater thickness field appears as a bright (deep) ring with a darker ring inside of it indicating a band of reduced layer thickness.

After the frontal bore passes by, several periodic deep bands (Figure 4.3 a and b blue arrows) start to be generated near the river mouth ($x = 0; -15 < y < 15$). In Figure 4.3a, only one deep band can be observed, whose depth is almost as the same as the frontal bore. It propagates offshore with the frontal bore. Later, the frontal bore almost damps to the same depth as the surrounding current, while the first deep-band also becomes shallower as they both propagates offshore. Three more deep bands have been generated near the river mouth (Figure 4.3b).

A series of freshwater thickness profile along $y = 0$ line is plotted in Figure 4.3c. Profiles color change from black into light gray as time increases, the darkest line is the same as Figure 4.3a and the lightest line is 1 second later than Figure 4.3b.

The small-scale fluctuations are mostly like to be the Kelvin-Helmholtz instabilities. The frontal bore and the deep bands can be also observed as the large-scale depth oscillations at the plume depth profile. Unlike the K-H-like instabilities in channelized cases, this oscillation has a lower frequency (higher wavelength). This is the so-called large-scale structure and is hypothesized to be generated in high Fr_i with the lateral spreading. we will focus on the generation, dynamics and impact of this large-scale structure in the this chapter.

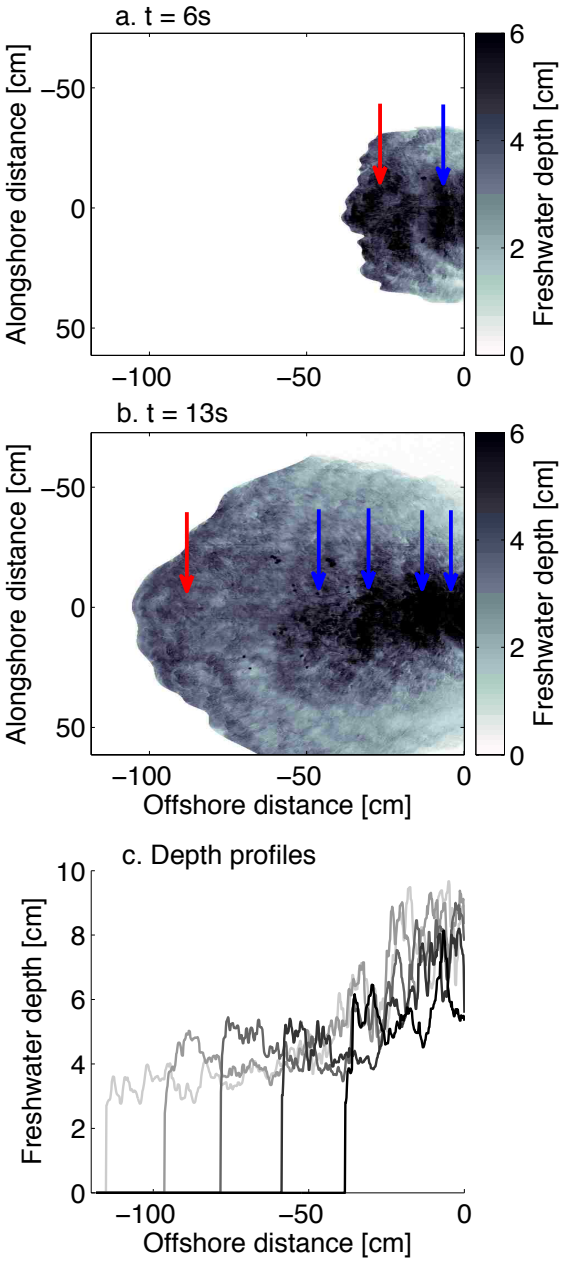

Figure 4.3: Plume front in plan-view freshwater thickness images for a) plume front (t = 6 s) and b) plume front after (t = 13 s). c) Freshwater thickness time series along $y = 0$ line, time increases with line color changes from dark black into light gray. Red arrows in panel (a) and (b) indicate the frontal bore, blue arrows indicate the deep-band structure generated near the river mouth.

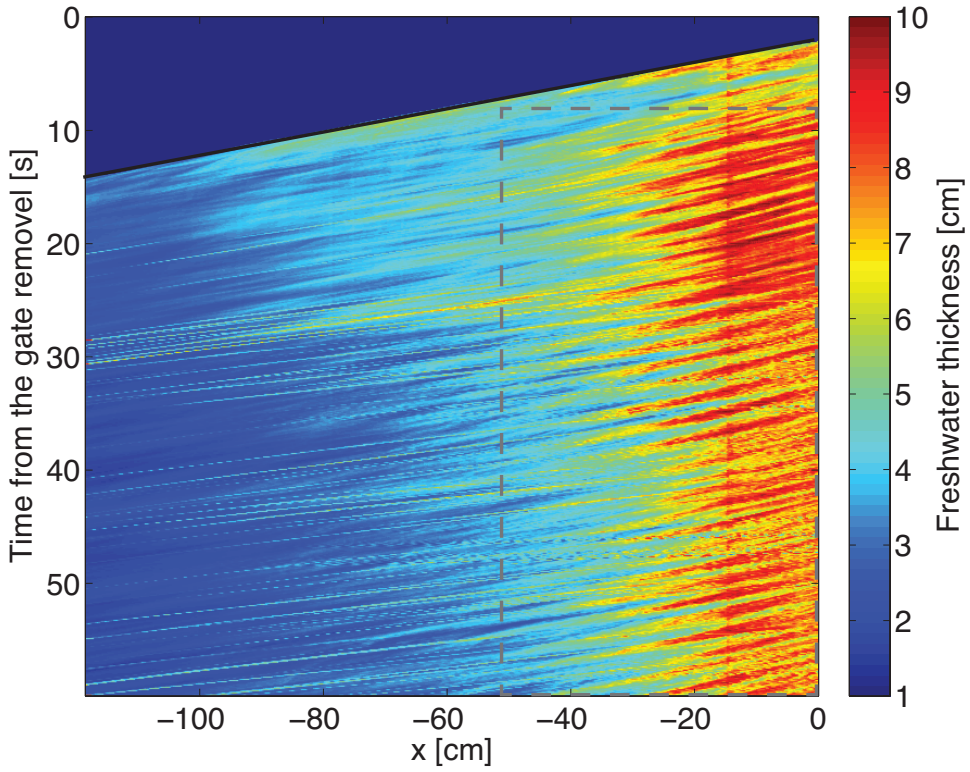

Figure 4.4: x - t diagram generated by combining the time sequence of the freshwater thickness observed in Figure 4.3 c. The blue area in the upper right corner indicates the region before frontal bore arrives. Diagonal red streaks represent large-scale structure propagates offshore as interfacial waves.

Wave evolution

The wave propagation of these large-scale structure can be seen in the x-t diagram of the characteristics in Figure 4.4. The characteristics represent a compilation of the freshwater thickness in a sequence of 600 images (60 s). The blue region in the upper right corner indicates the region before frontal bore arrives. Red diagonal lines represent the propagating large-scale structures offshore. In general these structures

propagate at a nearly constant speed near the river mouth ($|x| < 50$ cm). After it, the plume is not energetic enough to generate those large-scale structures ($|x| > 50$ cm), so the streaks damped out in the far end of the field of view.

To further analysis the wave evolution we generate a wavenumber-frequency ($k-f$) spectrum using the data within the gray box shown in Figure 4.4 ($0 < |x| < 50$ cm and $15 < t < 60$ s). This technique has commonly been used in the nearshore wave studies (Oltman-Shay et al., 1989; Bowen and Holman, 1989). By transforming from the x-t diagram into $k - f$ spectrum, a clear offshore propagation line can be observed as the red streak (labeled as black dash line) in Figure 4.5 a. This line has a relatively constant slope, which indicates the large-scale structure we are interested in propagate offshore at a constant speed. This wave speed $c \approx 0.04$ ms^{-1} equals to the average current speed, i.e., $Fr \approx 1$, where $Fr = c/U$ is the in-situ Froude number and average current speed U is half of the maximum horizontal velocity in the shear layer. In addition to the propagation speed, $k-f$ spectrum also provides information on the dominate frequency (wavenumber) of this specific wave. We identify a dark red peak in the $k - f$ spectrum (pointed by a purple arrow in Figure 4.5 a). By integrating the power density at each frequency within the gray box in Figure 4.5 a, a clear peak of the power reveals at Figure 4.5 b (also pointed by a purple arrow). This peak frequency is 0.18 Hz, within the range of $0.1 \sim 0.2$ Hz for the large-scale structure calculated before.

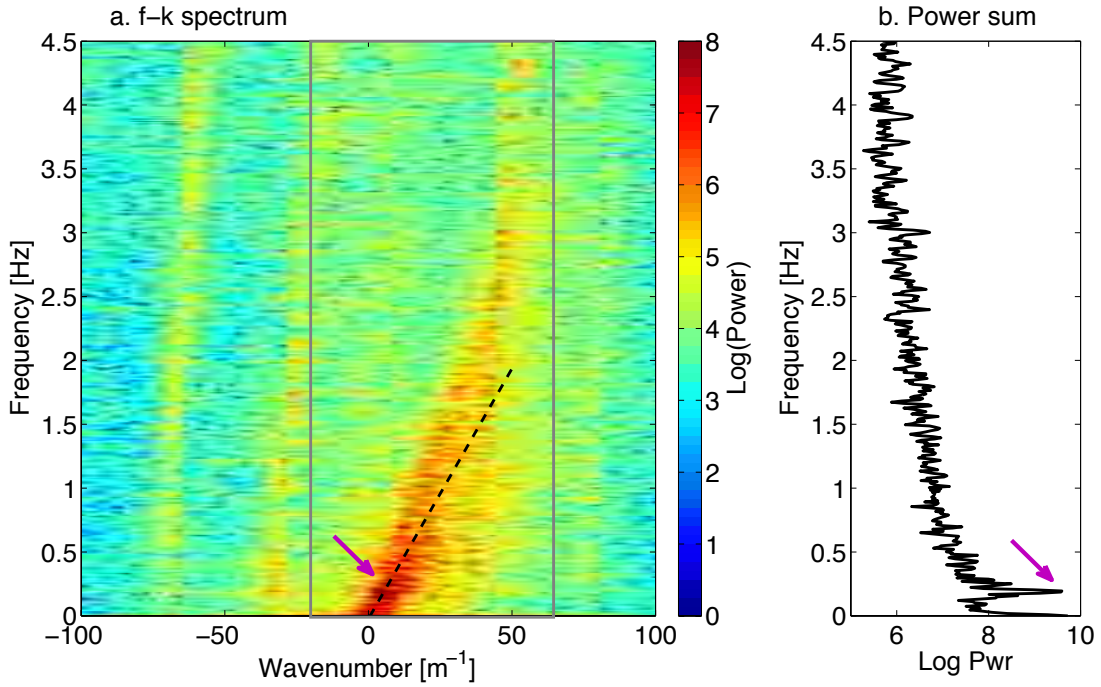

Figure 4.5: a) Estimated wavenumber-frequency spectrum of freshwater thickness generated from the data in Figure 4.4. Positive wavenumbers indicate offshore propagation. The black dash line marks the propagation of large-scale structure. Its slope is the propagation speed, $c \approx 0.04$ ms^{-1}. Three other red streaks in the $k - f$ spectrum may be generated from some unclear reason and will not be discussed here. Sum of power density within the gray box in (a) is plotted against the frequency in (b). It has a peak at $f = 0.18$ Hz, indicated as a purple arrow. Same peak is also identified in (a) as a dark read region pointed by a purple arrow.

4.4.2 Vertical flow structures

Plume vertical density field sequence

While the plan-view experiment provides the comprehensive plume structure of the spreading case, vertical density and velocity fields near the river mouth at similar conditions for both channelized and spreading cases are obtained from the combined PIV-PLIF method. Direct comparison between two cases are shown in Figure 4.6 for

channelized case and in Figure 4.7 for spreading case. The left-hand columns in two figures are for the frontal propagation region, represents the same time as in Figure 4.3a. The frontal bore in spreading case has a thickness similar to the channelized case, similar to the observation in the plan-view depth field. At the leading edge of the frontal bore, a small Kelvin-Helmholtz (K-H) billow starts to be generated at the sharp interface due to the high shear. This generation of K-H billow is more clear in the spreading than in the channelized case. A detailed discussion of the generation of small K-H billows along with the large-scale structure is in Appendix A.1.

In addition to the difference in the generation of K-H billows at the leading edge of the plume front, a more pronounced difference is the periodically large-scale structure in the spreading case: each large-scale structure acts like an individual front. The right-hand columns in two figures are at the same time in the steady-state region. In the channelized case, current is like the classical lock-exchange experiment with an almost uniform interface between two fluids (Figure 4.6). The mixing and entrainment of the dense ambient water into the plume is generated by the Kelvin-Helmholtz instability, however no clear evidence of the generation, development and breaking region of the K-H billows can be identified. On the other hand, in the spreading case, the series shown in here is right after the last structure passes offshore. The current turns into a highly stratified region, and then a sharp interface between two fluids forms right at this turbulent region. several small-scale K-H billows can be clearly identified at the shear layer (Appendix A.2).

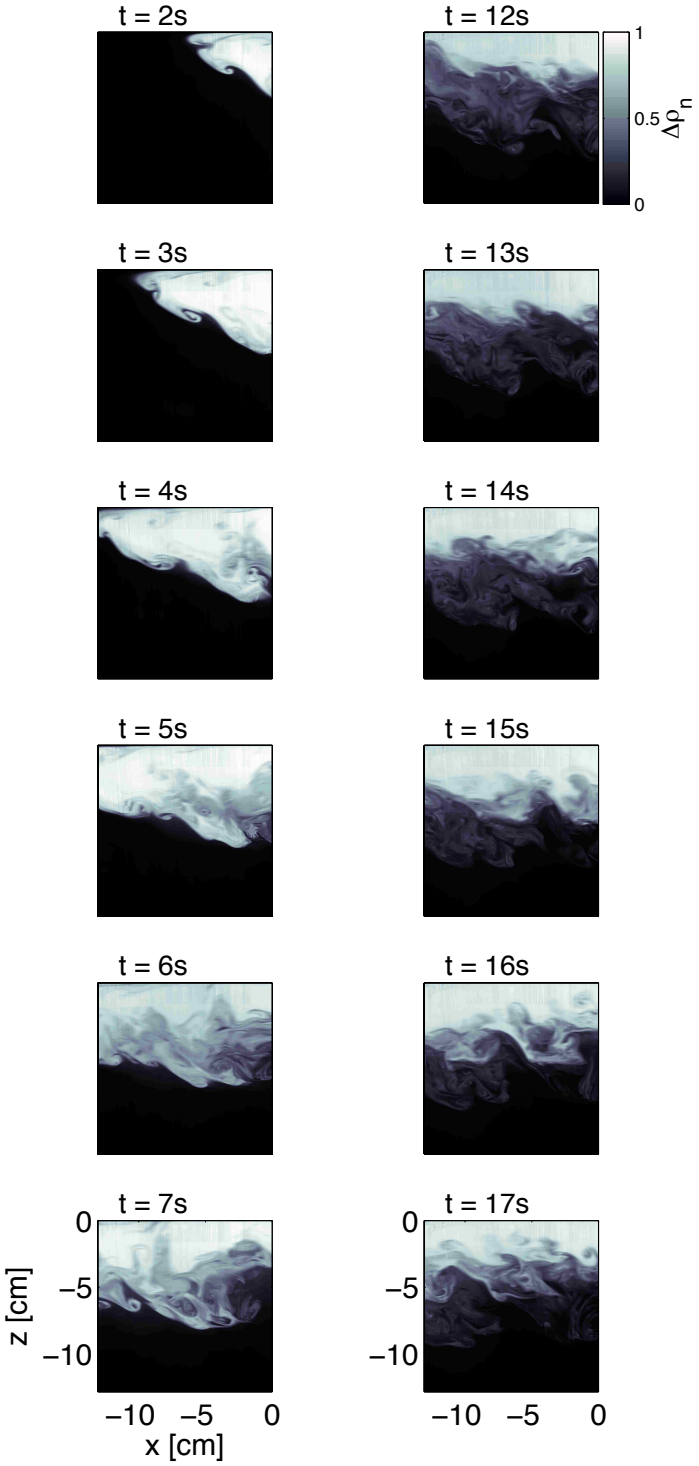

Figure 4.6: Normalized density anomaly field sequence at the plume front region (left-hand column) and steady-state region (right-hand column) for channelized case (CH4). Time increases downward at each column, time interval between two frames is 1 s. Physical dimension of this field of view is labeled at the lower-left corner.

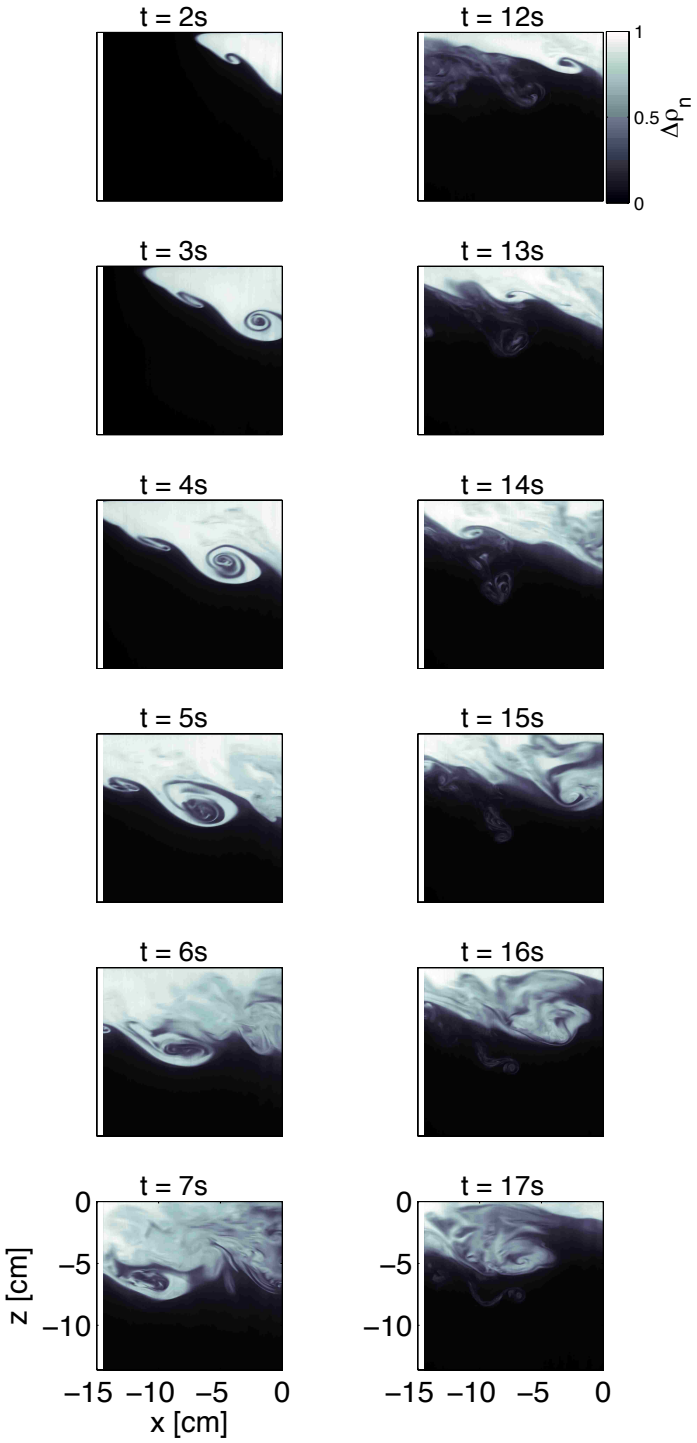

Figure 4.7: Same as Figure 4.6 but for a spreading run (SP4)

Plume density profile time series

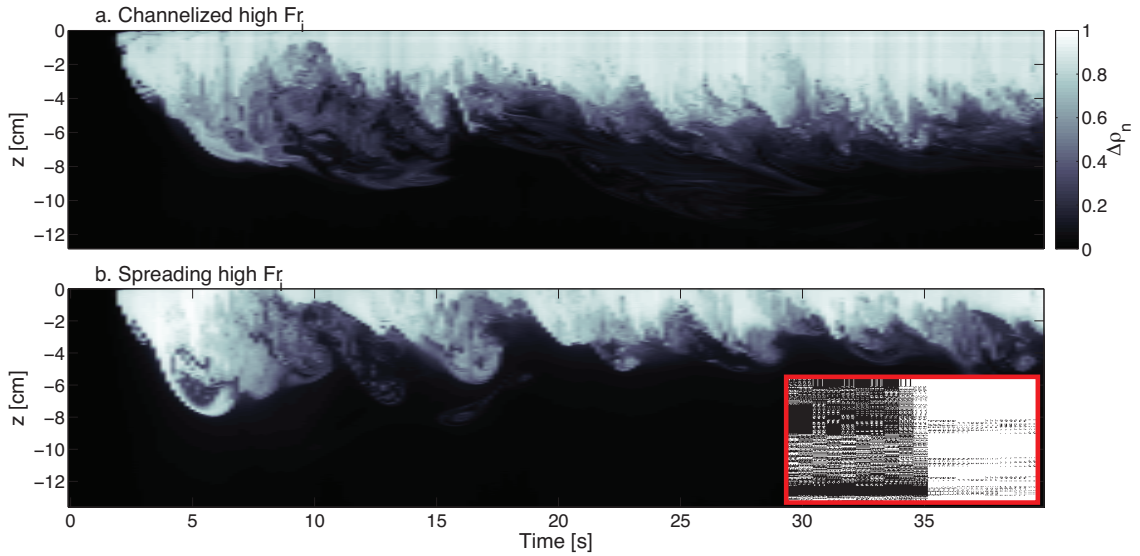

Figure 4.8: Temporal sequence of vertical density profile at the center of PLIF field of view for a) channelized and b) spreading cases. Inset in b) is a copy of initial phase of 10 degree sector tank lock-exchange experiment from Simpson (1997)

Plume structures evolution is clearly observed but hard to be quantified in the vertical-view experiment, since the spatial extent of the individual images was limited to about 12 cm. This limitation can be overcome with a time series constructed from a vertical density profile at a given location in spatial image. Figure 4.8 shows a 40 s time series at the center of the PLIF field of view, which clearly reveals the frontal bore region and the large-scale structure we mentioned in § 4.4 and § 4.4.2. A significant difference between channelized and spreading plume can be identified after the frontal propagation ($t > 10$ s). Five long temporal (low frequency) structures within $30 \sim 35$ s is observed in the spreading cases, resulting a period $T \approx 6 \sim 7$ s. A spatial length scale can be inferred by assuming a convective velocity of $U_m/2$, where U_m

is the maximum velocity within the plume layer. The corresponding wavelength of the structure is approximately 30 cm. Small-scale Kelvin-Helmholtz instabilities are visible at the 'braid' of this large-scale structures. Within one large-scale structure, a sharp interface at the 'front' side with one or two developing K-H billows. Such K-H billows tend to break at the trough of the large-scale structure and then turns into fully developed turbulence at the trailing edge.

To compare the evolution of the plume layer thickness with time in spreading cases and channelized cases, we examine the vertical density field data from density profile time series. The mixing layer thickness δ_ρ is defined as the inverse slope of the best-fit line through the normalized density anomaly profile between the 15% and 85% values.

$$\delta_\rho = \left(\overline{\left. \frac{d\rho}{dz} \right|_{\Delta\rho_n(z)=0.15}^{\Delta\rho_n(z)=0.85}} \right)^{-1}, \tag{4.2}$$

The similar definition can be applied to the normalized velocity profile to calculate the vorticity thickness, as suggested by Pawlak and Armi (2000). Here we choose the density thickness to represent the mixing layer thickness because the density anomaly profiles and velocity profiles are almost identical in the experiments expect to two low Fr_i spreading runs (Yuan and Horner-Devine, submitted). This mixing layer thickness represents the layer where the mixing and entrainment happens, excluding the top constant density layer in the channelized case. Yuan and Horner-Devine (submitted) examined the mixing from the averaged data and concluded the main impact of lateral spreading on the mixing in the same experiment is eliminate the top constant density layer and rise the mixing layer to the water surface. We use the normalized density anomaly profiles at the center of PLIF field of view and calculate δ_ρ for four runs shown in Figure 4.9. Dash line is the channelized cases, the plume thickness increases as the

frontal bore passes by. It then stays at an approximately constant value, with small oscillations corresponding to K-H instabilities at the shear layer. On the other hand, δ_ρ dramatically decreases after the frontal bore region in spreading case (solid line in Figure 4.9). This is consistent with the observation at lock-exchange experiment in sector tank by Simpson (1997) and DNS models of cylindrical release gravity current by Cantero et al. (2007a). The frontal bore entrains most of the fluid behind it due to increasing internal rotation in frontal bore. Cantero et al. (2007a) hypothesized that this increasing of rotation in the frontal bore is because of the lateral stretching at a result of lateral spreading in the cylindrical gravity currents. In this case, the majority of fluid is concentrated within the frontal bore, following by a relatively thin layer. In addition to the differences in frontal bore, we also observe δ_ρ continuously oscillates at a almost constant frequency in the high Fr_i spreading case.

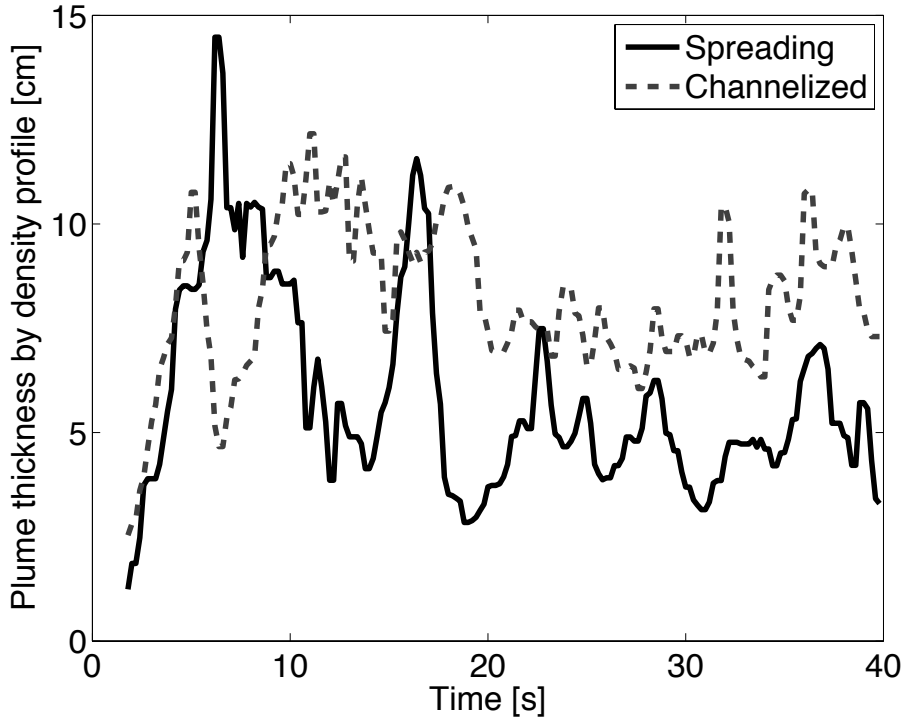

Figure 4.9: Plume thickness, δ_ρ vs. time t.

This large-scale structure has been previously observed in several cylindrical release laboratory experiments (Simpson, 1997; Chen, 1980; Maclatchy, 1999; Patterson et al., 2006) and numerical modeling (Cantero et al., 2007a). The insert of Figure 4.8 shows at the initial phase of the lock-exchange experiment in sector tank, several large-scale structure were clearly identified. Simpson (1997) concluded this feature as vortex ring structures which is generated by intensified vorticity because of the lateral spreading. As the cross-sectional area decrease, the conservation of angular momentum leads to an intensification of vortex. This process is largest during the rapid expansion near the source and produces a large vortex which occupies almost the full depth of the dense fluid. Patterson et al. (2006) and Alahyari and Longmire

(1996) observed similar flow pattern in the axisymmetric gravity current. They came with a different explanation on the formation of such multiple rings. They analysis the velocity using the particle image velocimetry method and found a vortex pair formation in the head. This hypothesis was supported by Cantero et al. (2007a) DNS model, who also observed a vortex pair within each large-scale structure. However, all of these experiments included a fixed-volume of gravity current, so that this vortex rings structure damped out after their initial stage of release.

Pawlak and Armi (2000) found similar large-scale structures in a hydraulically controlled, arrested wedge stratified flow in their laboratory experiments. Their experiment was designed to simulate the flow over a sill in Knight Inlet in British Columbia by Farmer and Armi (1999). Stratified flow is constrained in a rectangular channel with a constant sloop sill at the center. They observed a sequence of large-scale structure in the low-entrainment developing region after the initial high-entrainment stage. Unlike a single vortex nor a vortex pair within those large-scale structures suggested by previous axisymmetric lock-exchange laboratory experiment, they found that the vorticity is highest along the 'node' of the large-scale structures. They also showed evidence that small entraining scales are correlated with the large-scale structure.

Spectral analysis

Time series of vertical density profiles (Figure 4.8) appears to contain a periodic component for a period around $6 \sim 7$s, which is consistent with the length scale of the large-scale structure by multiplying a velocity of $U_m/2$. To examine this in more detail, the power spectrum of normalized density anomaly was computed for each pixel at the density interface and then averaged horizontally and vertically. The averaged power spectrum is plotted in Figure 4.10 for spreading case and channelized

case. The 2σ intervals indicated as circles were derived from the chi-squared approach. Notable peak in spreading case appears at $0.1 \sim 0.2$ Hz while there is no clear peak is channelized case. This broad peak in the spreading case is consistent with the period of the large-scale structure observed in Figure 4.8.

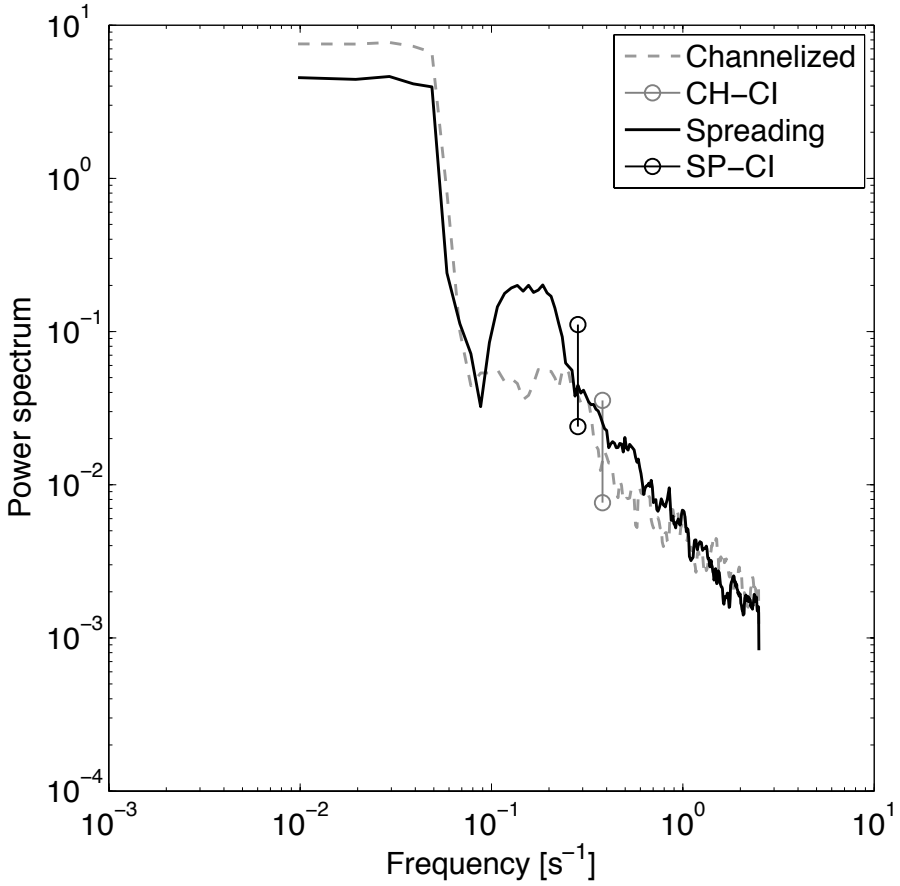

Figure 4.10: Power spectrum of the plume normalized density anomaly for the spreading (black solid) and the channelized (gray dash) with their respective 2σ confidence intervals labeled as circles. Both spectra were calculated using the multitaper method and averaged over 100 pixels horizontally and vertically.

One general concern regarding to the spectral analysis is whether this frequency

peak is generated by the boundary effect of the rectangular tank. This effect may be intensified in the spreading case with some unclear reason. To answer this question, here I calculate the sloshing frequency based on the length (L) and the thickness (H) of the plume basin, using the equation of

$$\omega = \sqrt{gk \tanh(kH)}, \tag{4.3}$$

where k is the wavenumber corresponding to a wavelength $\lambda = 2L$, i.e., $k = \frac{2\pi}{2L}$. This results to a sloshing frequency $\omega = 0.3$ Hz, different from the frequency peak we observed in Figure 4.10. So we can conclude that the peak in the spectrum shows the different dynamics between the spreading and channelized plume, which is not caused by the artificial mechanism generated from the experiment.

Linear stability analysis

A spatial linear stability is used in order to investigate the potential instability modes in the flow. We follow Taylor and Goldstein (TG) method to assess the stability of the flow on the background profiles of density and horizontal velocity in spreading and channelized cases. We use the numerical method described by Moum et al (2003) to generate the solution of the TG equation based on averaged velocity and density profiles. Here we assume that the instabilities are two-dimensional, which means they do not vary in the lateral direction (y). This is not a perfect assumption in studying the shear instabilities; especially in the spreading cases we intend to have the spanwise velocity and velocity gradient. But this two-dimensional analysis will provide us a potential range of wave number and growth rate on instabilities of interest. Each profile, a xx s average, is an average over sufficient instabilities. Profiles are then smoothed using a low-pass filter to remove instability associated with small-scale variations.

For given velocity profiles in channelized or spreading cases, density anomaly profile $\Delta\rho(z)$ (Figure 4.11a and 4.12a), $U(z)$ (Figure 4.11b and 4.12b), buoyancy frequency (N^2) and shear square ($(dU/dz)^2$) are calculated to get the Gradient Richardson number (figure Figure 4.11e and 4.12e). The potential mixing regions ($Ri_g < 1/4$) are indicated as shadow region in the Ri_g profile.

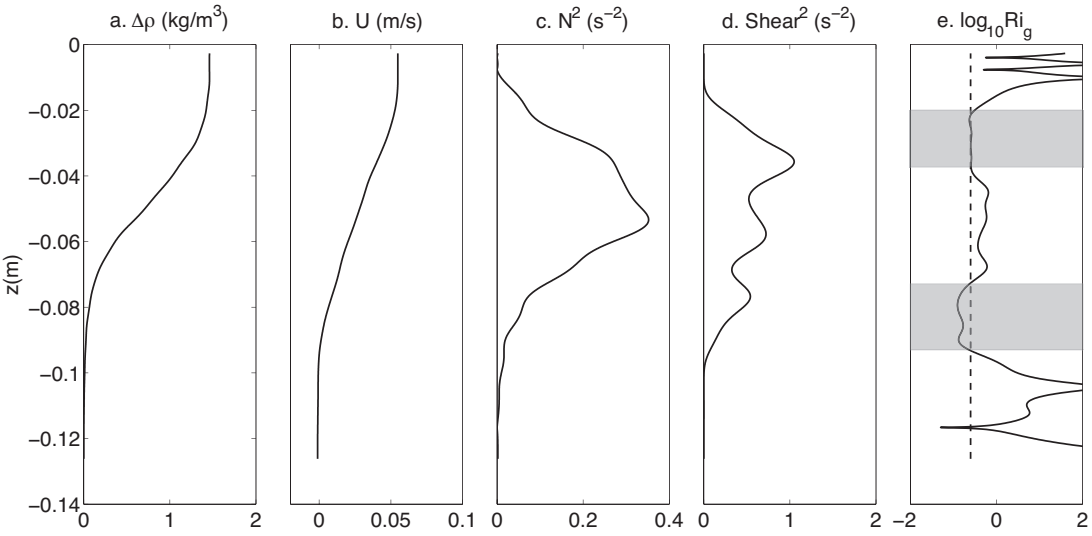

Figure 4.11: a) Density anomaly; b) velocity; c) buoyancy frequency square; d) shear square; and e) gradient Richardson number of a high Fr_i channelized case used to solve the Taylor-Goldstein equation. Shadow area in (e) indicates the region $Ri_g \leq 1/4$.

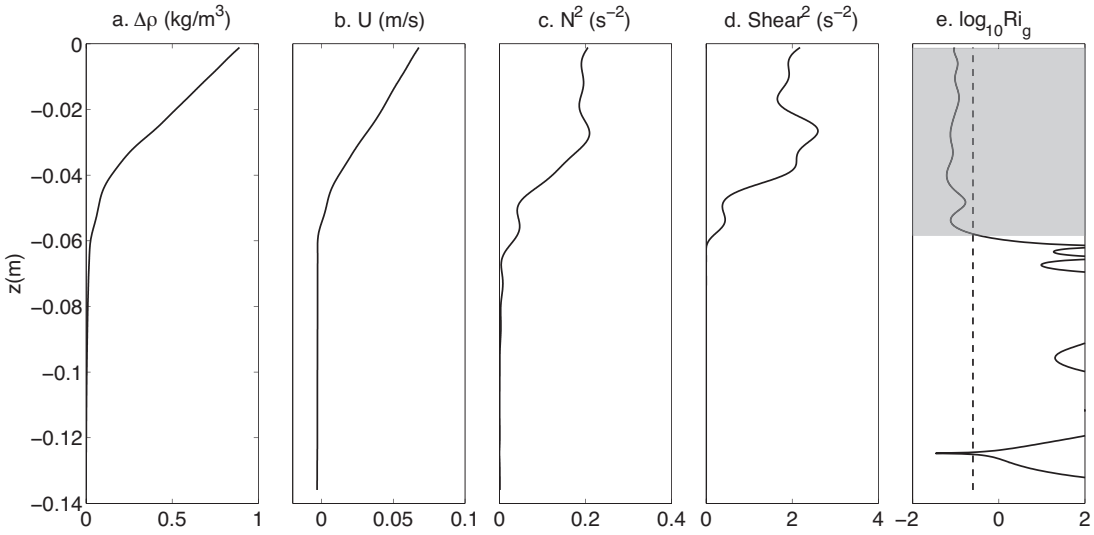

Figure 4.12: Same as Figure 4.11 but for a high Fr_i spreading case.

For each value of wavenumber k, TG solutions provide an eigenfunction-eigenvalue sets of $\{\phi(z), c\}$. Here $c = c_r + ic_i$, is the complex phase speed. The background flow is said to be unstable if any modes exists that have $c_i \neq 0$, where the growth rate is then defined as $\sigma = kc_i$. In general, the mode with the maximum growth rate is the mode that most likely to be observed.

The solutions of channelized flow are shown in Figure 4.13 a. The corresponding value of bulk Richardson number $Ri_b = xx$. The stability analysis yields a single mode of instability. The mode is most unstable at wavenumber approximately 35.8 m^{-1}, the corresponding wavelength is 17 cm with a peak growth rate of 0.0378 s^{-1}. The phase speed of the instability at this wavelength is 0.009 ms^{-1}.

The density and velocity profiles in the spreading cases result in two modes of instability (Figure 4.13 b). The unstable mode corresponds to the higher wavenumber has a peak growth rate of 0.0573 s^{-1} occurring at a wavenumber of 84.3 m^{-1}

with a phase speed of 0.015 ms^{-1}. This wavenumber slightly higher than the most unstable mode in the channelized case. The corresponding wavelength to this mode is approximately 7.5 cm, still matching the Kelvin-Helmholtz instability. In addition to this secondary local maxima, the most unstable mode occurs at wavenumber approximately 21.0 m^{-1}, the corresponding wavelength is 30 cm with a peak growth rate of 0.0764 s^{-1}. The phase speed of the instability at this wavelength is 0.034 ms^{-1}. The wavelength and the propagation speed are consistent with our observation of the large-scale structure in the plan-view $x - t$ diagram for the spreading case (§ 4.4.1).

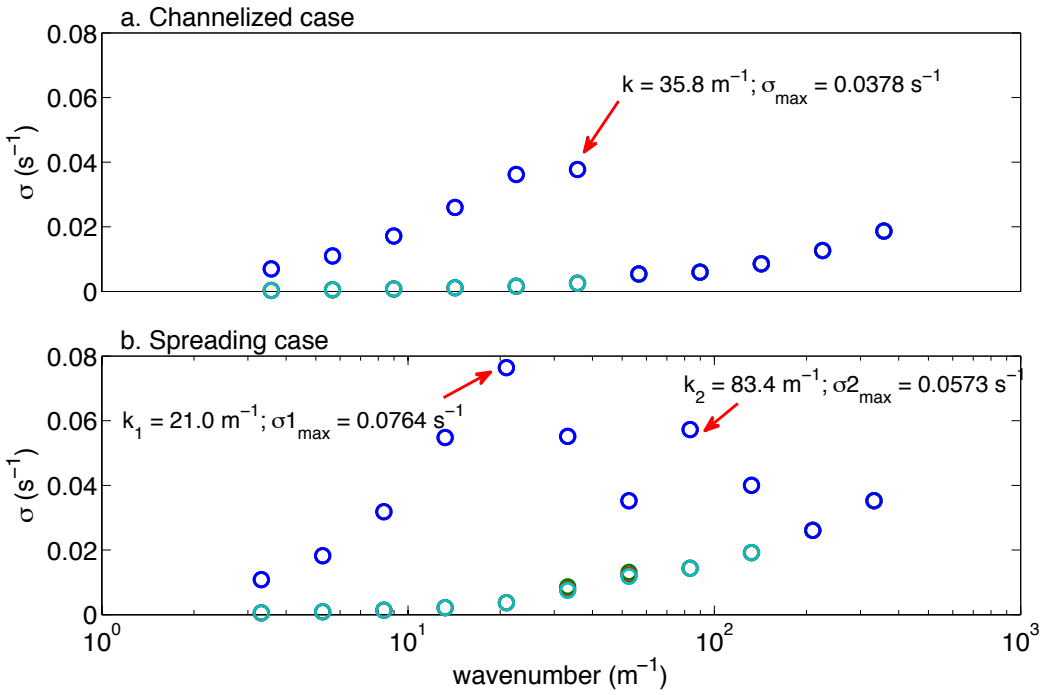

Figure 4.13: Growth rate vs wavenumber for a) channelized and b) spreading high Fr_i runs using the data shown in Figure 4.11 and 4.12, respectively. Three local prominent maxima (one for channelized case and two for spreading case) are highlighted by arrows and labeled their maximum value and corresponding wavenumber in text.

4.4.3 Formation of trapped cores within ISW

A close-up of the large-scale sturcture core is given is Figure 4.14 where contour plots of density, velocity (u and w) and the vorticity ($u_z - w_x$) fields are presented for the exact time shown in Figure A.2. The density and velocity fields are averaged over the time wave core propagating within the field of view. The horizontal velocity is calculate by subtracting with the propagation speed, estimated as $U_m/2$, and then the streamline and vorticity are calculated based on the velocity fields. The averaging process takes out the small-scale K-H instabilities and leaves only the large-scale wave structure. It shows some basic aspects of nonlinear internal solitary-like waves (ISW) identical to that of the theoretical wave discussed by, for example Lamb (1997) or Lee and Beardsley (1974), and also similar to the field observation over continental shelf by Moum et al. (2003). Density contours are compressed in the leading edge of the wave core, with two constant density regions in the core indicated with two black arrows. The highest u values at the center surface of the wave core generate a horizontal convergence region at the frontal side and a horizontal divergence at the trailing edge of the wave core. The downward vertical velocity ahead of the wave and subsequent upward velocity following the wave indicates the internal fluid motion resulting from the passage of the ISW in its form as a wave depression. The motion in the core has the form of two counter-rotating vortices. In the upper front of the core the vorticity is negative (counter-clocwise). Below this region, a strong positive vorticity (clockwise) is at the bottom center of the core. The dominant clockwise (positive vorticity) within the core agrees with the laborotary experiments (Manasseh et al., 1998); however it is in the opposite sense of the numerical models by Lamb (2002). A close streamline core sits right at the core center, coincided with the positive vorticity region. It is reported that this close streamline is an strong evidence of the existing

of nonlinear ISW with trapped cores (Lamb, 1997, 2002). Lamb and Farmer (2011) found that small-scale K-H billows aligned with the pycnocline and growth at is turns to the back of the wave. This shear instabilities are generated because of the thinning pycnocline and compressing streamlines at the front of internal solitary-like waves.

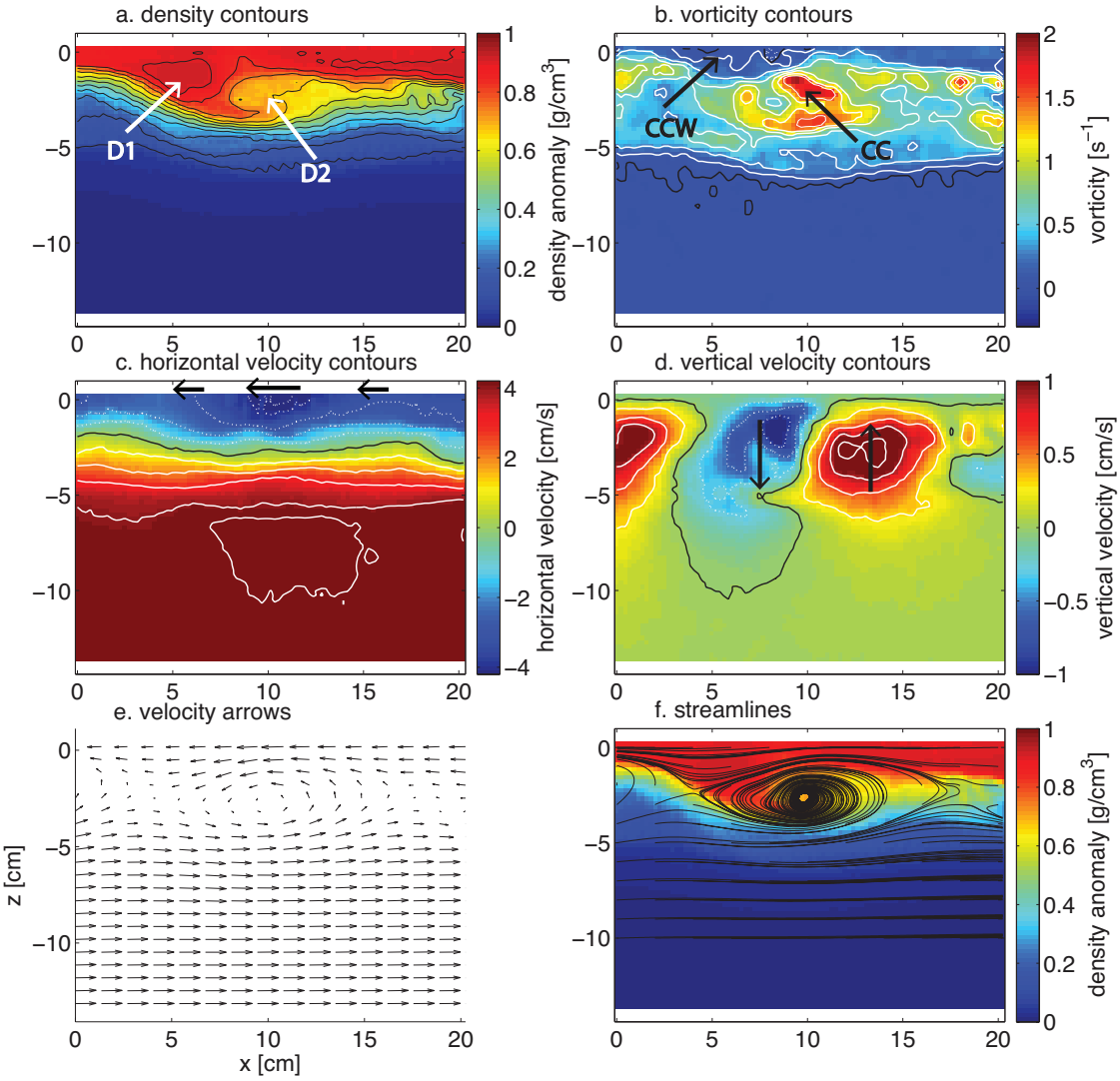

Figure 4.14: Contour plots of a solitary-like wave with a recirculating core same structure shown in Figure A.2. a) density contour; b) vorticity contour; c) horizontal velocity $(u - U_m/2)$; d) vertical velocity; e) velocity arrows; f) streamlines superimposed on density field. Two density cores are indicated as 'D1' and 'D2' in (a) and two vorticity cores are labeled as 'CCW' (counter-clockwise) and 'CW' (clockwise) in (b). Details about each panels are discussed in text.

4.5 Summary

This paper presents a direct comparison between channelized and freely spreading buoyant gravity currents with a continuous freshwater source in laboratory experiments. We observe a large-scale structure in the high Fr_i spreading plume. This structure has a low frequency ($f \approx 0.1 \sim 0.2$ Hz), which has been observed in both spatially in plan-view depth field and temporally in the spectral analysis and stability analysis of vertical density profile time series. Analog to the generation of similar waves in the open ocean when stratified flow meets topography changes, in the river plume case shoaling in depth and expanding horizontally is caused by the lateral spreading of the gravity current. We conclude that the large-scale structure is the nonlinear solitary waves with trapped cores, generated in the supercritical flow via shoaling of the single moving layer as following criteria:

- Energetic two-layer flow:

  High flowrate river makes the plume system falls into the strong barotropic box flow regime in Armi and Farmer (1986);

- Near critical flow:

  $Fr = u/c \sim 1$, wave is generated at the hydraulic control point, i.e., the lift-off region in the river plume system. The propagation speed of the large-scale structure is calculate from two independent methods: 1) $x - t$ diagram based on plan-view depth field, 2) spacial linear stability analysis (TG equation) based on averaged vertical density and velocity profiles;

- Depth shoaling:

Top moving layer shoals because of lateral spreading, this shoaling is essential in both generating the internal solitary wave and forming trapped cores within waves;

- Contraction/Expansion:

  Due to lateral spreading through the river mouth. The river plume system can be analogized to the stratified flow over sill+contraction system because both shoaling in depth and expanding in surface layer are simultaneously achieved by the lateral spreading.

- Monotonic stratification to water surface:

  Mixing layer rises to the water surface because lateral spreading drags the top un-mixed water to the side. Mixing layer has a linear density profile (i.e., monotonic stratification) to the water surface, which is an important criteria in the formation of trapped cores in the ISW as suggested by Lamb (2002).

Lateral spreading dramatically modifies the plume's vertical structure; the spreading plume layer contains approximately linear density and velocity profiles that extend to the surface (Figure 4.12), whereas the channelized plume has regions of uniform density and velocity near the surface (Figure 4.11). This vertical profile difference results in a difference in plume dynamics in the linear stability analysis (Figure 4.13). Consistent with predictions from the two-layer shoaling numerical model, a top uniform density and velocity layer greatly inhibits the formation of nonlinear solitary wave with trapped cores.

We observe that the small-scale K-H billows are generated along the leading edge of each large-scale structure, propagating downstream and finally breaking at the wave trough. This feature inhibits the mixing at the leading edge but increase the mixing in the wave wake region. One result of the lateral spreading is that the vortex is re-arranged to be along the braid of the wave structure (Figure A.2 m-x), rather than scattered within the whole current layer in the channelized case (Figure A.2 a-l). We hypothesize this rearrangement of vortex dynamics is caused by a compression of streamlines at the leading edge of the wave structure.

Chapter 5

CONCLUSIONS

In this dissertation we investigated the dynamics and transport mechanisms of a buoyant discharge. The experiments were divided into two separated parts, each one was concentrated on one specific region of the buoyant river plume. We made both a relatively simple experimental set-up (optical thickness method) and complex and accurate measurements (PIV-PLIF) with advanced laser technology on idealized laboratory river plumes. The first type of experiment was conducted in order to investigate the dynamics of the river plume bulge and the impact of alongshore upstream current in a rotating system. We ran fresh water through two identical inlets and observed the bulge evolution of the downstream plume. The second goal was to study the impacts of lateral spreading on mixing, entrainment, and plume structure in the near-field buoyant river plume. We varied the inflow conditions and conducted exactly the same measurement with and without lateral boundaries. We measured the high-resolution density and velocity field and calculated the buoyancy using the control-volume method. This direct measurement allowed us to determine the mixing efficiency over a range of inflow conditions and compare between channelized and spreading cases.

This dissertation makes several key contributions to our understanding of the dynamics of river plumes.

We generated a two-dimensional calibration map from two depth-dependent relationships and applied it to the mid-field plume on the rotating table. We observed

that the upstream bulge grew offshore and wrapped around the downstream plume bulge to form a large re-circulating bulge system. This bulge accumulated inflow fluid from both inlets and became unstable, until a critical time, at which a small bulge separated from the larger system and propagated downstream. The large bulge then returned to its stable state.The bulge growth rate and freshwater transport in the coastal current were calculated based on the obtained depth field and the assumption that the coastal current is in a cross-shore geostrophic balance. The computed transport closes the freshwater budget for the system, but requires an empirical coefficient $\alpha = 0.6$. Although this coefficient is significantly below unity, the fact that the computed transport only departs from that needed to close the balance by a constant implies that our expression captures the principal dynamics of the system.

We investigated a direct comparison between channelized and freely spreading buoyant gravity currents with a continuous freshwater source in laboratory experiments. The configuration of the experiments simulates a coastal river inflow with a simplified geometry in order to better understand the role of lateral spreading on the mixing and dilution of river water as it enters the coastal ocean. We observed that the lateral spreading rate is highly dependent on the inflow condition as characterized by Fr_i: the plume is convergent when $Fr_i < 1$ and divergent when $Fr_i > 1$. We estimated the entrainment rate E and the turbulent buoyancy flux B using the control volume method. A key outcome of this work is the observation that there is no difference between the entrainment rate or buoyancy flux in the channelized and spreading cases. This indicates that lateral spreading does not modify the local mixing efficiency. We hypothesized that this is because the spreading occurs preferentially near the surface, whereas buoyancy flux is greatest in the core of the current. We concluded that as estuary water enters the coastal ocean, lateral expansion oc-

curs preferentially near the surface, eliminating the uniform density layer observed at the surface in the estuary and shifting the mixing layer upwards to the water surface. Near-surface water is thus redistributed across a much wider area, where it then forms the plume base and is susceptible to mixing. The result of the lateral advection of fresh near-surface water is that the plume layer is more diluted on average in the presence of spreading than in an equivalent channelized flow.

We observed a large-scale structure in the high Fri spreading plume. We hypothesized that the large-scale structure is the nonlinear solitary waves with trapped cores, generated in the supercritical flow via shoaling of the single moving layer. And we provided solid evidence from stability and spectral analyses to confirm this wave-like structure has a frequency $f \approx 0.1 \sim 0.2$ Hz. We observed small-scale K-H billows were generated along the leading edge of each large-scale structure, propagating downstream and finally breaking at the wave trough. This feature inhibited the mixing at the leading edge but increased the mixing in the wave wake region. One result of the lateral spreading was that the vortex is re-arranged to be along the braid of the wave structure, rather than scattered within the whole current layer in the channelized case. We hypothesized this rearrangement of vortex dynamics is caused by a compression of streamlines at the leading edge of the wave structure.

In summary this dissertation provides three principal contributions to the understanding of river plume dynamics. First, laboratory experiments show that the plume bulge cannot reach a steady state with the coastal current from an identical upstream river plume. Second, we find that lateral spreading does not change the local mixing in the near-field region. However, it significantly increases the total mixing in the plume because of the increase in the horizontal area of the plume.Third, we demonstrate that the plume structure in the near-field plume is strongly modified by lateral

spreading. The shoaling and acceleration associated with lateral spreading provide a source of non-linear internal solitary waves with trapped cores in the coastal ocean.

Finally, our laboratory methods make a significant contribution to the field of experimental fluid mechanics. This work represents a novel method to extend classical optical thickness measurement to a two-dimensional calibration map using two colors for calculating two interacting plumes depth fields. In addition, the combination of optical thickness measurement and PIV-PLIF technique provides a comprehensive measurement of the full-field structure of buoyant river plumes.

BIBLIOGRAPHY

Afanasyev, Y. D. and W. R. Peltier, 2001: On breaking internal waves over the sill in Knight Inlet. *Proc. R. Soc. Lond. A*, **457**, 2799 – 2825.

Afanasyev, Y. D., P. B. Rhines, and E. G. Lindahl, 2009: Velocity and potential vorticity fields measured by altimetric imaging velocimetry in the rotating fluid. *Experiment in Fluids*, **47 (6)**, 913–926.

Alahyari, A. and E. Longmire, 1996: Development and structure of a gravity current head. *Exps. Fluids*, **20**, 410–416.

Armi, L., 1986: The hydraulics of two flowing layers with different densities. *J. Fluid Mech.*, **163**, 27–58.

Armi, L. and D. M. Farmer, 1986: Maximal two-layer exchange through a contraction with barotropic net flow. *J. Fluid Mech.*, **164**, 27–51.

Avicola, G. and P. Huq, 2002: Scaling analysis for the interaction between a buoyant coastal current and the continental shelf: experiments and observations. *Journal of Physical Oceanography*, **32 (11)**, 3233–3248.

Benjamin, T. B., 1968: Gravity currents and related phenomena. *J. Fluid. Mech.*, **31**, 209–248.

Bowen, A. J. and R. A. Holman, 1989: Shear instabilities of the mean longshore current 1. Theory. *J. Geophys. Res.*, **94 (C12)**, 18 023–18 030.

Britter, R. E., 1979: The spread of negatively buoyant plume in a calm environment. *Atmo. Environ.*, **13**, 1241–1247.

Britter, R. E. and J. E. Simpson, 1978: Experiments on the dynamics of a gravity current head. *J. Fluid Mech.*, **88**, 223–240.

Buch, E., 1980: On entrainment and vertical mixing in stably stratified fjords. *2nd Intern. Symposium on Stratified flows*, Throndheim, Norway, 461–469.

Cantero, M. I., S. Balachandar, and M. H. Gacia, 2007a: High-resolution simulations of cylindrical density currents. *J. Fluid Mech.*, **590**, 437–469.

Cantero, M. I., S. Balachandar, M. H. Gacia, and J. Ferry, 2006: Direct numerical simulations of planar and cylindrical density currents. *J. Appl. Mech.*, **73**, 923–930.

Cantero, M. I., J. R. Lee, S. Balachandar, and M. H. Gacia, 2007b: On the front velocity of gravity currents. *J. Fluid Mech.*, **586**, 1–39.

Cenedese, C., 1998: Baroclinic eddies over topography. Ph.D. thesis, University of Cambridge.

Cenedese, C. and S. Dalziel, 1998: Concentration and depth field determined by the light transmitted through a dyed solution. *8th international symposium on flow visualization*, 61.1–61.5.

Cenedese, C. and S. Dalziel, 1999: Concentration and depth fields determined by the light transmitted through a dyed solution. *submitted to Experiment in Fluids*.

Cenedese, C. and J. A. Lerczak, 2008: Understanding the dynamics of the interaction between two river plumes. *Fifth International Symposium on Environmental Hydraulics*, 1–6.

Chant, R. J., S. M. Glenn, E. Hunter, J. Kohut, R. F. Chen, R. W. Houghton, J. Bosch, and O. Schofield, 2008: Bulge formation of a buoyant river outflow. *Journal of Geophysical Research-Oceans*, **113**.

Chen, F., D. G. MacDonald, and R. D. Hetland, 2009: Lateral spreading of a near-field river plume: Observations and numerical simulations. *J. Geophys. Res.*, **114**, C07 013, doi:10.1029/2008JC004893.

Chen, J. C., 1980: Studies on gravitational spreading currents. Ph.D. thesis, California Institute of Technology, 436 pp.

Chen, J. C. and E. J. List, 1976: Spreading of buoyant discharges. *Proc. 1st CHMIT Seminar on Turbulent buoyant convection*, 171 – 182.

Christodoulou, G. C., 1986: Interfacial mixing in stratified flows. *J. Hydraul. Res.*, **24 (2)**, 77–92.

Chu, V. H. and M. R. Vanvari, 1976: Experimental study of turbulent stratified shearing flow. *J. Hydraulics Div., ASCE*, **102 (HY6)**, 691–706.

Cowen, E. A., K. A. Chang, and Q. Liao, 2001: A single-camera coupled PTV technique. *Experiments in Fluids*, **31 (1)**, 63–73.

Crimaldi, J. P., 2008: Planar laser induced fluorescence in aqueous flows. *Exp. Fluids*, **44 (6)**, 851–863.

Didden, N. and T. Maxworthy, 1982: The viscous spreading of plane and axisymmetric gravity currents. *J. Fluid Mech.*, **121**, 27–42.

Ellison, T. H. and J. S. Turner, 1959: Turbulent entrainment in stratified flows. *J. Fluid Mechanics*, **6**, 423–448.

Farmer, D. M. and L. Armi, 1986: Maximal two-layer exchange over a sill and through the combination of a sill and contraction with barotropic flow. *J. Fluid Mech.*, **164**, 53–76.

Farmer, D. M. and L. Armi, 1999: The generation and trapping of solitary waves over topography. *Science*, **283**, 188–190.

Farmer, D. M. and J. D. Smith, 1977: Nonlinear internal waves in a fjord. *Hydrodynamics of estuaries and fjords*, J. Nihoul, Ed., Elsevier, 465–493.

Farmer, D. M. and J. D. Smith, 1980: Tidal interaction of stratified flow with a sill in Knight Inlet. *Deep-Sea Res.*, **27A**, 239–254.

Fong, D. A. and W. R. Geyer, 2002: The alongshore transport of freshwater in a surface-trapped river plume. *Journal of Physical Oceanography*, **32 (3)**, 957–972.

Garvine, R. W., 1984: Radial spreading of buoyant, surface plumes in coastal waters. *J. Geophys. Res.*, **89 (C2)**, 1989–1996.

Geyer, W. R., A. C. Lavery, M. E. Scully, and J. H. Trowbridge, 2010: Mixing by shear instability at high Reynolds number. *Geophys. Res. Lett.*, **37**, L22 607.

Gonzalez, R. C., R. E. Woods, and S. L. Eddins, 2004: *Digital Image Processing using MATLAB*. Prentice Hall, 201-211 pp.

Griffiths, R. W. and E. J. Hopfinger, 1983: Gravity currents moving along a lateral boundary in a rotating fluid. *Journal of Fluid Mechanics*, **134**, 357–399.

Hallworth, M. A., H. E. Huppert, J. C. Phillips, and R. S. J. Sparks, 1996: Entrainment into two-dimensional and axisymmetric turbulent gravity currents. *J. Fluid Mech.*, **308**, 289–311.

Halverson, M. and R. Pawlowicz, 2011: Entrainment and flushing time in the Fraser River estuary and plume from a steady salt balance analysis. *J. Geophys. Res.*, **116**, C08 023.

Hartel, C., E. Meiburg, and F. Necker, 2000: Analysis and direct numerical simulation of the flow at a gravity-current head. Part 1. Flow topology and front speed for slip and non-slip boundaries. *J. Fluid Mech.*, **418**, 189–212.

Hetland, R. D., 2005: Relating river plume structure to vertical mixing. *J. Phys. Oceanogr.*, **35 (9)**, 1667–1688.

Hetland, R. D., 2010: The effects of mixing and spreading on density in near-field river plumes. *Dyn. Atmos. Oceans*, **49**, 37–53.

Hetland, R. D. and D. G. MacDonald, 2008: Spreading in the near-field merrimack river plume. *Ocean Modell.*, **21**, 12–21, doi:10.1016/j.ocemod.2007.11.001.

Hickey, B. M., L. J. Peitrafesa, D. A. Jay, and W. C. Boicourt, 1998: The Columbia River plume study: subtidal variability in the velocity and salinity field. *J. Geophys. Res.*, **103 (C5)**, 10 339 – 10 368.

Holford, J. M. and S. B. Dalziel, 1996: Measurements of layer depth during baroclinic instability in a two-layer flow. *Applied Scientific Research*, **56 (2-3)**, 191–207.

Horner-Devine, A. R., 2006: Velocity, density and transport measurements in rotating, stratified flows. *Experiments in Fluids*, **41 (4)**, 559–571.

Horner-Devine, A. R., D. A. Fong, S. G. Monismith, and T. Maxworthy, 2006: Laboratory experiments simulating a coastal river inflow. *Journal of Fluid Mechanics*, **555**, 203–232.

Horner-Devine, A. R., D. A. Jay, P. M. Orton, and E. Y. Spahn, 2009: A conceptual model of the strongly tidal Columbia River plume. *J. of Marine System*, **78 (3)**, 460–475.

Hoult, D., 1972: Oil spreading in the sea. *Annu. Rev. Fluid Mech.*, **4**, 341–368.

Huppert, H. E. and J. E. Simpson, 1980: The slumping of gravity currents. *J. Fluid Mech.*, **99**, 785–799.

Ivey, G. N. and J. Imberger, 1991: On the nature of turbulence in a stratified fluid: 1. The energetics of mixing. *J. Phys. Oceanogr.*, **21**, 650–658.

Ivey, G. N., K. B. Winters, and J. R. Koseff, 2008: Density stratification, turbulence, but how much mixing? *Annu. Rev. Fluid Mech.*, **40**, 169–84.

Jirka, G. H., E. E. Adams, and K. D. Stolzenbach, 1981: Buoyant surface jets. *J. Hydr. Div*, **107 (11)**, 1467–1487.

Kay, D. J. and D. A. Jay, 2003: Interfacial mixing in a highly stratified estuary 1. Characteristics of mixing. *J. Geophys. Res.*, **108 (C3)**, 3072.

Kilcher, L. F. and J. D. Nash, 2010: Structure and dynamics of the Columbia River tidal plume front. *J. Geophys. Res.*, **115**, C05S90.

Kilcher, L. F., J. D. Nash, and J. N. Moum, 2012: The role of turbulence stress divergence in decelerating a river plume. *J. Geophys. Res.*, **117**, C05 032.

Kinder, T. H., 1984: Net mass transport by internal waves near the Strait of Gibraltar. *Geophys. Res. Letters*, **11 (10)**, 987–990.

Lamb, K. G., 1997: Particle transport by nonbreaking internal solitary waves. *J. Geophys. Res.*, **102**, 18 641 – 18 660.

Lamb, K. G., 2002: A numerical investigation of solitary internal waves with trapped cores formed via shoaling. *J. Fluid Mech.*, **451**, 109–144.

Lamb, K. G. and D. M. Farmer, 2011: Instabilities in an internal solitary-like wave on the Oregon shelf. *J. Phys. Oceanogr.*, **41**, 67–87.

Lawrence, G. A., F. K. Browand, and L. G. Redekopp, 1991: The stability of a sheared density interface. *Phys. Fluids*, **3 (10)**, 2360–2370.

Lee, C. and R. Beardsley, 1974: The generation of lone nonlinear internal waves in a weakly stratified shear flow. *J. Geophys. Res.*, **79**, 453–462.

Linden, P. F. and J. E. Simpson, 1985: Buoyancy driven flow through an open door. *Air Infiltration Rev.*, **6**, 4–5.

Linden, P. F. and J. E. Simpson, 1994: Continuous releases of dense fluid from an elevated point source in a cross-flow. *Mixing and transport in the environment*, K. J. Beven, P. C. Chatwin, and J. H. Millbank, Eds., Wiley, 401–408.

Luketina, D. A. and J. Imberger, 1987: Characteristics of a surface buoyant jet. *J. Geophys. Res.*, **94 (C5)**, 5435–5447.

MacDonald, D. G. and F. Chen, 2012: Enhancement of turbulence through lateral spreading in a stratified-shear flow: Development and assessment of a conceptual model. *J. Geophys. Res.*, inpress, doi:10.1029/2011JC007484.

MacDonald, D. G. and W. R. Geyer, 2004: Turbulent energy production and entrainment at a highly stratified estuarine front. *J. Geophys. Res.*, **109**, C05 004, doi:10.1029/2003JC002094.

MacDonald, D. G. and A. R. Horner-Devine, 2008: Temporal and spatial variability of vertical salt flux in a highly stratified estuary. *J. Geophys. Res.*, **113**, C09 022, doi:10.1029/2007JC004620.

MacDonald, M. D., L. Goodman, and R. D. Hetland, 2007: Turbulent dissipation in a near-field river plume: A comparison of control volume and microstructure observations with a numerical model. *J. Geophys. Res.*, **112**, C07 026, doi: 10.1029/2006JC004075.

Maclatchy, M. R., 1999: Radially spreading surface flows. Ph.D. thesis, University of British Columbia, 87 pp.

Manasseh, R., C. Y. Ching, and H. J. S. Fernando, 1998: The transition from density-driven to wave-dominated isolated flows. *J. Fluid Mech.*, **361**, 253–274.

McClimans, T. A., 1978: Fronts in fjords. *Geophys. Astrophys. Fluid Dyn.*, **11**, 23–24.

Morton, B. R., G. Taylor, and J. S. Turner, 1956: Turbulent gravitational convection from maintained and instantaneous sources. *Proc. R. Soc. London, Ser. A*, **234**, 1–23.

Moum, J. N., D. M. Farmer, W. D. Smyth, L. Armi, and S. Vagle, 2003: Structure and generation of turbulence at interfaces strained by internal solitary wave propagating shoreward over the continental shelf. *J. Phys. Oceanogr.*, **33**, 2093 – 2112.

Nof, D. and T. Pichevin, 2001: The ballooning of outflows. *Journal of Physical Oceanography*, **31 (10)**, 3045–3058.

Nowacki, D. J., A. R. Horner-Devine, J. D. Nash, and D. A. Jay, 2012: Rapid sediment

removal from the columbia river plume near field. *Continental Shelf Research*, **35**, 16–28.

Oltman-Shay, J., P. A. Howd, and W. A. Birkemeier, 1989: Shear instabilities of the mean longshore current 2. Field observations. *J. Geophys. Res.*, **94 (C12)**, 18 031–18 042.

Orton, P. M. and D. A. Jay, 2005: Observations at the tidal plume front of a high-volume river outflow. *Geophys. Res. Lett.*, **32**, L11 605.

Patterson, M. D., J. E. Simpson, S. B. Dalziel, and G. J. F. van Heijst, 2006: Vortical motion in the head of an axisymmetric gravity current. *Phys. Fluids*, **18**, 046 601.

Pawlak, G. and L. Armi, 1998: Vortex dynamics in a spatially accelerating shear layer. *J. Fluid Mech.*, **376**, 1–35.

Pawlak, G. and L. Armi, 2000: Mixing and entrainment in developing stratified currents. *J. Fluid Mech.*, **424**, 45–73.

Pedersen, F. B., 1980: *A Monograph on turbulent entrainment and friction in two-layer stratified flow*. Inst. of Hydrodynamics and Hydraulic Engin., Techn. University of Denmark, Series Paper No. 25.

Penney, W. G. and C. K. Thornhill, 1952: Pt. iii. the dispersion under gravity of a column of fluid supported on a rigid horizontal plane. *Phil. Trans. Roy. Soc. London*, **A244**, 285–311.

Rocca, M. L., C. Adduce, G. Sciortino, and A. B. Pinzon, 2008: Experimental and numerical simulation of three-dimensional gravity currents on smooth and rough bottom. *Phys. Fluids*, **20**, 106 603.

Rottman, J. W. and J. E. Simpson, 1983: Gravity currents produced by instantaneous releases of a heavy fluid in a rectangular channel. *J. Fluid Mech.*, **1351**, 95–110.

Rottman, J. W. and J. E. Simpson, 1984: The initial development of gravity currents from fixed-volume releases of heavy fluids. *Atmospheric Dispersion of Heavy Gases and Small Particles*, G. Ooms and H. Tennekes, Eds., Springer, New York, 347–359.

Shih, L. H., J. R. Koseff, G. N. Ivey, and J. H. Ferziger, 2005: Parameterization of turbulent fluxes and scales using homogenous sheared stably stratified turbulence simulations. *J. Fluid Mech.*, **525**, 193–214.

Shin, J. O., S. B. Dalziel, and P. F. Linden, 2004: Gravity currents produced by lock exchange. *J. Fluid Mech.*, **521**, 1–34.

Signell, R. P. and W. R. Geyer, 1991: Transient eddy formation around headlands. *J. Geophys. Res.*, **96 (C2)**, 2561 – 2575.

Simpson, J. E., 1997: *Gravity Current: in the Environment and the Laboratory*. 2d ed., Cambridge University Press, 244 pp.

Stillinger, D. C., K. N. Helland, and C. W. V. Atta, 1983: Experiments on the transition of homogeneous turbulence to internal waves in a stratified fluid. *J. Fluid Mech.*, **131**, 91–122.

Sveen, J. K., 2004: An introduction to matpiv v.1.6.1. Eprint no. 2, **ISSN** 0809-4403, Dept. of Mathematics, University of Oslo, 27 pp.

Tedford, E. W., J. R. Carpenter, R. Pawlowicz, R. Pieters, and G. A. Lawrence, 2009a: Observation and analysis of shear instability in the fraser river estuary. *J. Geophys. Res.*, **114**, C11 006.

Tedford, E. W., R. Pieters, and G. A. Lawrence, 2009b: Symmetric holmboe instabilities in a laboratory exchange flow. *J. Fluid Mech.*, **636**, 137–153.

Thomas, L. P., S. B. Dalziel, and B. M. Marino, 2003: The structure of the head of an inertial gravity current determined by particle-tracking velocimetry. *Exp. Fluids*, **34**, 708.

Thomas, P. J. and P. F. Linden, 1998: A bi-modal structure imposed on gravity driven boundary currents in rotating systems by effects of the bottom topography. *Exp. Fluids*, **25**, 388–391.

Thorpe, S. A., 1971: Experiments on instability of stratified shear flow: miscible fluids. *J. Fluid Mech.*, **46**, 299–319.

Thorpe, S. A., 1973: Experiments on instability and turbulence in a stratified shear flow. *J. Fluid Mech.*, **61**, 731–751.

Tian, X. D. and P. J. W. Roberts, 2003: A 3D LIF system for turbulent buoyant jet flows. *Experiments in Fluids*, **35 (6)**, 636–647.

Ungarish, M. and T. Zemach, 2005: On the slumping of high reynolds number gravity currents in two-dimensional and axisymmetric configurations. *Eur. J. Mech. B/Fluids*, **24**, 71–90.

von Karman, T., 1940: The engineer grapples with nonlinear problems. *Bull. Amer. Math. Soc.*, **46**, 615–683.

Wedemeyer, E., 1964: The unsteady flow within a spinning cylinder. *Journal of Fluid Mechanics*, **20**, 383–399.

Wright, L. D. and J. M. Coleman, 1971: Effluent expansion and interfacial mixing in the presence of a salt wedge, Mississippi River Delta. *J. Geophys. Res.*, **76 (36)**, 8649–8661.

Wright, S. J., P. J. W. Roberts, Y. Zhongmin, and N. E. Bradly, 1991: Surface dilution of round submerged buoyant jets. *J. Hydraulic Res.*, **29 (1)**, 67–89.

Yuan, Y., M. E. Averner, and A. R. Horner-Devine, 2011: A two-color optical method for determining layer thickness in two interacting buoyant plumes. *Exp. Fluids*, **50 (5)**, 1235–1245.

Yuan, Y. and A. R. Horner-Devine, submitted: Laboratory investigation of the impact of lateral spreading on buoyancy flux in a river plume. *J. Phys. Oceanogr.*

Zhang, X., D. Dabiri, and M. Gharib, 1996: Optical mapping of fluid density interfaces: Concepts and implementations. *Review of Scientific Instruments*, **67 (5)**, 1858–1868.

Zhou, J., R. J. Adrian, S. Balachandar, and T. M. Kendall, 1999: Mechanisms for generating coherent packets of hairpin vortices in channel flow. *J. Fluid Mech.*, **387**, 353–396.

Zhou, J., T. S. Huang, and R. J. Adrian, 1996: Extracting 3d vortices in turbulent fluid flow. *IEEE transactions on pattern analysis and machine intelligence*, **20 (2)**, 193–199.

Appendix A

GENERATION OF SMALL KELVIN-HELMHOLTZ BILLOWS WITH INTERNAL SOLITARY WAVES: THE VORTEX DYNAMICS

A.1 Vortex structures at plume front

Figure A.1 presents images sequences of the density fields along with swirling strength for each image with 1 s time interval between each images. Swirling strength $|\lambda_{ci}|$, defined as the absolute value of the imaginary portion of the complex eigenvalues of the local velocity gradient tensor provides a clean measure of the vortical structures of the flow (Cantero et al., 2007b). Zhou et al. (1999) proved that swirling strength picks out regions of intense vorticity, but discriminates against planar shear layers, where vorticity is balanced by strain rate. Swirling strength is mainly used in the three-dimensional numerical simulations, however, Zhou et al. (1996) presented $|\lambda_{ci}|$ from 2D velocity fields worked successfully in detecting regions of high vorticity concentrations. Those regions often correspond to the higher turbulence area with high turbulent dissipation rate.

Two columns on the left in Figure A.1 are the channelized case, while two columns on the right are the identical time for each images from the same inflow condition in spreading cases. The sequences represent successive stages of the development of the front head. The frame interval for each sequence is 1 s.

In the earliest stage of the frontal bore, a sharp leading edge is observed in both cases (Figure A.1 a, m). Along the leading edge, a small K-H billow starts to be

generated at the density interface due to the high shear (arrow '1' two panels). This K-H billow is picked up by $|\lambda_{ci}|$ clearly in Figure A.1 g and s (arrow '1s' in two panels). 1 s later(Figure A.1 b, n), this K-H billow moves offshore with the plume current, slightly stretched along the leading edge. Another K-H core is identified in the spreading case (n), labeled as '2' with an arrow. This K-H billow is more developed comparing to the earlier one. K-H billows propagate slower than the frontal speed, so that the billow edge increases in the direction opposite to the frontal propagation. If we think in temporal reference frame, the second K-H billow is the result of the first K-H billow developing with time. Those two K-H billows correspond to high $|\lambda_{ci}|$ regions shown in the swirling strength field Figure A.1 u (arrow '1s' and '2s'). In the channelized case at the same time, however, the second K-H billow can not be clearly identified in the density field (Figure A.1 d). In the swirling strength field (Figure A.1 j), we observe a region of high $|\lambda_{ci}|$ corresponding to the first K-H billow (arrow '1s'), but not for the second one. After another 2 s of development, the image in spreading case turns into the trailing edge of the frontal bore (Figure A.1 e and q). The second K-H billow is fully developed and breaks into turbulence at the thickest point in the frontal bore. The wake behind it is a high turbulence region where most of the mixing and entrainment have happened. On the other hand, there is no clear 'break' of the K-H billow process in the channelized case. Once K-H instability is generated at the interface, it breaks shortly. This makes the turbulence almost uniform within the current, indicated by a scatter but uniform swirling strength in Figure A.1 k and l. Even in the leading edge, we can observe some entrainment of denser ambient water (darker region within the front in Figure A.1 b and c). In contrast, there is almost no mixing in the leading side of the frontal bore in spreading case (Figure A.1 n and o). Mixing starts to happen after the second K-H billow developed and darker regions

are then identified in Figure A.1 p and q.

Generally, K-H instabilities are clearly identified along the leading edge in the spreading case. They develop along the 'braid' of the frontal bore, and then turn into fully developed turbulence at the trailing edge of frontal bore. Within the frontal bore, vorticity is low and fluid is almost uniform with low entrainment from the ambient water. In the channelized case mixing happens along the interface and there is no clear low entrainment regions.

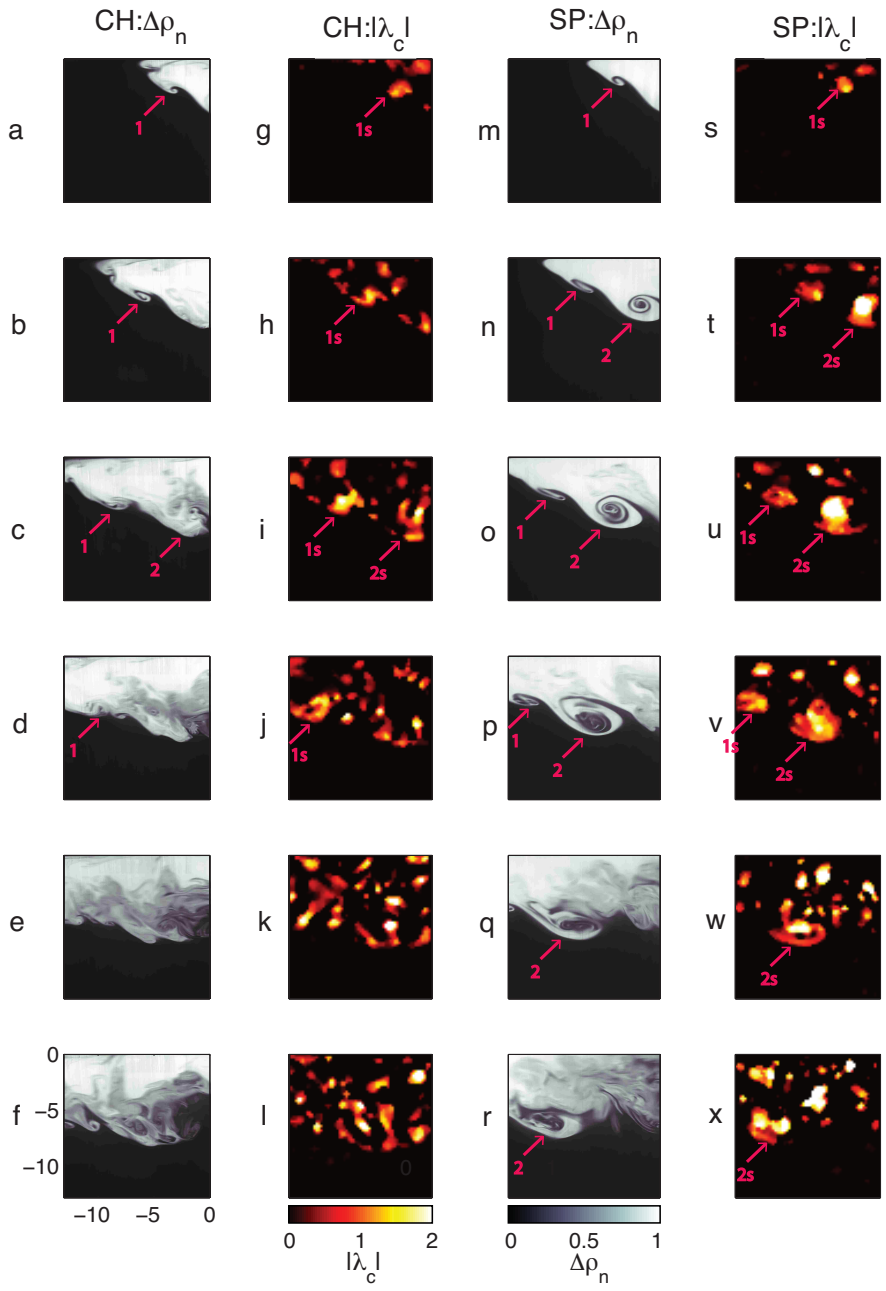

Figure A.1: Normalized density anomaly field (left-hand column) and swirling strength (right-hand column) sequence at the plume front region for channelized case (density field: a-f; swirling strength field: g-l) and spreading case (density field: m-r; swirling strength field: s-x). Time increases downward at each column, time interval between two frames is 1 s. Physical dimension of this field of view is labeled at the lower-left corner, with the unit of [cm]. $|\lambda_{ci}|$ and $\Delta\rho_n$ scales are shown in the colorbars at the bottom of second and third column, respectively.

A.2 Vortex structures at steady-state

As the discussion for Figure 4.8, we observe continuously large-scale structures in the high Fr_i spreading case: each large-scale structure acts like an individual front. Here we pick up one of those repeating structures and analysis it in detail from the images sequences of the density fields along with swirling strength similar to §A.1 (Figure A.2).

Within one large-scale structure (Figure A.2 m-x), there is evidence of the persistence of the vortex mechanism along the leading edge illustrated in Figure A.1 m-x. After the last structure passes offshore, the current turns into a highly stratified region. A sharp interface between two fluids forms right at the fully turbulence region. A K-H billow (labeled as '1' in Figure A.2 m) is generated along this sharp interface. It develops in time and goes offshore with the plume current (Figure A.2 n and o). A second K-H billow begins to be identified at Figure A.2 p, labeled as '2'. Then the second K-H billow breaks into turbulence at the trailing edge of this large-scale structure. Both two K-H billows can be clearly picked out in the corresponding swirling strength fields (labeled as '1s' and '2s', respectively). At the same time in the channelized case, however, there is no clear tendency along the interface. Several small-scale K-H billows can be identified at the shear layer. The swirling strength fields show that the turbulence energy spreads out within the current more uniform than the spreading case.

One interesting feature in the vortex dynamics of spreading plume is that the small-scale vortex billows separates from the main large-scale structure and 'leapfrogs' the next large-scale structure because it has smaller velocity comparing to the plume layer. It is hard to identified in the density field because the density is high after entraining denser water into the billow, however, it can be clearly observed in the

swirling strength field (labeled as blue arrow in Figure A.2 s-x). It interacts with the K-H billows from the next large-scale structure ('2s') to form a vortex pair. The K-H billow '2s' actually will detach from the main large-scale structure and influence the next one as the billow pointed by blue arrows. This vortex 'leapfrog' pairing phenomenon was previously observed by Pawlak and Armi (1998) in their laboratory study of spatially accelerating stratified shear layer.

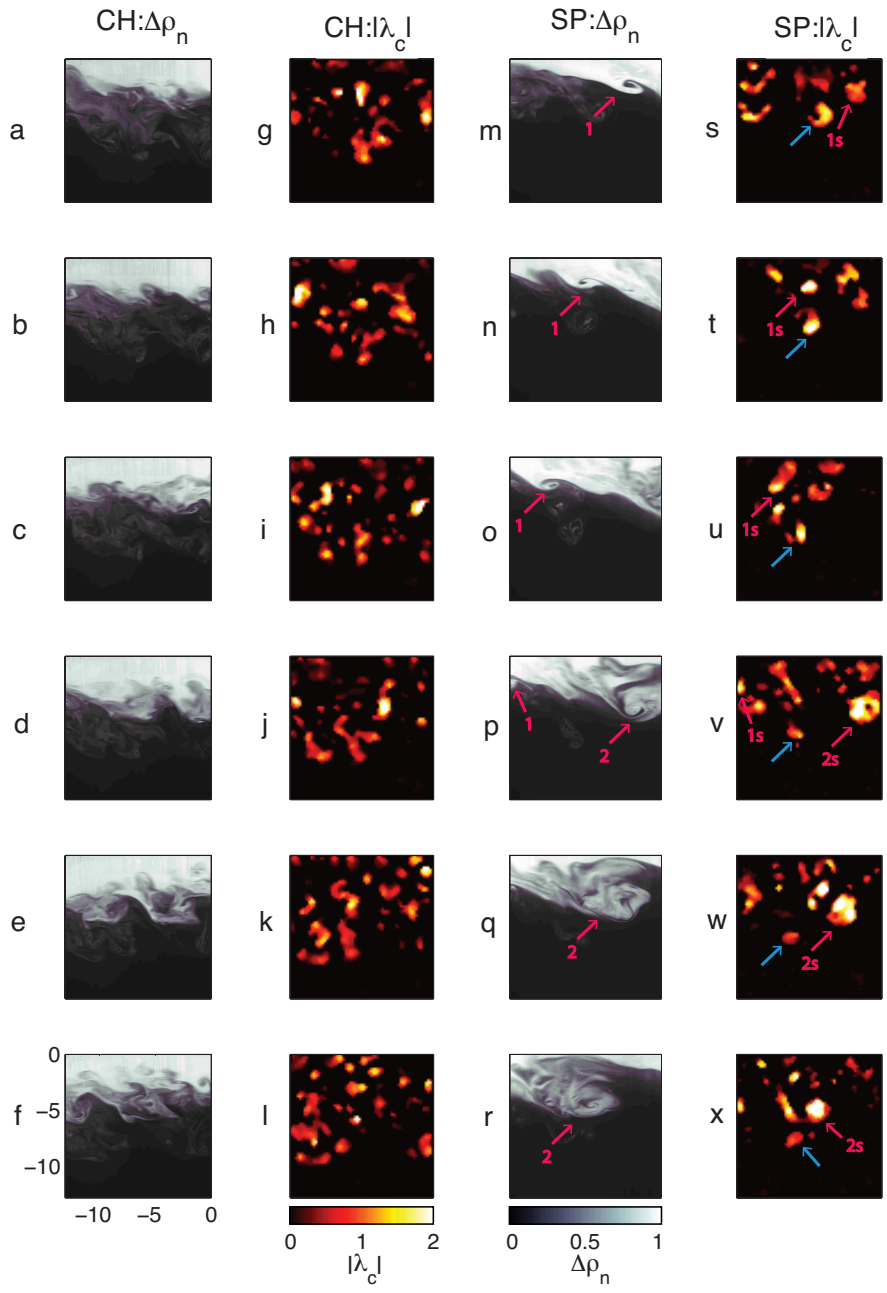

Figure A.2: Same as Figure A.1 but for a later time when plume turns into steady-state region